Single Higgs Boson Production at Future Linear Colliders

Dissertation
zur Erlangung des Doktorgrades
des Fachbereichs Physik
der Universität Hamburg

vorgelegt von
Fantina Madricardo
aus Venedig

Hamburg
2002

Gutachter der Dissertation:	Prof. Dr. B. A. Kniehl Prof. Dr. J. Bartels
Gutachter der Disputation:	Prof. Dr. B. A. Kniehl Prof. Dr. P. Zerwas
Datum der Disputation:	17.12.2002
Vorsitzender des Prüfungsausschusses:	Prof. Dr. G. Mack
Vorsitzender des Promotionsausschusses:	Prof. Dr. G. Huber
Dekan des Fachbereichs Physik:	Prof. Dr. F.-W. Büßer

ABSTRACT

In this work, we present the order α_s corrections of the process $e^+e^- \to t\bar{b}H^-$ and its charge conjugate counterpart within the minimal supersymmetric extension of the standard model. Large logarithmic corrections that arise in the on-mass-shell renormalization scheme for the quark mass in the $t\bar{b}H^-$ Yukawa coupling are resummed by adopting the modified minimal-subtraction scheme. The inclusion of the order α_s corrections leads to a significant reduction of the theoretical uncertainties due to scheme and scale dependence. We consider moreover the standard model process $e^+e^- \to t\bar{t}h$ and compute the order α_s corrections. We investigate the effect of electron and positron beam polarization and show that the cross sections of the considered processes can be largely enhanced by a suitable choice of the polarization.

ZUSAMMENFASSUNG

In dieser Arbeit werden die Korrekturen der Ordnung α_s zum Prozeß $e^+e^- \to t\bar{b}H^-$ und zu seinem ladungskonjugierten Gegenstück innerhalb der minimalen supersymmetrischen Verallgemeinerung des Standardmodells berechnet. Große logarithmische Korrekturen, die in der "on-mass-shell" Renormierung der Quarkmasse in der $t\bar{b}H^-$ Yukawa Kopplung vorkommen, werden mit Hilfe des modifizierten Minimal-Subtraktion-Schemas resummiert. Die Einbeziehung der Korrekturen zur Ordnung α_s führt zu einer erheblichen Reduktion der theoretischen Unsicherheit, die durch die Schema- und Skalenabhängigkeit hervorgerufen wird. Außerdem betrachten wir den Standardmodell-Prozeß $e^+e^- \to t\bar{t}h$ und berechnen die führende Korrekturen in α_s. Wir untersuchen den Effekt der Polarisation der Elektron- und Positronstrahlen und zeigen, daß die Wirkungquerschnitte der betrachteten Prozesse durch eine geeignete Wahl der Polarisation wesentlich erhöht werden können.

A Gilberto

Contents

1 Introduction **1**

2 Supersymmetry **5**

2.1 Motivation for supersymmetry 5

2.2 Generalities on supersymmetric Lagrangians 7

2.2.1 R parity 8

2.2.2 Soft supersymmetry breaking 8

2.3 The Minimal Supersymmetric Standard Model 10

2.3.1 Particle content 10

2.3.2 Higgs sector 12

2.3.3 Squark sector 15

2.3.4 Gluinos 17

2.3.5 Experimental limits 17

3 Single charged boson Higgs production **19**

3.1 Introduction 19

3.2 Lepton tensor 20

3.3 Born cross section 22

3.4 QCD corrections 24

3.4.1 Virtual corrections 24

3.4.2 Real corrections 28

3.4.3 Extraction of the IR divergences 31

3.5 SUSY QCD corrections 33

3.5.1 Cancellation of the UV divergences 35

3.6 Numerical results 37

3.6.1 Renormalization scheme and scale dependence 39

3.6.2 QCD corrections 43

3.6.3 SUSY QCD corrections 45

4 SM Higgs Boson Bremsstrahlung **53**
4.1 Introduction . . . 53
4.2 Born cross section . . . 54
4.3 QCD corrections . . . 55
4.3.1 Virtual corrections . . . 55
4.3.2 Real corrections . . . 56
4.4 Numerical results . . . 58

5 Higgs Boson production with polarized beams **63**
5.1 Introduction . . . 63
5.2 Beam polarization . . . 63
5.3 Polarized lepton tensor . . . 64
5.4 Polarized cross section for $e^+e^- \to t\bar{b}H^-$ . . . 66
5.4.1 Polarized Born cross section for $e^+e^- \to t\bar{b}H^-$ . . . 67
5.4.2 Polarized QCD- and SUSY QCD-corrected cross section for $e^+e^- \to t\bar{b}H^-$ . . . 71
5.5 Polarized cross section for $e^+e^- \to t\bar{t}h$ . . . 74

6 Conclusions **81**

A Loop Integrals **85**
A.1 UV divergent integrals . . . 85
A.2 IR divergent integrals . . . 87

B Born form factors **91**

C Four-particle phase space **95**

D Quark selfenergy **99**

Chapter 1

Introduction

The theoretical predictions of the Standard Model (SM) of electroweak and strong interactions [1] have met with impressive agreement the precision electroweak data accumulated in the past decade at the Large Electron Positron (LEP) collider at CERN (Geneva), at the Stanford Linear Collider (SLC) at SLAC, the Tevatron at Fermilab (Chicago) and elsewhere [2]. The SM is based on the gauge group $SU(3)_C \times SU(2)_L \times U(1)_Y$. The electroweak symmetry is broken down to $SU(3)_C \times U(1)_{em}$, in order to give mass to the particles of the theory. The Electroweak Symmetry Breaking (EWSB) is realized with the help of the Higgs mechanism [3], which requires the existence of a fundamental, complex scalar field, whose neutral component has a non-vanishing vacuum expectation value $v = (G_F\sqrt{2})^{-\frac{1}{2}} \simeq 246$ GeV. As a consequence of the Higgs mechanism, the weak gauge bosons, W and Z, and the fermions[1] acquire masses, and a physical degree of freedom representing the Higgs boson appears in the theory. After the discovery of the top quark in 1994 [5], only the discovery of the Higgs boson is missing in order to confirm the understanding of EWSB. The best direct limits on the SM Higgs mass, m_h, come from LEP, where the search for the Higgs boson via the process $e^+e^- \to Z^* \to Zh$ leads to a lower bound for the mass of 114.1 GeV at 95% C.L. [6]. The indirect bounds from precision electroweak observables are consistent with this number, and imply $m_h < 196$ GeV at 95% C.L. [2]. One of the prime objectives of a future e^+e^- linear collider (LC), like the TeV Energy Superconducting Linear Accelerator (TESLA), which is being developed and planned at DESY (Hamburg) [7], will be the detailed study of the properties of the Higgs boson.

Actually, the Higgs sector may have a more complicated structure than the one of

[1] Although in the SM the neutrinos are considered massless, the model can be easily extended to the case of massive neutrinos in agreement with the experimental results concerning neutrino oscillations [4].

the SM. The latter has been very successful until now, but there are several reasons to believe that it represents an accurate "effective low-energy theory", which cannot be valid up to very high energy scales. For example, it is clear that it has to be modified in order to incorporate the effects of gravity at the Plank scale ($M_{\text{Planck}} \sim 10^{19}$ GeV). However, if one assumes that the SM represents a valid description of particle physics up to a certain scale Λ, where $\Lambda \lesssim M_{\text{Planck}}$, quadratic divergences in Λ arise in the counterterm to the Higgs mass. Supersymmetric theories [8] represent an elegant way to solve this problem, also known as the "naturalness problem" [9]. Supersymmetry relates the fermionic and bosonic degrees of freedom of the theory. In particular, in supersymmetric extension of the SM each particle acquires a supersymmetric partner with the same transformation properties under the gauge symmetries, but with different spin. Since fermions and bosons contribute to the the Higgs mass counterterm with opposite signs, the quadratic divergences cancel. Moreover, by considering supersymmetry as a local symmetry a natural connection between gravity and supersymmetry can be established. Another very important reason is the unification of the couplings. The running coupling constants of the electromagnetic, weak and strong interactions in the context of the SM do not match exactly in one point as one would expect in grand unified theories. On the contrary, supersymmetry predicts new particles which influence the running of the couplings in such a way that they match around $M_X \sim 10^{16}$ GeV [10].

These reasons among others to be discussed in the next chapter motivate the choice of supersymmetry as the framework for this thesis. In particular, we will work in the context of the Minimal Supersymmetric Standard Model (MSSM) [11, 12, 13], which is the simplest low-energy supersymmetric extension of the SM. In the MSSM, the Higgs sector consists of a two-Higgs-doublet model (2HDM) and accommodates five physical Higgs bosons: the neutral CP-even h^0 and H^0 bosons, the neutral CP-odd A^0 boson and the charged $H^{\pm}$-boson pair. The 2HDM has six free parameters, which are usually taken to be the masses m_{h^0}, m_{H^0}, m_{A^0}, and $m_{H^{\pm}}$, the ratio $\tan\beta = v_2/v_1$ of the vacuum expectation values of the two Higgs doublets, and the weak mixing angle α that relates the weak and mass eigenstates of h^0 and H^0. At the tree level, the MSSM Higgs sector has just two free parameters, which are usually taken to be m_{A^0} and $\tan\beta$.

The discovery of the charged Higgs bosons would be a significant step towards the understanding of EWSB, as it would prove the SM incomplete and, at the same time give strong support to the 2HDM and the MSSM. If the $H^{\pm}$ bosons have mass $m_H < m_t - m_b$, they will be mainly produced through the $t \to bH^+$ decays of top quarks, which are copiously generated singly or in pairs at an e^+e^- LC [14]. On the other hand, if there is sufficient center-of-mass (c.m.) energy available, $\sqrt{s} > 2m_H$, then charged-Higgs-

boson pair production, $e^+e^- \to H^+H^-$ will be the dominant production mechanism [14]. Otherwise, if $m_H > \max(m_t - m_b, \sqrt{s}/2)$, the $H^\pm$ bosons can still be produced singly. There are various mechanisms of single-charged-Higgs-boson production [15]. The most important of them are $e^+e^- \to W^+H^-$, which proceeds through quantum loops involving SM [16, 17] and possibly supersymmetric [16] particles, $e^+e^- \to \tau^+\nu_\tau H^-$ [15, 18], and $e^+e^- \to t\bar{b}H^-$ [15, 19]. The results for these three processes have been compared for different values of m_H and $\tan\beta$ [20] and it turns out that in certain parts of the parameter space the process $e^+e^- \to t\bar{b}H^-$ is dominant. Furthermore, this process can provide interesting constraints on $\tan\beta$ as is shown in Ref. [21].

For these reasons, we dedicate the main part of this thesis to the study of the process $e^+e^- \to t\bar{b}H^-$. The leading order results present a dramatic renormalization scheme and scale dependence. Therefore, we consider the dominant quantum corrections to $e^+e^- \to t\bar{b}H^-$ cross section, which arise from quantum chromodynamics (QCD) [22]. This leads to one-loop $2 \to 3$ diagrams with a gluon exchange, which yield the virtual corrections, and to $2 \to 4$ diagrams of the tree level type, where a gluon is radiated by a quark in the final state. The latter give rise to the real corrections. To complete the calculation to order α_s, we present the results for SUSY QCD corrections as well. These are given by $2 \to 3$ diagrams with one closed loop, which includes gluinos and squarks. We find that the renormalization scheme and scale dependence are greatly reduced by the introduction of the next-to-leading order radiative corrections.

In order to check the calculation for the corrections to $e^+e^- \to t\bar{b}H^-$, the SM process $e^+e^- \to t\bar{t}h$ has been considered. This reaction represents an essential tool to measure the SM $t\bar{t}h$ Yukawa coupling and has already been investigated in Ref. [19] at the Born level and to order α_s in Refs. [23, 24]. We compute the virtual and real QCD corrections relevant to this process, and confirm the results obtained in Refs. [23, 24]. This agreement yields important checks for the parameterization of the phase space and for a subsection of diagrams in the reaction $e^+e^- \to t\bar{b}H^-$.

Another important point to be discussed is the polarization of the electron and positron beams, since a suitable choice of the beam polarization can significantly enhance the cross sections and suppress the background. Already in its basic running mode of a e^+e^- LC, the electron beam can be polarized to around 80% with the help of a strained photocathode technology, similar to that used at the SLC [7]. The polarization of the positron beam should be possible as well up to 40-60%, representing, however, a much more difficult experimental task. In this work, we present extensive studies for the processes $e^+e^- \to t\bar{b}H^-$ and $e^+e^- \to t\bar{t}h$ with polarized electron and positron beams.

The outline of the thesis is the following: in the next chapter, we discuss our theoretical

framework, presenting an introduction to supersymmetric theories and to the MSSM. In Chapter 3, we describe in detail the analytical calculation of the next-to-leading order cross section for $e^+e^- \to t\bar{b}H^-$ and its charge conjugate $e^+e^- \to b\bar{t}H^+$, and present the corresponding numerical results for energies accessible at TESLA. In Chapter 4, we discuss the computation of the SM process $e^+e^- \to t\bar{t}h$, including the QCD corrections and present updated numerical results for the cross section. The influence of the beam polarization on the results for these cross sections is investigated in Chapter 5. Finally, in Chapter 6 we draw our conclusions.

Lengthy expressions are relegated to the appendices. In Appendix A, we give the expressions for the integrals arising in the calculation. In Appendix B, we list the analytical results for the Born form factors for the processes $e^+e^- \to t\bar{b}H^-$ and $e^+e^- \to t\bar{t}h$. In Appendix C, we present a general parameterization of the four-particle phase space for four different massive particles in the final state, while in Appendix D, we summarize the results for the quark self-energies, used for the computation of our counterterms.

Chapter 2

Supersymmetry

2.1 Motivation for supersymmetry

Although the SM [1] can describe the experimental results with very high precision [2], there are several reasons to believe that it represents just an effective theory. In other words, the SM can not be valid up to arbitrarily high energies.
If we get closer to the Plank scale $M_{\text{Plank}} = 1/\sqrt{G_{\text{Newton}}} \sim 1.2 \cdot 10^{19}$ GeV, for example, the gravitational force between the particles becomes as strong as the other elementary forces. As the SM does not include gravity, it can not be a complete description of nature at such energy scales.

The simplest extension of the SM is the Minimal Supersymmetric Standard Model (MSSM) [11, 12, 13]. This model is able to explain the experimental data in the context of Supersymmetry (SUSY) [8] very precisely as well. Moreover, it allows to answer several fundamental questions, which are left open in the SM and, at the same time, presents remarkable properties. Let us mention the most important ones:

1. "Hierarchy" and "naturalness" problems: the particles observed until now have masses of the order of magnitude of the W boson mass $m_W \sim 10^2$ GeV. On the other hand, the strong and electroweak interactions should unify at a scale near to $M_{\text{GUT}} \sim 2 \cdot 10^{16}$ GeV according Grand Unified Theories (GUTs) [25]). Why are these apparently fundamental disparate scales present in the theory? The existence of these huge hierarchies in the theory represents the so called "hierarchy problem" [26] and induces the instability of the Higgs mass in the SM. If we try to extend the SM to a scale $\Lambda \sim M_{\text{GUT}}$, we encounter the so called "naturalness" problem for the Higgs mass [9]. While the lower bound on the Higgs mass comes from the experiments, arguments based on perturbative unitarity and triviality suggest

that self-consistency of the SM is broken unless $m_h < \mathcal{O}(1\text{ TeV})$. However, m_h is extremely unstable if we consider radiative corrections. At the lowest order m_h is equal to the bare mass $m_{h,0}$, while at one-loop, we will have $m_{h,0}^2 = m_h^2 + \delta m_h^2$, with δm_h^2 being quadratically divergent in Λ, where the divergences arise from the fermion loops in the Higgs self-energy. This means that $m_{h,0}^2$, $\delta m_h^2 \sim \Lambda^2 \sim 10^{32}\,\text{GeV}^2$ and at the same time the condition $m_{h,0}^2 - \delta m_h^2 = m_h^2 \sim 10^4\,\text{GeV}^2$ has to be satisfied. In other words, $m_{h,0}^2$ and δm_h^2 have to cancel up to 28 orders of magnitude at each order of the perturbation theory. The necessity of such a fine tuning represents the "naturalness problem".
With the introduction of SUSY this problem disappears: the scalar SUSY particles associated with the fermions give an additional quadratically divergent contribution to δm_h^2, which cancels exactly the quadratic divergences.

2. Connection to supergravity: gravitation as a fourth fundamental force could not be included in Grand Unification Theories up to now. If we consider SUSY as a local symmetry, we find that the Lorentz-algebra, the algebra of the General Relativity Theory, is a part of the local SUSY-algebra [27], as invariance under local supersymmetry transformations implies invariance under local coordinate changes. Thanks to local supersymmetry, also called Supergravity (SUGRA), we obtain a natural connection between supersymmetry and gravitation. Indeed, almost all attempts of quantizing gravity are based on superstrings models, which assume a $N = 1$ supersymmetry as a low energy limit.

3. Haag-Lopuszanski-Sohnius-Theorem [28]: another striking argument for SUSY is the result of the Haag-Lopuszanki-Sohnius-theorem. This theorem shows that the biggest symmetry, that a non trivial quantum field theory (QFT) can have is an internal gauge symmetry $\times$ a (local) SUSY. The internal gauge symmetry is realized by $SU(3)_C \times SU(2)_L \times U(1)_Y$.

4. Coupling unification: the running coupling constants of the electromagnetic, weak and strong interactions in the context of the SM do not match exactly in one point as one would expect in grand unified theories. On the contrary, the MSSM predicts new particles which influence the running of the couplings in such a way that they match around $M_X \sim 10^{16}$ GeV [10].

4. Dark matter: from the rotation of the galaxies there is experimental evidence for the existence of non baryonic dark matter. While the SM does not have any candidate

for dark matter[1], in the MSSM the lightest SUSY particle (LSP) is stable and therefore represents an optimal candidate to explain the presence of dark matter in the universe.

2.2 Generalities on supersymmetric Lagrangians

Supersymmetric field theories [29] are based on the supersymmetry algebra [30], an extension of the Poincaré algebra. Because of the Coleman-Mandula theorem [31], this extension can be obtained only by adding some generators of fermionic characters, obeying anticommutation relations. We consider here the phenomenology-viable case of simple $N = 1$ supersymmetry, with N referring to the number of supersymmetries. Defining the fermionic supersymmetry generator and its hermitian conjugate Q_α and $\bar{Q}_{\dot{\beta}} = (Q_\beta)^\dagger$, respectively, the supersymmetry algebra is defined by the following relations:

$$\begin{aligned} \left\{Q_\alpha, \bar{Q}_{\dot{\beta}}\right\} &= 2\left(\sigma^\mu\right)_{\alpha\dot{\beta}} P_\mu, \\ \{Q_\alpha, Q_\beta\} &= \left\{\bar{Q}_{\dot{\alpha}}, \bar{Q}_{\dot{\beta}}\right\} = 0, \end{aligned} \tag{2.1}$$

where $\sigma^\mu = (\mathbf{1}, \sigma^i)$ and $\bar{\sigma}^\mu = (\mathbf{1}, -\sigma^i)$ are the Pauli matrices, P_μ is the space-time momentum operator. Q_α transforms as a left handed Weyl spinor, a $(1/2, 0)$ representation under Lorenz transformations. As the supersymmetry transformations are global (independent of position in spacetime) we have that $[Q_\alpha, P_\mu] = [\bar{Q}_{\dot{\beta}}, P_\mu] = 0$.

To construct supersymmetric Lagrangians, it is convenient to work in superspace, which can be obtained adding to the ordinary space variables x_μ, the anticommuting Grassmann variables θ and $\bar{\theta}$. A superfield is a function of the superspace variables and is indicated by a symbol with a caret on it, in order to distinguish it from the usual fields. In globally supersymmetric extensions of the SM, there are two types of superfields, the chiral and gauge superfields. They contain equal numbers of bosonic and fermionic degrees of freedom. The chiral superfields $\hat{\phi}$ contain a complex spin-0 field ϕ, a Weyl fermion ψ and a complex scalar F, which represents an auxiliary field with no kinetic energy term. That is its equations of motions are purely algebraic and it can be re-expressed in terms of other dynamical fields. In the Wess-Zumino gauge, the gauge superfields $\hat{V}$ contain a real spin-1 field V_μ, a Majorana spinor λ and a real scalar auxiliary field D. To obtain the components of the superfield, one has to expand it in terms of θ and $\bar{\theta}$.

Given a simple gauge group G, with generators T^a and gauge coupling g, one can write the most general supersymmetric, gauge invariant, renormalizable Lagrangian in

[1]Actually, a possible candidate coul be the neutrino, but this option is arleady excluded by the experiments.

terms of the superfield components [29]. After elimination of the auxiliary fields via their equations of motions:

$$\mathcal{L} = -\frac{1}{4}F^a_{\mu\nu}F^{\mu\nu a} + \frac{i}{2}\bar{\lambda}^a\gamma^\mu D_\mu\lambda^a + \left(D^\mu\phi\right)^\dagger_i \left(D_\mu\phi\right)^i + \frac{i}{2}\bar{\psi}_i\gamma^\mu D_\mu\psi^i \tag{2.2}$$
$$+ \left[i\sqrt{2}g\bar{\psi}_i\left(\lambda T^a\phi\right)^i + h.c.\right] - \frac{1}{2}\left[\frac{\partial^2 W}{\partial\phi^i\phi^j}\bar{\psi}^{c^i}\psi^j + h.c.\right] - V\left(\phi,\phi^\dagger\right),$$

where $F^a_{\mu\nu} = \partial_\mu A^a_\nu - \partial_\nu A^a_\mu + ig[A^b_\mu, A^c_\nu]$ is the strength field, $D^\mu = \partial^\mu + igA^\mu$ the gauge covariant derivative, V is the scalar potential:

$$V = F^*_i F^i + \frac{g^2}{2}D^a D^a = \sum_i \left|\frac{\partial W}{\partial\phi^i}\right|^2 + \sum_a \frac{g^2}{2}\left[\phi^*_i (T^a)^i_j \phi^j\right]^2 \geq 0, \tag{2.3}$$

where $W(\phi)$ is a gauge-invariant polynomial of degree three in the fields ϕ^i, called *superpotential*, and i, j run over the number of chiral supermultiplets in the theory. Note that by construction the superpotential is an analytic function of the scalar fields ϕ^i treated as a complex variable.

2.2.1 R parity

In the SM the $SU(3)_C \times SU(2)_L \times U(1)_Y$ gauge invariance is sufficient to guarantee that all the terms in the Lagrangian of dimension 4 or less conserve baryon (B) and lepton (L) number. In the MSSM this is no longer true. Since B and L violating processes have never been seen experimentally, one has to add a new symmetry which allows only B and L conserving terms in the Lagrangian. This symmetry is a discrete symmetry, called "R-parity" [32], and it is defined as follows:

$$R = (-1)^{3(B-L)+2S}, \tag{2.4}$$

where S represent the spin of the particle. SM particles and Higgs bosons have even R-parity ($R = +1$), while all the squarks, sleptons, gauginos and higgsinos have odd R-parity ($R = -1$). As a consequence the lightest supersymmetric particle (LSP) has to be absolutely stable. Hence, if it is neutral, it represents an attractive candidate for the non-baryonic dark matter required by cosmology. Moreover, the conservation of R-parity implies that supersymmetric particles can be produced experimentally only in pairs.

2.2.2 Soft supersymmetry breaking

Until now we have considered an unbroken supersymmetric theory. However, to construct a realistic model of low-energy physics, supersymmetry has to be broken. If SUSY were

not broken, the supersymmetric partners of the SM particles should have been already observed in the experiments. Using Eq. (2.2), one can express the Hamiltonian function H in terms of the supersymmetry algebra generators:

$$\sum_{\alpha=1}^{2} \left\{ Q_\alpha, \bar{Q}_{\dot{\alpha}} \right\} = 4P_0 = 4H. \tag{2.5}$$

From this equation follows that H is semi-positive definite. Then, supersymmetry is spontaneously broken if and only if the vacuum energy, $E_{vac} = \langle 0|H|0\rangle$, is strictly positive. If a state $|0\rangle$ exists for which $Q_\alpha|0\rangle = 0$ and $\bar{Q}_{\dot{\alpha}}|0\rangle = 0$, this state is the *true* vacuum, as $\langle 0|H|0\rangle = E_{vac} \geq 0$ and supersymmetry is unbroken. On the other hand, if $E_{vac} \geq 0$ follows immediately that supersymmetry is spontaneously broken. Since $\langle 0|H|0\rangle = \langle 0|V|0\rangle$, where V is given in Eq. (2.3), there can be two mechanisms for the spontaneous supersymmetry breaking:

$$\langle 0|F_i|0\rangle \neq 0 \qquad \text{O'Raifeartaigh breaking mechanism [33]} \tag{2.6}$$

$$\langle 0|D^a|0\rangle \neq 0 \qquad \text{Fayet-Iliopoulos breaking mechanism [34]} \tag{2.7}$$

However, in the past there have been several attempts to set in practice one of these mechanisms inside the MSSM. Unfortunately, all these proposals have failed. In fact, the mass sum rules require at least some of the superpartners in a supermultiplet to be lighter than their SM counterparts. These light superpartners have not been observed by the experiments. A way to circumvent the problem is to think that there is an additional "hidden" sector where supersymmetry is broken spontaneously, which does not couple to the SM particles. The informations about the spontaneous symmetry breaking are then communicated to the MSSM via interactions shared by both sectors. There are several models to describe this mechanism. We already mentioned supergravity in the introduction, where the information from the hidden sector is mediated by the gravitational interaction. Other scenarios have been proposed like the Gauge-Mediated Supersymmetry Breaking (GMSB) scenario (for a review on this topic see [35]) where the information about supersymmetry breaking is transmitted to the visible sector via gauge forces.

In the MSSM, one normally introduces an explicit soft supersymmetry breaking term in the low-energy effective Lagrangian. This term, $\mathcal{L}_{soft}$, is explicitly not supersymmetric, but "soft" (of positive mass dimension) in order to not introduce new quadratic divergences in the theory. In this way, what we do not know about the supersymmetry breaking mechanism at high energy scale is contained in the general parameters of the soft SUSY breaking term. All the possible quantities which satisfy this condition have been found by Girardello and Grisaru [36]. They are of the type:

- $m^2\phi\phi^*,\ m^2(\phi^2+\phi^{*2})$,
  mass terms for the scalar fields,
- $m_\lambda\bar{\lambda}\lambda + \text{h.c.}$,
  mass terms for the gauginos,
- $\mu(\phi^3+\phi^{*3})$,
  trilinear scalar interaction terms.

Clearly, $\mathcal{L}_{soft}$ breaks supersymmetry, since it involves only scalars and gauginos, and not their respective superpartners.

2.3 The Minimal Supersymmetric Standard Model

2.3.1 Particle content

To obtain the minimal supersymmetric extension of the SM one has to add to each known SM particle a supersymmetric partner, called *superpartner*. A particle and its superpartner differ by one half unit of spin and have the same transformation properties under the SM gauge group $G \equiv SU(3)_C \times SU(2)_L \times U(1)_Y$ and the MSSM Lagrangian is given by the minimal renormalizable Lagrangian with global $N = 1$ supersymmetry. We will have then new spin-$\frac{1}{2}$ Majorana fields associated to the SM electroweak bosons and gluons, called "gauginos" and "gluinos", respectively. Moreover, we will have a complex spin-0 field for each quark or lepton chirality state, the "squarks" $\tilde{q}_L \equiv (\tilde{u}_L\ \tilde{d}_L)^T, \tilde{u}_R, \tilde{d}_R$ and the "sleptons" $\tilde{l}_L \equiv (\tilde{\nu}_L\ \tilde{e}_L)^T, \tilde{e}_R$, in three generations as their fermionic superpartners. For each generation one has to introduce a chiral superfield, therefore we will have the superfields $\hat{Q}, \hat{L}, \hat{U}, \hat{D}$ and $\hat{E}$, whose fermionic components are q_L, l_L, u_L^C, d_L^C and e_L^C, respectively. Finally we have to introduce multiplets containing the spin-0 degrees of freedom necessary for the Higgs mechanism. However, the superpartners of the Higgs bosons are chiral fermions which contribute to the $SU(2)_L \times U(1)_Y$ gauge anomaly. In order to have an anomaly-free theory and to give masses to all the fermions, we have to introduce at least two Higgs doublet chiral superfields, $\hat{H}_1$ and $\hat{H}_2$. They contain the $SU(2)_L$-doublet Higgs fields $H_1 = (H_1^0, H_1^-), H_2 = (H_2^+, H_2^0)$, and the associated spinor fields $(\tilde{H}_1^0, \tilde{H}_1^-), (\tilde{H}_2^+, \tilde{H}_2^0)$. They have opposite hypercharge, so that the contributions of the higgsinos to the gauge anomalies will cancel. All the superfields and their components are listed in table 2.1.

We have written down just the first generation of quarks and leptons. We indicate with $i = 1, 2, 3$ and with $a = (1, \ldots, 8)$ the index of the $SU(2)_L$ and $SU(3)_C$ generators,

Superfields	Boson fields	Fermion fields	$SU(3)_C$	$SU(2)_L$	$U(1)_Y$
Gauge fields					
$\hat{V}'$	B_μ	λ'	1	1	0
$\hat{V}^i$	W^i_μ	λ^i	1	3	0
$\hat{V}^a_s$	G^a_μ	λ^a_s	8	1	0
Matter fields					
$\hat{L}$	$\begin{pmatrix} \tilde{\nu}_L \\ \tilde{e}_L \end{pmatrix}$	$\begin{pmatrix} \nu_L \\ e_L \end{pmatrix}$	1	2	-1
$\hat{E}$	$\tilde{e}^*_R$	e^C_L	1	1	2
$\hat{Q}$	$\begin{pmatrix} \tilde{u}_L \\ \tilde{d}_L \end{pmatrix}$	$\begin{pmatrix} u_L \\ d_L \end{pmatrix}$	3	2	1/3
$\hat{U}$	$\tilde{u}^*_R$	u^C_L	3^*	1	$-4/3$
$\hat{D}$	$\tilde{d}^*_R$	d^C_L	3^*	1	2/3
Higgs fields					
$\hat{H}_1$	$\begin{pmatrix} H^0_1 \\ H^-_1 \end{pmatrix}$	$\begin{pmatrix} \tilde{H}^1_0 \\ \tilde{H}^-_1 \end{pmatrix}$	1	2	-1
$\hat{H}_2$	$\begin{pmatrix} H^+_2 \\ H^0_2 \end{pmatrix}$	$\begin{pmatrix} \tilde{H}^+_2 \\ \tilde{H}^0_2 \end{pmatrix}$	1	2	1

Table 2.1: Superfields and particles of the MSSM.

respectively. The reported numbers for the gauge groups $SU(2)_L$ and $SU(3)_C$ give the dimension of the representation, while the number for $U(1)_Y$ represents the hypercharge number. Gauginos and higgsinos can mix. This means that the physical mass eigenstates are linear combinations of the gauge eigenvalues encountered until now. These mass eigenvalues are called charginos and neutralinos. In the same way, we can have mixing in the squark and slepton sectors. In this case the mass eigenvalue will be indicated with the subscript $1, 2$ instead of L, R. In Sec. 2.2, we have seen how to write down a supersymmetric Lagrangian. However, the superpotential has still to be given to complete the description of the model. The most general R-parity invariant superpotential read [13, 37]:

$$W = \mu \hat{H}_1 \hat{H}_2 + y_U \hat{Q} \hat{U} \hat{H}_2 + y_D \hat{Q} \hat{D} \hat{H}_1 + y_E \hat{L} \hat{E} \hat{H}_1, \tag{2.8}$$

where the dimensionless Yukawa coupling y_U, y_D, y_E are 3×3 matrices with two generation indices. Here we have suppressed all the gauge and family indices.

Finally, the expression for $\mathcal{L}_{soft}$ that has to be summed to the supersymmetric Lagrangian $\mathcal{L}_{SUSY}$ is given by:

$$\begin{aligned}\mathcal{L}_{soft} &= -\sum_i \tilde{m}_i|\phi^i|^2 - \frac{1}{2}\sum_A M_A\bar{\lambda}^A\lambda^A - \Big(y_U A_U\hat{Q}\hat{U}\hat{H}_2 + \\ &\quad + y_D A_D\hat{Q}\hat{D}\hat{H}_1 + y_E A_E\hat{L}\hat{E}\hat{H}_1 + m_{12}^2\hat{H}_1\hat{H}_2 + \text{h.c.}\Big)\,,\end{aligned} \tag{2.9}$$

where ϕ^i denotes the generic spin-0 field with $i = H_1, H_2, Q, U, D, L, E$ and λ_A the generic gaugino field with $A = 1, 2, 3$. Also A_U, A_D and A_E are matrices in the generation space.

The full expression of the MSSM Lagrangian can be found in Ref. [13]. In the following subsections, we consider in detail the sector of the model which arise in our calculation, paying special attention to the diagonalization of the mass matrices in the Higgs and squark sectors.

2.3.2 Higgs sector

We have already mentioned that the two Higgs doublets H_1 and H_2, contained in the Higgs superfields, have opposite hypercharge, $Y_1 = -1$ and $Y_2 = +1$, respectively. Both have a non vanishing vacuum expectation value (VEV), v_1 and v_2:

$$\langle H_1\rangle = \begin{pmatrix} v_1 \\ 0 \end{pmatrix}, \qquad \langle H_2\rangle = \begin{pmatrix} 0 \\ v_2 \end{pmatrix}. \tag{2.10}$$

Therefore, we can re-express them as follows:

$$\begin{aligned} H_1 &= \begin{pmatrix} H_1^0 \\ H_1^- \end{pmatrix} = \begin{pmatrix} v_1 + \frac{1}{\sqrt{2}}(\phi_1^0 + i\chi_1^0) \\ -\phi_1^- \end{pmatrix} \\ H_2 &= \begin{pmatrix} H_2^+ \\ H_2^0 \end{pmatrix} = \begin{pmatrix} \phi_2^+ \\ v_2 + \frac{1}{\sqrt{2}}(\phi_2^0 + i\chi_2^0) \end{pmatrix}. \end{aligned} \tag{2.11}$$

The ratio of VEVs is defined as $\tan\beta \equiv v_2/v_1$, where $0 < \beta < \pi/2$.

Usually, it is assumed that squarks and sleptons have vanishing VEVs. Thus, to obtain the electroweak gauge symmetry breaking , it is enough to study the behaviour of the Higgs potential with all explicit soft breaking terms [13, 37]:

$$\begin{aligned} V = m_1^2|H_1|^2 + m_2^2|H_2|^2 - m_{12}^2\left(\epsilon_{ij}H_1^iH_2^j + \text{h.c.}\right) \\ + \frac{1}{8}(g^2 + g'^2)\left(|H_1|^2 - |H_2|^2\right)^2 + \frac{1}{2}g^2|H_1^\dagger H_2|^2, \end{aligned} \tag{2.12}$$

where $\epsilon_{ij} = -\epsilon_{ji}$ with $\epsilon_{12} = 1$,

$$m_1^2 \equiv |\mu|^2 + \tilde{m}_{H_1}^2, \qquad m_2^2 \equiv |\mu|^2 + \tilde{m}_{H_2}^2, \tag{2.13}$$

$\tilde{m}_{H_1}, \tilde{m}_{H_1}$, and m_{12}^2 are the soft breaking parameters seen in the previous section, whereas g and g' represent the $SU(2)$ and $U(1)$ gauge couplings, respectively. The potential has a minimum for $H_1 = \langle H_1 \rangle$ and $H_2 = \langle H_2 \rangle$, assuming that m_{12}^2 is positive, which is not restrictive.

The $SU(2)_L \times U(1)_Y$ breaking down to $U(1)_{em}$ occurs if we impose the conditions:

$$\begin{aligned} m_1^2 + m_2^2 &\geq 2|m_{12}^2| \qquad \text{(for the potential to be bounded from below)}, \\ m_{12}^4 &\geq m_1^2 m_2^2 \qquad \text{(to get non} - \text{vanishing VEVs at the minimum)}. \end{aligned} \tag{2.14}$$

If we define the variable $v^2 \equiv v_1^2 + v_2^2$, the condition for the potential to be minimized can be written as follows:

$$\sin 2\beta = \frac{-2m_{12}^2}{m_1^2 + m_2^2}, \qquad v^2 = \frac{4}{g^2 + g'^2} \frac{m_1^2 - m_2^2 \tan\beta}{\tan^2\beta - 1}. \tag{2.15}$$

We start with eight real scalar degrees of freedom. Three of these are absorbed by the Goldstone bosons G^0 and $G^\pm$. The remaining five yield the physical Higgs bosons of the model:

- two CP-even neutral Higgs bosons, h^0, H^0,
- a CP-odd neutral Higgs boson A^0,
- two charged Higgs bosons $H^\pm$.

These represent mass eigenstates and if we indicate the general Higgs field in the potential by φ, they can be obtained diagonalizing the mass matrix:

$$M_{ij}^2 = \frac{1}{2} \frac{\partial^2 V}{\partial\varphi_i \partial\varphi_j}\bigg|_{minimum}, \tag{2.16}$$

where at the minimum we impose $\langle 0|\varphi_i|0\rangle = 0$. The diagonalization of the mass matrix can be obtained with the help of the following transformation:

$$\begin{pmatrix} H^0 \\ h^0 \end{pmatrix} = \begin{pmatrix} \cos\alpha & \sin\alpha \\ -\sin\alpha & \cos\alpha \end{pmatrix} \begin{pmatrix} \phi_1^0 \\ \phi_2^0 \end{pmatrix}, \tag{2.17}$$

$$\begin{pmatrix} G^0 \\ A^0 \end{pmatrix} = \begin{pmatrix} \cos\beta & \sin\beta \\ -\sin\beta & \cos\beta \end{pmatrix} \begin{pmatrix} \chi_1^0 \\ \chi_2^0 \end{pmatrix}, \tag{2.18}$$

$$\begin{pmatrix} G^\pm \\ H^\pm \end{pmatrix} = \begin{pmatrix} \cos\beta & \sin\beta \\ -\sin\beta & \cos\beta \end{pmatrix} \begin{pmatrix} \phi_1^\pm \\ \phi_2^\pm \end{pmatrix}, \tag{2.19}$$

where we have introduced the mixing angle α which is conventionally chosen such that $-\frac{\pi}{2} \leq \alpha \leq 0$ and is given by

$$\cos 2\alpha = -\cos 2\beta \left(\frac{m_{A^0}^2 - m_Z^2}{m_{H^0}^2 - m_{h^0}^2} \right), \qquad \sin 2\alpha = -\sin 2\beta \left(\frac{m_{H^0}^2 + m_{h^0}^2}{m_{H^0}^2 - m_{h^0}^2} \right), \tag{2.20}$$

where m_Z is the mass of the Z boson.

The parameters of the Higgs potential can be re-expressed in terms of physical parameters. First, we have that

$$m_W^2 = m_Z^2 c_w^2 = \frac{1}{4}(v_1^2 + v_2^2), \tag{2.21}$$

with $s_w^2 = 1 - c_w^2 = 1 - m_W^2/m_Z^2$ being the sine square of the weak mixing angle. Thus, $(v_1^2 + v_2^2) \simeq 246$ GeV. Secondly,

$$m_{A^0}^2 = \frac{m_{12}^2}{\sin\beta\cos\beta}. \tag{2.22}$$

In the end, we are left with two free parameters which fix the Higgs boson masses and couplings. These are conventionally chosen to be m_{A^0} and $\tan\beta$.
At tree level, the masses of the other physical Higgs particles can be expressed in terms of m_{A^0}, m_Z and $\tan\beta$:

$$\begin{aligned} m_{H^0,h^0}^2 &= \frac{1}{2}\left[m_{A^0}^2 + m_Z^2 \pm \sqrt{(m_{A^0}^2 + m_Z^2) - 4 m_Z^2 m_{A^0}^2 \cos^2 2\beta} \right], \\ m_{H^\pm}^2 &= m_{A^0}^2 + m_W^2, \end{aligned} \tag{2.23}$$

where conventionally $m_{h^0} \leq m_{H^0}$. These tree-level relations imply the following mass hierarchies:

$$\begin{aligned} m_{H^0}^2 &\geq m_{A^0}^2, m_Z^2 \\ m_{H^\pm}^2 &\geq m_W^2 \\ m_{h^0}^2 &\leq m_Z^2 \cos\beta \leq m_Z^2. \end{aligned} \tag{2.24}$$

The last limit is already ruled out by experiment. However, if one consider the radiative corrections to the Higgs masses, the upper limit for m_{h^0} is shifted to ~ 135 GeV, so that it is still compatible with the experimental results. For a recent review on Higgs phenomenology see Ref. [38].

2.3.3 Squark sector

The squark mass term in the Lagrangian for a squark $\tilde{q}$ is given by

$$\mathcal{L}_{m_{\tilde{q}}} = -\left(\tilde{q}_L^\dagger, \tilde{q}_R^\dagger\right) M_{\tilde{q}}^2 \begin{pmatrix} \tilde{q}_L \\ \tilde{q}_R \end{pmatrix}, \tag{2.25}$$

with the mass matrix

$$\begin{aligned} M_{\tilde{u}}^2 &= \begin{pmatrix} \tilde{m}_Q^2 + m_Z^2 \cos 2\beta\,(I_u - Q_u s_w^2) + m_u^2 & m_u(A_u^* - \mu \cot\beta) \\ m_u(A_u - \mu^* \cot\beta) & \tilde{m}_U^2 + m_Z^2 \cos 2\beta\, Q_u s_w^2 + m_u^2 \end{pmatrix}, \\ M_{\tilde{d}}^2 &= \begin{pmatrix} \tilde{m}_Q^2 + m_Z^2 \cos 2\beta\,(I_d - Q_d s_w^2) + m_d^2 & m_d(A_d^* - \mu \tan\beta) \\ m_d(A_d - \mu^* \tan\beta) & \tilde{m}_D^2 + m_Z^2 \cos 2\beta\, Q_d s_w^2 + m_d^2 \end{pmatrix}, \end{aligned} \tag{2.26}$$

where A_u, A_d are the diagonal elements of the matrices A_U and A_D, respectively.
The matrices in the preceding equation can be diagonalized with the help of the unitary matrices S^q:

$$S^q M_{\tilde{q}}^2 S^{q\dagger} = \begin{pmatrix} m_{\tilde{q}_1}^2 & 0 \\ 0 & m_{\tilde{q}_2}^2 \end{pmatrix}. \tag{2.27}$$

The gauge eigenstates $\tilde{q}_L$ and $\tilde{q}_R$ and mass eigenstates $\tilde{q}_1$ and $\tilde{q}_2$ are related by the following equations:

$$\begin{aligned} \tilde{q}_1 &= S_{11}^q\, \tilde{q}_L + S_{12}^q\, \tilde{q}_R\ , \\ \tilde{q}_2 &= S_{21}^q\, \tilde{q}_L + S_{22}^q\, \tilde{q}_R\ . \end{aligned} \tag{2.28}$$

In general, the entries of the unitary matrices S_q are complex. However, if one assumes them to be real parameters, one can express them through the mixing angle $\theta_{\tilde{q}}$, defining $\cos\theta_{\tilde{q}} = S_{11}^q = S_{22}^q$ and $\sin\theta_{\tilde{q}} = S_{12}^q = -S_{21}^q$. Thus, one can rewrite Eq. (2.28) as follows:

$$\begin{aligned} \tilde{q}_1 &= \cos\theta_{\tilde{q}}\, \tilde{q}_L + \sin\theta_{\tilde{q}}\, \tilde{q}_R\ , \\ \tilde{q}_2 &= -\sin\theta_{\tilde{q}}\, \tilde{q}_L + \cos\theta_{\tilde{q}}\, \tilde{q}_R\ . \end{aligned} \tag{2.29}$$

After this transformation, the squark mass term in the Lagrangian reads:

$$\mathcal{L}_{m_{\tilde{q}}} = -m_{\tilde{q}_1}^2\, |\tilde{q}_1|^2 - m_{\tilde{q}_2}^2\, |\tilde{q}_2|^2\ . \tag{2.30}$$

The parameters $\tilde{m}_Q^2, \tilde{m}_U^2, \tilde{m}_D^2$ and A_u, A_u in Eq. (2.26) are in general complex. However, for our analysis, we have chosen to work in the minimal supergravity (mSUGRA) scenario, where the MSSM soft breaking parameters obey a set of boundary conditions at the GUT scale. Besides the unification of the gauge coupling constants, the unification and universality conditions are:

- Unification of the gaugino masses:

$$M_1(M_{\rm GUT}) = M_2(M_{\rm GUT}) = M_3(M_{\rm GUT}) \equiv m_{\frac{1}{2}} \tag{2.31}$$

- Universal scalar masses:

$$\begin{aligned} \tilde{m}_Q(M_{\rm GUT}) = \tilde{m}_U(M_{\rm GUT}) = \tilde{m}_D(M_{\rm GUT}) = \tilde{m}_L(M_{\rm GUT}) = \tilde{m}_E(M_{\rm GUT}) \\ \tilde{m}_{H_1}(M_{\rm GUT}) = \tilde{m}_{H_2}(M_{\rm GUT}) \equiv m_0 \end{aligned} \tag{2.32}$$

- Universal trilinear couplings:

$$A_U^{ij}(M_{\rm GUT}) = A_D^{ij}(M_{\rm GUT}) = A_E^{ij}(M_{\rm GUT}) \equiv A_0 \delta^{ij}. \tag{2.33}$$

The conditions in Eqs. (2.14) tell us that the electroweak symmetry breaking is only possible for a positive value of μ^2. The sign of μ is not determined. Therefore, this model has only four continues parameters and an unknown sign:

$$\tan\beta, m_{\frac{1}{2}}, m_0, A_0, {\rm sign}(\mu). \tag{2.34}$$

All the soft SUSY breaking parameters at the weak scale are then obtained through Renormalization Group Equations (RGE) [39].

The case of no mixing between the squarks correspond to the condition $A_u = \mu \cot\beta$ and $A_d = \mu \tan\beta$ in Eq. (2.26):

$$\begin{aligned} m^2_{\tilde{q}_L} &= m_0^2 + m_Z^2 \cos 2\beta \, (I_q - Q_q s_w^2) + m_q^2 \\ m^2_{\tilde{q}_R} &= m_0^2 + m_Z^2 \cos 2\beta \, (Q_q s_w^2) + m_q^2 \ . \end{aligned} \tag{2.35}$$

Otherwise, for $\tan\beta > 1$, after diagonalization we will have:

$$\begin{aligned} m^2_{\tilde{q}_{1,2}} &= m_0^2 + \frac{1}{2} m_Z^2 \cos(2\beta) \, I_q + m_q^2 \\ &\pm \left\{ \begin{array}{l} -\frac{1}{2}\Big[(m_Z^2 \cos 2\beta \, (I_u - 2Q_u s_w^2))^2 + 4 m_u^2 (A_u - \mu \cot\beta)^2 \Big]^{\frac{1}{2}} \\ \ \ \frac{1}{2}\Big[(m_Z^2 \cos 2\beta \, (I_d - 2Q_d s_w^2))^2 + 4 m_d^2 (A_d - \mu \tan\beta)^2 \Big]^{\frac{1}{2}} \end{array} \right. , \end{aligned} \tag{2.36}$$

where the upper and lower lines are for up-type and down-type squarks, respectively. If the parameters are real, we can obtain the mixing angle $\tilde{\theta}_q$ of the squarks for $\tan\beta > 1$ from the following equations:

$$\cos\theta_{\tilde{u},\tilde{d}} := \ S_{11}^{\tilde{u},\tilde{d}} \ = \ |m^2_{\tilde{q}_R} - m^2_{\tilde{q}_1}| \left\{ \begin{array}{l} \Big[m_u^2 (A_u - \mu\cot\beta)^2 + (m^2_{\tilde{u}_R} - m^2_{\tilde{u}_1})^2 \Big]^{-\frac{1}{2}} \\ \Big[m_d^2 (A_d - \mu\tan\beta)^2 + (m^2_{\tilde{d}_R} - m^2_{\tilde{d}_1})^2 \Big]^{-\frac{1}{2}} \end{array} \right. ,$$

$$\sin\theta_{\tilde{u},\tilde{d}} := \ S_{12}^{\tilde{u},\tilde{d}} \ = \ \left\{ \begin{array}{l} -\, m_u (A_u - \mu\cot\beta) \Big[m_u^2 (A_u - \mu\cot\beta)^2 + (m^2_{\tilde{u}_R} - m^2_{\tilde{u}_1})^2 \Big]^{-\frac{1}{2}} \\ +\, m_d (A_d - \mu\tan\beta) \Big[m_d^2 (A_d - \mu\tan\beta)^2 + (m^2_{\tilde{d}_R} - m^2_{\tilde{d}_1})^2 \Big]^{-\frac{1}{2}} \end{array} \right. \tag{2.37}$$

2.3.4 Gluinos

The gluino is a Majorana fermion and represents the superpartner of the gluon. There are eight gluinos corresponding to the eight linear independent $SU(3)_C$ generators. The gluinos represent already mass eigenstates, i.e. unlike the other superparticles they do not mix. They intract strongly and their mass is directly related to the soft SUSY breaking parameter M_3 ($M_3 \in \mathcal{R}$):

$$m_{\tilde{g}} \quad = \quad |M_3|. \tag{2.38}$$

The experimental constraints on the gluino mass are discussed in the next section.

2.3.5 Experimental limits

A lot of effort has been made in the last few years in the search for new physics. Unfortunately, no convincing signals of new particles have been found until now. However, through the accurate searches mainly at LEP and Tevatron, it has been possible to set some experimental limits on the masses of supersymmetrical particles and parameters. Mostly, the mSUGRA scenario has been used in the data analysis, even if some other scenarios, like the the GMSB scenario or R-parity violating (RPV) models, have been considered (for a review see [40]).

In the MSSM with conserved R-parity, the supersymmetrical particles always decay eventually to the LSP, which is conventionally assumed to be the lightest neutralino $\tilde{\chi}_1^0$. The latter is neutral, has no colour charge and interacts only weakly with matter. This means that it will almost certainly escape the detection. Therefore, in the search for supersymmetrical particles, one has to look for events with "missing energy".

At linear colliders the main signals come from SUSY particles with charge, weak isospin, or large Yukawa couplings. At LEP energies, one generally expects large cross sections for the gauge fermions (charginos and neutralinos), while the scalar particle cross sections are suppressed by kinematical factors near to threshold. Therefore, the signatures consist in some combination of jets, leptons, possibly photon, and missing energy.

At Tevatron, instead, the main source of signals for supersymmetry are squarks and gluinos. They can be produced in pairs in s, t and u-channel processes. One searches then for events with large missing transverse energy $\not{E}_T$. In Fig. 2.1, we show a typical exclusion plot, where the recent exclusion limits for the squark and gluino masses are given. One can see that the gluino has generally to be heavier than 300 GeV. Only if the squark mass is larger than 300 GeV, the lower limit for the gluino mass can be set to 195 GeV. In

Chapter 3, we will choose the lower limit for the gluino mass to be 300 GeV, as in our numerical analysis, we consider the region of the parameter space where $m_{\tilde{g}} \sim m_{\tilde{q}}$.

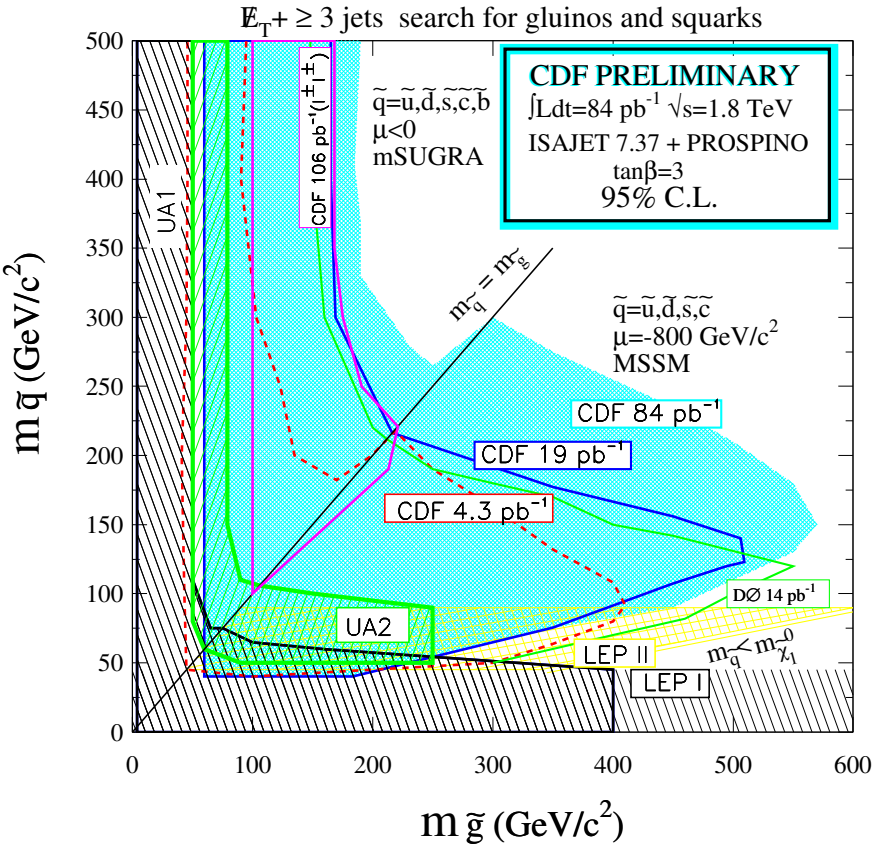

Figure 2.1: Regions in the $m_{\tilde{q}}$-$m_{\tilde{g}}$ excluded by CDF, DØ, and LEP.

Chapter 3

Single charged boson Higgs production

3.1 Introduction

In this chapter the calculation of the cross section for the process $e^+e^- \to t\overline{b}H^-$ and its charge conjugate (c.c) $e^+e^- \to \overline{t}bH^+$, including the order α_s QCD and SUSY QCD corrections, is described in detail. This reaction is kinematically allowed if $\sqrt{s} > m_t + m_b + m_H$. Hence, we are most interested in a situation where $m_t + m_b < \sqrt{s}/2 < m_H < \sqrt{s} - m_t - m_b$. For $\sqrt{s} = 500$ GeV (800 GeV), this implies that $250 \lesssim m_H \lesssim 320$ GeV ($400 \lesssim m_H \lesssim 620$ GeV). In such a situation, none of the virtual particles appearing in the tree-level diagrams can be resonating. We note in passing that the absence of resonances is also guaranteed if $m_t - m_b < m_H < m_t + m_b$ [19]. However, this process is then of minor interest because we always have $\sqrt{s} > 2m_H$, so that $e^+e^- \to H^+H^-$ will take place. In the presence of a resonance, the cross section approximately factorizes. Specifically, we have $\sigma(e^+e^- \to t\overline{b}H^-) \approx \sigma(e^+e^- \to t\overline{t})B(\overline{t} \to \overline{b}H^-)$ when the virtual top quark gets on its mass shell, while we have $\sigma(e^+e^- \to t\overline{b}H^-) \approx \sigma(e^+e^- \to H^+H^-)B(H^+ \to t\overline{b})$ when the virtual H^+ boson gets on its mass shell.

The outline of the chapter is the following: after discussing the general expression for the lepton tensor, we present in Sec. 3.3 the result for the Born cross section and a brief discussion about the three-particle phase-space. In Sec. 3.4, we describe the computation of the QCD corrections. To obtain the QCD corrections [22], we have to take into account the effect of virtual particles (virtual corrections) in loops as well as the emission of real gluons from the quarks (real corrections). The virtual corrections contain integrals which diverge because of large loop momenta (ultraviolet or UV divergence) or of very small loop

momenta (infrared or IR divergence).[1] We explain how to regularize the UV divergences and how to eliminate them with the help of the renormalization procedure. Regarding the IR divergences, the Bloch-Nordsieck [41] and the Kinoshita-Lee-Nauenberg (KLN) [42] theorems ensure that these divergences have to cancel in the incoherent sum over all the indistinguishable final states. Therefore, we considered the process $e^+e^- \to t\bar{b}gH^-$ (and its c.c. $e^+e^- \to \bar{t}bgH^+$) and checked analytically the cancellation of the IR divergences. In Sec. 3.5, we discuss some technical details of the calculation of the SUSY QCD corrections. and in Sec. 3.6 we present our numerical results.

3.2 Lepton tensor

Let us consider a general process with e^+e^- in the initial state where n particles are produced via a virtual photon or a Z boson exchange in the s-channel.
The four-momenta of the incoming electron and positron are called k_1 and k_2 and those of the outgoing particles $p_i (i = 1, \ldots, n)$, respectively. Assuming that the outgoing particles are much heavier than the electron, we can neglect the electron mass, so that the on-mass-shell (OS) conditions read $k_1^2 = k_2^2 = 0$ and $p_i^2 = m_i^2$. The virtual photon and Z boson have four-momentum $p = k_1 + k_2 = \sum_{i=1}^n p_i$, and we define $s = p^2$. Here and in the following, we define the Lorentz-invariant n-particle phase-space measure as

$$d\mathrm{PS}_n(p; p_1, \ldots, p_n) = (2\pi)^4 \delta^{(4)} \left(p - \sum_{i=1}^n p_i \right) \prod_{i=1}^n \frac{d^3 p_i}{(2\pi)^3 2p_i^0}. \tag{3.1}$$

We assume that the incoming leptons are unpolarized and the expression for the differential cross section is given by

$$d\sigma = \frac{1}{2s} \frac{1}{4} |\mathcal{T}|^2 d\mathrm{PS}_n(p; p_1, \ldots, p_n), \tag{3.2}$$

where $\mathcal{T}$ is the transition-matrix element corresponding to the considered process , $1/(2s)$ is the flux factor and the average over the lepton spins gives rise to the factor $1/4$. Next, we observe that $|\mathcal{T}|^2$ can be written as a contraction of two rank-two tensors, a leptonic one involving k_1 and k_2 and a hadronic one involving $p_1, \ldots, p_n$. The hadronic tensor carries all the information about the particular process under consideration, while the lepton tensor is common to every s-channel process with e^+e^- in the initial state and with a virtual photon or Z boson exchange. The latter has the general form

$$L^{\mu\nu} = \mathrm{tr}\left[\not{k}_1 \gamma^\nu \left(v_e' - a_e' \gamma_5\right) \not{k}_2 \gamma^\mu (v_e - a_e \gamma_5) \right], \tag{3.3}$$

[1] As in this process all the final state particles are massive, we do not have to deal with collinear IR divergences.

where v_e, v'_e, a_e, and a'_e are generic vector and axial-vector couplings of the electron to the photon or Z boson. To obtain this expression we have used the relations[2]

$$\sum_{\lambda_1=\pm1} u(k_1,\lambda_1)\bar{u}(k_1,\lambda_1) = \not{k}_1, \qquad \sum_{\lambda_2=\pm1} v(k_2,\lambda_2)\bar{v}(k_2,\lambda_2) = \not{k}_2, \tag{3.5}$$

where u, λ_1 and v, λ_2 are the spinors and helicities of the electron and positron, respectively. We indicate here with $\lambda_{1,2} = +1$ ($\lambda_{1,2} = -1$) the states with positive (negative) helicity, i.e. with spin parallel (anti-parallel) to the direction of motion. After evaluating the trace one obtains

$$L^{\mu\nu} = 4\Big[\left(v_e v'_e + a_e a'_e\right) \{k_1 k_2\}^{\mu\nu} - i \left(v_e a'_e + a_e v'_e\right) \epsilon^{\mu\nu\alpha\beta} k_{1\alpha} k_{2\beta}\Big], \tag{3.6}$$

with

$$\{k_1 k_2\}^{\mu\nu} = k_1^\mu k_2^\nu + k_1^\nu k_2^\mu - k_1 \cdot k_2 g^{\mu\nu}. \tag{3.7}$$

For Lorentz invariance, we can write the integral of $L^{\mu\nu}_{\rm pol}$ as a linear combination of $g^{\mu\nu}$ and the momenta $p^\mu p^\nu$ as follows

$$\int \frac{d\Omega}{4\pi} L^{\mu\nu}_{\rm pol} = A g^{\mu\nu} + B p^\mu p^\nu. \tag{3.8}$$

Contracting the last expression with $g^{\mu\nu}$ and $p^\mu p^\nu$, respectively, one finds the solution for the coefficients A and B, and the lepton tensor is given by

$$\int \frac{d\Omega}{4\pi} L^{\mu\nu} = \frac{4}{3}\left(v_e v'_e + a_e a'_e\right)\left(p^\mu p^\nu - s g^{\mu\nu}\right). \tag{3.9}$$

The fact that Eq. (3.9) just depends on p, dramatically simplifies the remaining phase-space integrations, and the role of the lepton tensor is reduced to that of a prefactor. Therefore, we can restrict ourselves to the study of the *decay* of a virtual photon or Z boson instead of studying a *scattering* process with two incoming particles. In the first case (*decay*), the number of variables $\boldsymbol{p}_1, \ldots, \boldsymbol{p}_n$ constrained by four momentum conservation is $3n-4$. However, absence of spin for the final states implies that in the rest frame of the decaying particle the orientation of the momentum configuration is irrelevant. This means that three variables are trivial and we are left with $3n-7$ *essential variables* [43]. In the second case (*scattering*) there are $3n-4$ final state variables as well but this time the beam axis defines a direction in space and there is just one trivial variable ϕ, corresponding to

[2]The general expressions for massive particles are

$$\sum_{\lambda=\pm1} u(k,\lambda)\bar{u}(k,\lambda) = \not{k} + m, \qquad \sum_{\lambda=\pm1} v(k,\lambda)\bar{v}(k,\lambda) = \not{k} - m. \tag{3.4}$$

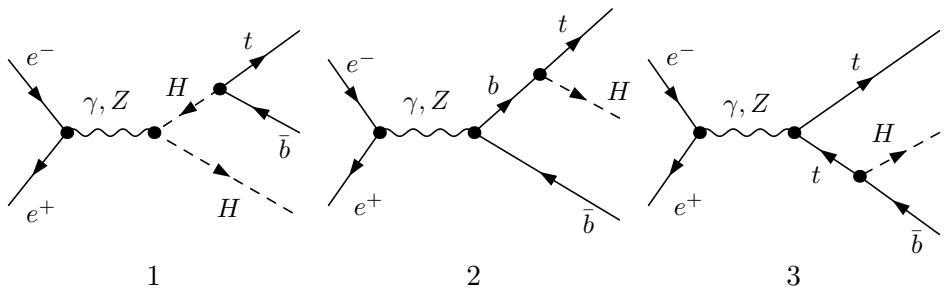

Figure 3.1: Tree-level Feynman diagrams pertinent to the process $e^+e^- \to t\bar{b}H^-$.

the rotation around the beam axis. We are left then with $3n-5$ essential final state variables. In other words, this property of the lepton tensor allows us to reduce by two the number of integrations (from 4 to 2 and from 7 to 5 in the case of three particles and four particles in the final state, respectively).

3.3 Born cross section

We start by defining the kinematics. We call the four-momenta of the incoming electron and positron k_1 and k_2 and those of the outgoing t quark, $\overline{b}$ quark, and H^- boson p_1, p_2, and p_3, respectively. We neglect the electron mass, but retain the b-quark mass, so that the OS conditions read $k_1^2 = k_2^2 = 0$, $p_1^2 = m_t^2$, $p_2^2 = m_b^2$, and $p_3^2 = m_H^2$. As before, the virtual photon and Z boson have four-momentum $p = k_1 + k_2 = p_1 + p_2 + p_3$, and we define $s = p^2$. It is convenient to introduce the dimensionless Lorentz scalars

$$a_i = \frac{p_i^2}{s}, \qquad x_i = \frac{2p \cdot p_i}{s}, \qquad y_i = \sqrt{x_i^2 - 4a_i}, \tag{3.10}$$

with $i = 1, 2, 3$. In the c.m. frame, $x_i = 2p_i^0/\sqrt{s}$ and $y_i = 2|\boldsymbol{p_i}|/\sqrt{s}$ carry the meaning of scaled energies and absolute three-momenta, respectively. By four-momentum conservation, we have $x_1 + x_2 + x_3 = 2$.

The differential Born cross section may be evaluated as

$$d\sigma_{\text{Born}} = \frac{1}{2s}\frac{1}{4}|\mathcal{T}_{\text{Born}}|^2 d\text{PS}_3(p; p_1, p_2, p_3), \tag{3.11}$$

where $\mathcal{T}_{\text{Born}}$ is the transition-matrix element corresponding to the Feynman diagrams of Fig. 3.1, and the summation over the lepton and quark spins is implied. We assume that the incoming leptons are unpolarized.

We now discuss the parameterization of the three-particle phase space. We wish to express the Born cross section differential with respect to the scaled energies of the final-state quarks, x_1 and x_2. For convenience, we work in the c.m. frame, define the z axis of the coordinate system to point along $\boldsymbol{k}_1 = -\boldsymbol{k}_2$, and fix the x axis in an arbitrary way. We then have

$$d\mathrm{PS}_3(p; p_1, p_2, p_3) = \frac{4}{(4\pi)^5} dp_1^0\, d\cos\theta_1\, d\phi_1\, dp_2^0\, d\phi_2, \tag{3.12}$$

where θ_1 and ϕ_1 are the polar and azimuthal angles of $\boldsymbol{p}_1$, respectively, and ϕ_2 is the azimuthal angle of $\boldsymbol{p}_2$ with respect to the axis pointing along $\boldsymbol{p}_1$ measured from the plane spanned by $\boldsymbol{k}_1$ and $\boldsymbol{p}_1$. Due to the azimuthal symmetry of the problem at hand, the integration over ϕ_1 is trivial, and we may take $\boldsymbol{p}_1$ to lie in the x-z plane. If we now rotate the coordinate system in such a way that $\boldsymbol{p}_1$ points along the z axis and $\boldsymbol{p}_2$ lies in the x-z plane, then $\theta = \theta_1$ and $\phi = \pi - \phi_2$ define the direction of $\boldsymbol{k}_1$. We thus have

$$d\mathrm{PS}_3(p; p_1, p_2, p_3) = \frac{s}{2(4\pi)^4} dx_1\, dx_2\, d\cos\theta\, d\phi. \tag{3.13}$$

We have seen in Sec. 3.2 that after the integration over θ and ϕ the scalar products of the type $k_i \cdot p_j$ are precluded. The residual scalar products can be written as follows

$$p_i \cdot p_j = \frac{s}{2}(z_k - a_i - a_j), \tag{3.14}$$

where

$$z_k = 1 + a_k - x_k, \tag{3.15}$$

with $i, j, k = 1, 2, 3$ and $i \neq j \neq k \neq i$. The doubly-differential Born cross section in terms of our dimensionless variables x_1 and x_2 is given by:

$$\frac{d\sigma_{\mathrm{Born}}}{dx_1\, dx_2} = \frac{G_F^3 m_Z^4}{32\pi^3\sqrt{2}} \left[\mathcal{Q}_e^2 f_{\gamma\gamma}(x_1, x_2) + \mathcal{Q}_e \mathcal{V}_e f_{\gamma Z}(x_1, x_2) + \left(\mathcal{V}_e^2 + \mathcal{A}_e^2\right) f_{ZZ}(x_1, x_2)\right], \tag{3.16}$$

where G_F is Fermi's constant,

$$\mathcal{Q}_e = -2 c_w s_w Q_e, \qquad \mathcal{V}_e = \frac{I_e - 2 s_w^2 Q_e}{1 - m_Z^2/s}, \qquad \mathcal{A}_e = \frac{I_e}{1 - m_Z^2/s}, \tag{3.17}$$

and $f_{\gamma\gamma}(x_1, x_2)$, $f_{\gamma Z}(x_1, x_2)$, and $f_{ZZ}(x_1, x_2)$ are form factors listed in Appendix B. Here, $Q_e = -1$ is the electric charge of the electron, and $I_e = -1/2$ is the third component of weak isospin of its left-handed component.

The boundaries of integration are

$$\begin{aligned} 2\sqrt{a_1} \;&<\; x_1 \;<\; 1 + a_1 - \left(\sqrt{a_2} + \sqrt{a_3}\right)^2, \\ x_2^- \;&<\; x_2 \;<\; x_2^+, \end{aligned} \tag{3.18}$$

with

$$x_2^{\pm} = \frac{1}{2z_1}\left[(2-x_1)(z_1+a_2-a_3) \pm y_1\sqrt{\lambda(z_1,a_2,a_3)}\right], \tag{3.19}$$

where

$$\lambda(x,y,z) = x^2+y^2+z^2-2(xy+yz+zx) \tag{3.20}$$

is the Källén's function. We perform the integrations over x_1 and x_2 numerically with the aid of the multi-dimensional Monte Carlo integration routine `VEGAS` [44].

3.4 QCD corrections

3.4.1 Virtual corrections

Let us now turn to the virtual QCD corrections, which arise from the one-loop Feynman diagrams shown in Fig. 3.2. Specifically, they include t- and b-quark self-energy corrections; $t\bar{t}\gamma$, $t\bar{t}Z$, $b\bar{b}\gamma$, $b\bar{b}Z$, and $t\bar{b}H^-$ vertex corrections; and $t\bar{b}\gamma H^-$ and $t\bar{b}ZH^-$ box corrections. These corrections suffer both from IR and UV divergences. We regularize the former by endowing the gluon with an infinitesimal mass, m_g. In our case, this does not spoil gauge invariance, since the non-abelian nature of QCD does not yet emerge at next-to-leading order. This leads to terms logarithmic in m_g, which combine with similar terms arising from soft-gluon emission, to be discussed below, to give an m_g-independent result.

UV divergences only occur in the self-energy and vertex corrections. We extract them using dimensional regularization (DReg) [45], with $D = 4-2\epsilon$ space-time dimensions and 't Hooft mass scale μ. They are removed by renormalization. Specifically, we need to renormalize the quark masses and wave functions appearing in $\mathcal{T}_{\rm Born}$. Notice that the quark masses enter not only through the quark propagators, but also through the $t\bar{b}H^-$ coupling. To distinguish them, we will call the mass term in the propagators $m_q^{\rm prop}$ and the one in the Yukawa coupling $m_q^{\rm Yuk}$. We need to substitute in the Lagrangian the bare quark masses $m_q^{0,\rm Yuk}$, $m_q^{0,\rm prop}$, and the bare quark field ψ_q^0 ($q=t,b$) through their renormalized expressions. The relations between the bare and the renormalized parameters read[3]:

$$\begin{aligned} m_q^{0,\rm prop} &= m_q^{\rm prop} + \delta m_q^{\rm prop}, \\ m_q^{0,\rm Yuk} &= m_q^{\rm Yuk} + \delta m_q^{\rm Yuk}, \\ \psi_q^{0,L} &= \psi_q^L\sqrt{\delta Z_q^L} = \psi_q^L\left(1+\frac{1}{2}\delta Z_q^L\right), \end{aligned}$$

[3]We have omitted everywhere the generation indices because only the third generation of quarks plays a role in this calculation.

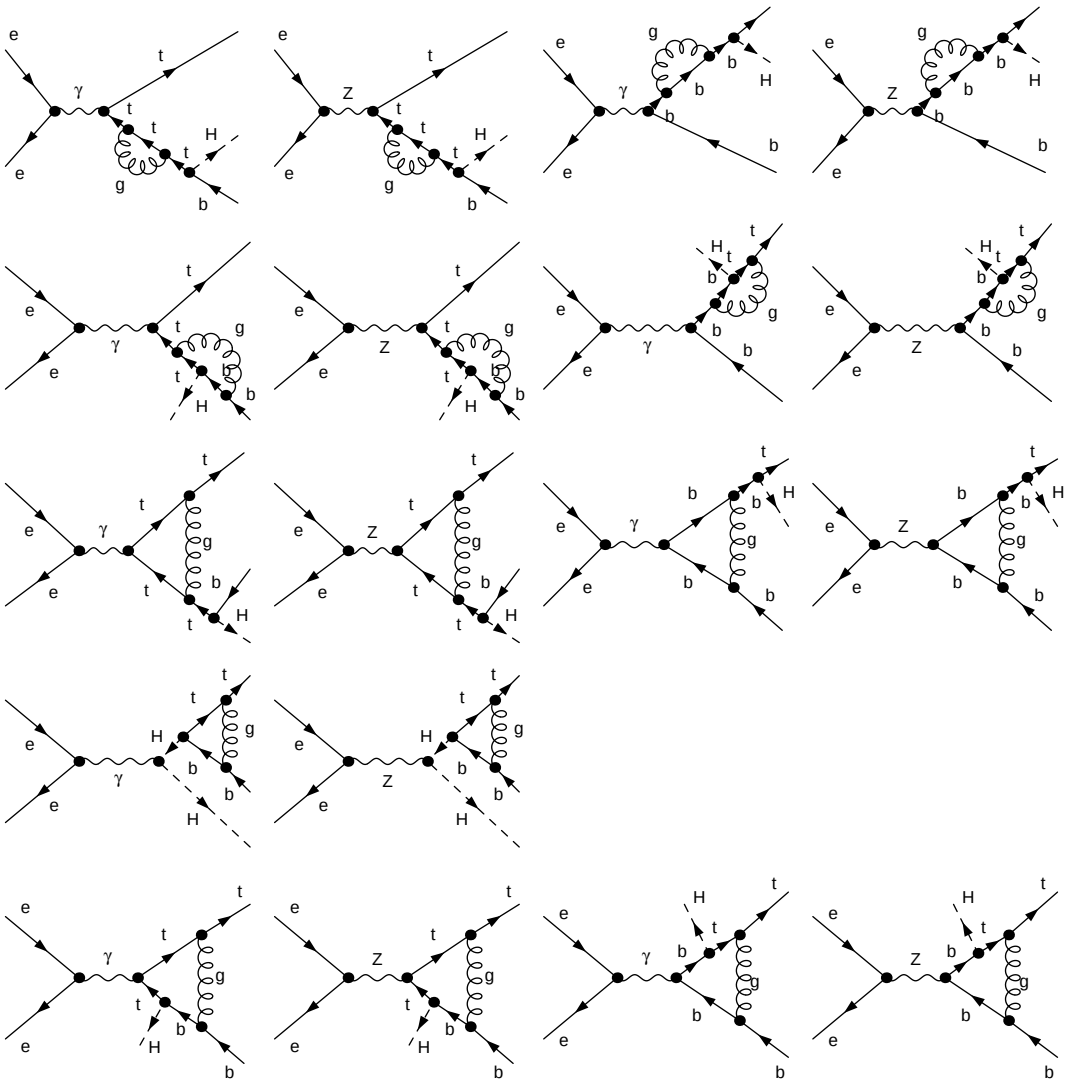

Figure 3.2: One-loop Feynman diagrams pertinent to the process $e^+e^- \to t\bar{b}H^-$. They are classified according to the number of propagators in the loop.

$$\psi_q^{0,R} \;=\; \psi_q^R\sqrt{\delta Z_q^R} = \psi_q^R\left(1+\frac{1}{2}\delta Z_q^R\right), \tag{3.21}$$

where $\psi_q^L = P_L\psi_q$ and $\psi_q^R = P_R\psi_q$ represent the left-handed and right-handed components of ψ, obtained multiplying by the the chirality projectors $P_{L,R} = \frac{1}{2}(1 \mp \gamma_5)$. To determine the counterterms $\delta m_q^{\text{prop,Yuk}}$ and $\delta Z_q^{L,R}$, one has to impose the renormalization conditions. We will work in a mixed renormalization scheme, which we call "Yukawa mixed scheme". In this scheme, the counterterm for the Yukawa coupling mass is computed in the minimal subtraction ($\overline{\text{MS}}$) scheme [46], while the other counterterms are defined in the on-mass-

shell scheme (OS) [47]. As we will discuss in detail in Sec. 3.6.1, in the Yukawa mixed scheme, the results do not contain large logarithms in m_b which instead arise if we renormalize the mass in the Yukawa coupling in the OS scheme [22]. In the OS scheme, the renormalized masses are assumed to be equal to the physical masses, i.e. to the real part of the poles of the respective propagators. For the fields, it is required that the residues of the renormalized propagators are equal to 1. In the momentum space, the renormalized amputated one-particle irreducible (1PI) two-point Green function $\hat{\Gamma}^{(2)}(k)$ and the respective propagator $\hat{G}^{(2)}(k)$, with the external momentum k, satisfy the relation:

$$\hat{\Gamma}^{(2)}(k)\hat{G}^{(2)}(k) = i. \tag{3.22}$$

Therefore, the renormalization conditions can be expressed in terms of the 1PI two-point function, as the poles of the propagator are equivalent to the zeros of the 1PI two-point function. For the quarks, the latter is defined by:

$$\hat{\Gamma}_q(p) = i(\not{p} - m_q) + i\left[\not{p}P_L\hat{\Sigma}_q^L(p^2) + \not{p}P_R\hat{\Sigma}_q^R(p^2) + P_L\hat{\Sigma}_q^D(p^2) + P_R\hat{\Sigma}_q^{D*}(p^2)\right], \tag{3.23}$$

where we have decomposed the renormalized quark self-energy $\hat{\Sigma}_q$ in its most general form [48]. Let us now introduce the spinors u and $\bar{u}$ which are solutions of the Dirac equation with mass m_q:

$$(\not{p} - m_q)u(p) = 0, \qquad \bar{u}(p')(\not{p}' - m_q) = 0. \tag{3.24}$$

The renormalization conditions read[4]:

$$\begin{aligned}
\tilde{\mathrm{Re}}\hat{\Gamma}_q(p)u(p)|_{p^2=m_q^2} &= 0 \\
\bar{u}(p')\tilde{\mathrm{Re}}\hat{\Gamma}_q(p')|_{p'^2=m_q^2} &= 0, \\
\lim_{p^2\to m_q^2}\frac{\not{p}+m_q}{p^2-m_q^2}\tilde{\mathrm{Re}}\hat{\Gamma}_q(p)u(p) &= iu(p), \\
\lim_{p'^2\to m_q^2}\bar{u}(p')\tilde{\mathrm{Re}}\hat{\Gamma}_q(p')\frac{\not{p}'+m_q}{p'^2-m_q^2} &= i\bar{u}(p').
\end{aligned} \tag{3.25}$$

Eventually, following [48] we obtain the counterterms as functions of the unrenormalized self-energies:

$$\begin{aligned}
\delta m_q &= \frac{1}{2}m_q\tilde{\mathrm{Re}}\left[\Sigma_q^L(m_q^2) + \Sigma_q^R(m_q^2)\right] + \frac{1}{2}\tilde{\mathrm{Re}}\left[\Sigma_q^D(m_q^2) + \Sigma_q^{D*}(m_q^2)\right] \\
\delta Z_q^L &= -\tilde{\mathrm{Re}}\Sigma_q^L(m_q^2) - m_q^2\tilde{\mathrm{Re}}\left[\Sigma_q^{L\prime}(m_q^2) + \Sigma_q^{R\prime}(m_q^2)\right]
\end{aligned}$$

[4] $\tilde{\mathrm{Re}}$ is the real part of the one-loop integrals which occur in the self-energies. However, the mixing matrix elements are still complex.

$$
\begin{aligned}
& +\tilde{\mathrm{Re}}\left[\Sigma_q^{D\prime}(m_q^2)+\Sigma_q^{D*\prime}(m_q^2)\right], \\
\delta Z_q^R &= -\tilde{\mathrm{Re}}\Sigma_q^R(m_q^2) - m_q^2\tilde{\mathrm{Re}}\left[\Sigma_q^{L\prime}(m_q^2)+\Sigma_q^{R\prime}(m_q^2)\right] \\
& +\tilde{\mathrm{Re}}\left[\Sigma_q^{D\prime}(m_q^2)+\Sigma_q^{D*\prime}(m_q^2)\right],
\end{aligned} \tag{3.26}
$$

where δm_q represents the expression of the mass counterterm in the OS scheme and

$$
\Sigma'(m_q^2) = \left(\frac{\partial\Sigma(p^2)}{\partial p^2}\right)\Big|_{p^2=m_q^2}.
$$

The expression for the quark self-energy is given in Appendix D.
In the case of QCD corrections, we have that $\delta Z_q^L = \delta Z_q^R = \delta Z_q$ and the counterterms assume the simple form:

$$
\begin{aligned}
\delta m_q &= -\frac{\alpha_s}{4\pi}C_F m_q\left[3\Delta + 3\ln\frac{\mu^2}{m_q^2} + 4 + \mathcal{O}(\epsilon)\right], \\
\delta Z_q &= -\frac{\alpha_s}{4\pi}C_F\left[\Delta + \ln\frac{\mu^2}{m_q^2} + 2\ln\frac{m_g^2}{m_q^2} + 4 + \mathcal{O}(\epsilon)\right],
\end{aligned} \tag{3.27}
$$

with $C_F = (N_c^2-1)/(2N_c) = 4/3$ for $N_c = 3$ quark colors and

$$
\Delta = \frac{1}{\epsilon} - \gamma_E + \ln(4\pi), \tag{3.28}
$$

where γ_E is the Euler-Mascheroni constant.

On the other hand, in the $\overline{\mathrm{MS}}$ scheme, the counterterms contain only the divergences. In particular, the $\overline{\mathrm{MS}}$ counterterm for the quark mass reads:

$$
\delta\overline{m}_q = -\frac{3\alpha_s}{4\pi}C_F m_q\Delta. \tag{3.29}
$$

It is interesting to note that δZ_q is also IR divergent.
Eventually, the virtual QCD corrections may be evaluated as

$$
d\sigma_{\mathrm{virt}} = d\sigma_{\mathrm{Born}}\delta_{\mathrm{virt}}(m_g), \tag{3.30}
$$

with

$$
\begin{aligned}
\delta_{\mathrm{virt}}(m_g) = \frac{2}{|\mathcal{T}_{\mathrm{Born}}|^2}\,\mathrm{Re}\Bigg\{\mathcal{T}_{\mathrm{Born}}^*\Bigg[\sum_{q=t,b}\Bigg(&\delta m_q^{\mathrm{Yuk}}\frac{\partial}{\partial m_q^{\mathrm{Yuk}}} \\
&+\delta m_q^{\mathrm{prop}}\frac{\partial}{\partial m_q^{\mathrm{prop}}} + \frac{1}{2}\delta Z_q\Bigg)\mathcal{T}_{\mathrm{Born}} + \mathcal{T}_{\mathrm{loop}}\Bigg]\Bigg\},
\end{aligned} \tag{3.31}
$$

where $\mathcal{T}_{\mathrm{loop}}$ is the transition-matrix element corresponding to the Feynman diagrams of Fig 3.2. Notice that the quark masses that appear in the squares of the quark spinors

and in the boundaries of the phase-space integration correspond to OS renormalized ones from the outset. As mentioned above, $\delta_{\rm virt}(m_g)$ is UV finite, but IR divergent. Notice that Eq. (3.3), which refers to the physical case $D = 4$, can still be used at the one-loop level, since the quarkonic tensor is by itself UV finite upon renormalization.

We generate $\mathcal{T}_{\rm loop}$ and reduce it to standard one-loop scalar integrals defined in Appendix A using the combination of the program packages `FeynArts` [49] and `FormCalc` [50]. The results have been compared numerically with another totally independent computation performed with the help of custom-made routines written in the program language `FORM` [51]. We then evaluate the standard one-loop scalar integrals, the IR-divergent ones analytically using the results of Ref. [52] and the IR-finite ones numerically with the help of the program package `LoopTools` [50]. Our analytic result for $\delta_{\rm virt}(m_g)$ is too lengthy to be presented here.

3.4.2 Real corrections

We now proceed to the real QCD corrections, which arise from the $2 \to 4$ tree-level Feynman diagrams shown in Fig. 3.3. We denote the gluon four-momentum by q. As mentioned above, the emission of soft gluons generates IR divergences. For consistency with the evaluation of the virtual QCD corrections, the latter must also be regularized by the gluon mass m_g. It is convenient to work in the c.m. frame and to introduce an unphysical gluon-energy cutoff, $E_{\rm cut}$, with $m_g \ll E_{\rm cut} \ll E_{\rm max}$, where $E_{\rm max}$ is the maximum gluon energy allowed by kinematics, so as to separate the gluon phase space into soft and hard regions, defined by $m_g < q^0 < E_{\rm cut}$ and $E_{\rm cut} < q^0 < E_{\rm max}$, respectively. This has two technical advantages, since soft gluons with infinitesimal mass m_g do not affect the kinematics of the underlying process, while hard gluons with zero mass do not produce IR divergences. On the one hand, the soft-gluon bremsstrahlung may be treated analytically in the eikonal approximation, which is independent of the underlying process and results in a multiplicative correction to the Born result. On the other hand, m_g may be safely neglected in the treatment of the hard-gluon bremsstrahlung, which facilitates the phase-space integration. In turn, the soft- and hard-gluon contributions both depend on $E_{\rm cut}$, while their combined contribution is, of course, independent of $E_{\rm cut}$, which we checked numerically. In Fig. 3.4 we have plotted the dependence on $E_{\rm cut}$ of the different contributions to the next-to-leading order (NLO) cross section. For our numerical evaluation we have chosen $E_{\rm cut} = 0.8$ GeV, because on the one hand, one can see in Fig. 3.4 that for this value the NLO curve is quite flat. On the other hand, this value lies far from the region where soft- and hard-gluon corrections depend strongly on

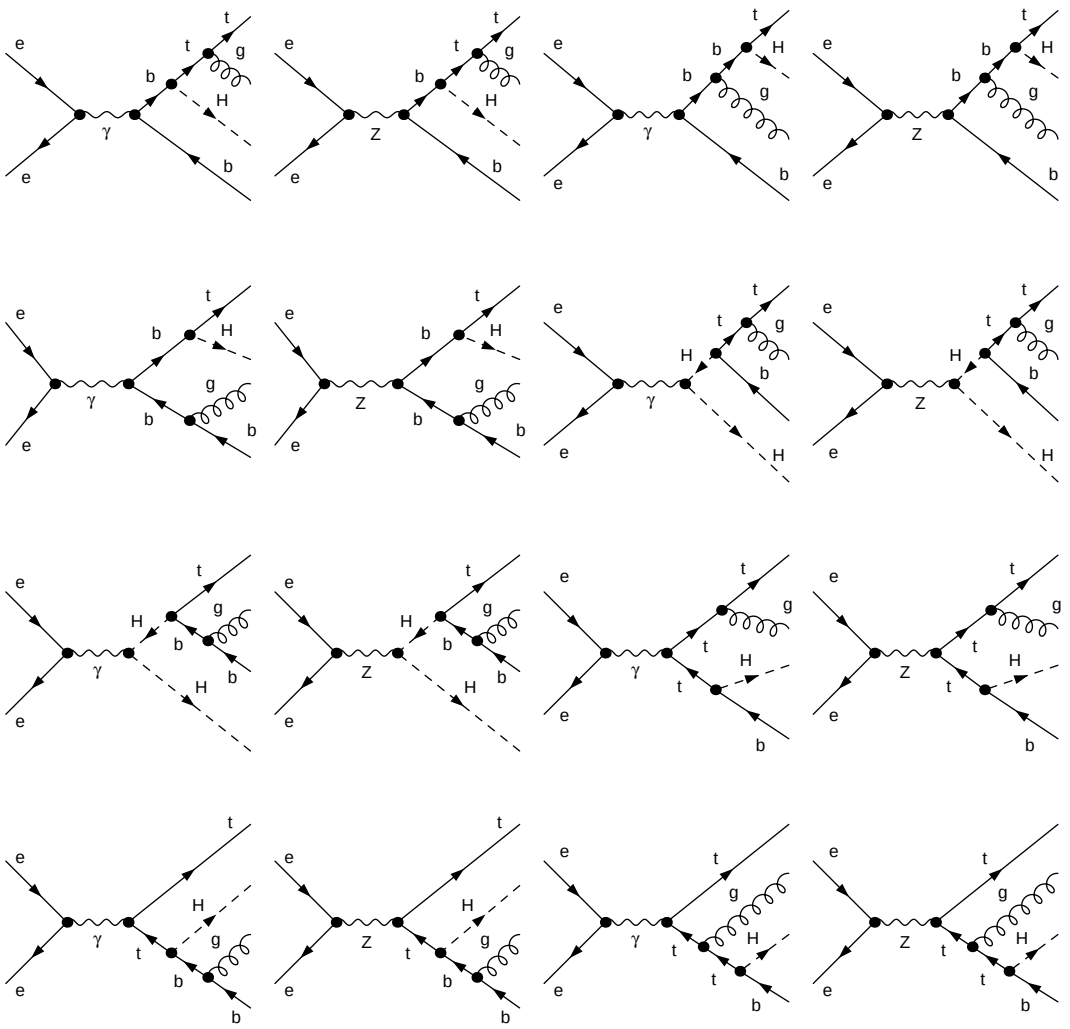

Figure 3.3: Tree-level Feynman diagrams pertinent to the process $e^+e^- \to t\bar{b}gH^-$.

$E_{\rm cut}$.

The soft-gluon contribution is given by

$$d\sigma_{\rm soft} = d\sigma_{\rm Born}\delta_{\rm soft}(m_g, E_{\rm cut}), \tag{3.32}$$

with

$$\delta_{\rm soft}(m_g, E_{\rm cut}) = -\frac{\alpha_s C_F}{(2\pi)^2}\int_{|\boldsymbol{q}|<E_{\rm cut}} \frac{d^3q}{q^0}\left(\frac{p_1}{p_1\cdot q} - \frac{p_2}{p_2\cdot q}\right)^2, \tag{3.33}$$

where $q^0 = \sqrt{\boldsymbol{q}^2 + m_g^2}$ is the gluon energy. The integration in Eq. (3.33) can be performed analytically as described in Ref. [53, 54], the result being

$$\delta_{\rm soft}(m_g, E_{\rm cut}) = \frac{\alpha_s}{\pi}C_F\left\{\left(\frac{\alpha}{2}\,\frac{z_3 - a_1 - a_2}{\alpha^2 a_1 - a_2}\ln\frac{\alpha^2 a_1}{a_2} - 1\right)\ln\frac{4E_{\rm cut}^2}{m_g^2}\right.$$

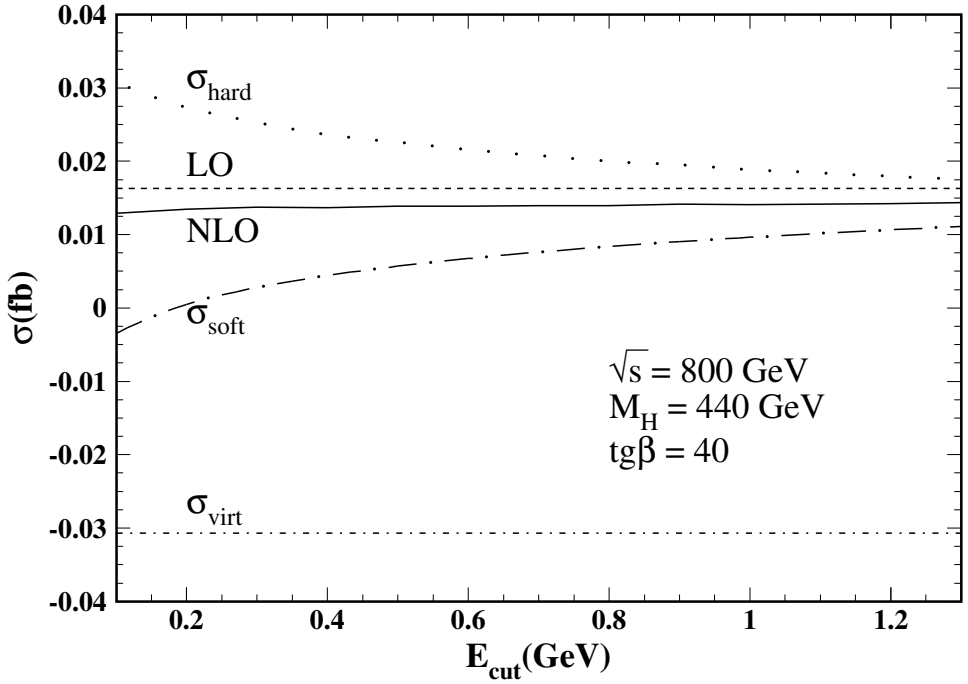

Figure 3.4: Different contributions to the total cross section of $e^+e^- \to t\bar{b}gH^-, \bar{t}bgH^+$ as a function of the gluon-energy cut-off, $E_{\rm cut}$, for $\sqrt{s} = 800$ GeV, $\tan\beta = 40$, $m_H = 440$ GeV.

$$
\begin{aligned}
&+ \alpha\frac{z_3 - a_1 - a_2}{\alpha^2 a_1 - a_2}\left[\mathrm{Li}_2\left(1 - \alpha\frac{x_1 + y_1}{v}\right) + \mathrm{Li}_2\left(1 - \alpha\frac{x_1 - y_1}{v}\right)\right. \\
&- \mathrm{Li}_2\left(1 - \frac{x_2 + y_2}{v}\right) - \mathrm{Li}_2\left(1 - \frac{x_2 - y_2}{v}\right) + \frac{1}{4}\left(\ln^2\frac{x_1 - y_1}{x_1 + y_1} - \ln^2\frac{x_2 - y_2}{x_2 + y_2}\right)\Bigg] \\
&\left. - \frac{1}{2}\left(\frac{x_1}{y_1}\ln\frac{x_1 - y_1}{x_1 + y_1} + \frac{x_2}{y_2}\ln\frac{x_2 - y_2}{x_2 + y_2}\right)\right\}, \qquad (3.34)
\end{aligned}
$$

where

$$
\mathrm{Li}_2(x) = -\int_0^x dy\,\frac{\ln(1-y)}{y} \qquad (3.35)
$$

is the Spence function, and

$$
\begin{aligned}
\alpha &= \frac{1}{2a_1}\left[z_3 - a_1 - a_2 + \sqrt{\lambda(z_3, a_1, a_2)}\right], \\
v &= 2\frac{\alpha^2 a_1 - a_2}{\alpha x_1 - x_2}. \qquad (3.36)
\end{aligned}
$$

Notice that Eq. (3.34) like Eq. (3.33) is invariant under the interchange of the indices 1 and 2.

The hard-gluon contribution may be evaluated by integrating

$$d\sigma_{\rm hard}(E_{\rm cut}) = \frac{1}{2s}\,\frac{1}{4}|\mathcal{T}_{\rm real}|^2\theta(q^0 - E_{\rm cut})d{\rm PS}_4(p; p_1, p_2, p_3, q), \tag{3.37}$$

where $\mathcal{T}_{\rm real}$ is the transition-matrix element corresponding to the Feynman diagrams of Fig. 3.3, over the full four-particle phase space, imposing the condition $q^0 > E_{\rm cut}$. We use the parameterization of the four-particle phase space presented in Appendix C. It involves five nontrivial integrations, which we perform numerically using the Monte Carlo routine `VEGAS` [44]. Our formula for $|\mathcal{T}_{\rm real}|^2$ is too lengthy to be listed here.

We performed several checks for our implementation of the four-particle phase-space integration. We numerically verified the analytical formula for the total cross section of $e^+e^- \to q\overline{q}g^* \to q\overline{q}Q\overline{Q}$, where q and Q represent massless and massive quarks, respectively, and g^* denotes a virtual gluon, given in Eq. (2) of Ref. [55]. In this case, IR singularities do not appear in intermediate steps, so that no separation into soft-gluon and hard-gluon contributions is required. We also found excellent agreement with a numerical result for a similar process involving four different quark masses obtained using the democratic multi-particle phase-space generator `RAMBO` [56].

Our final result for the QCD-corrected differential cross section reads

$$d\sigma_{\rm QCD} = d\sigma_{\rm Born}[1 + \delta_{\rm virt}(m_g) + \delta_{\rm soft}(m_g, E_{\rm cut})] + d\sigma_{\rm hard}(E_{\rm cut}), \tag{3.38}$$

where $d\sigma_{\rm Born}$, $\delta_{\rm virt}(m_g)$, $\delta_{\rm soft}(m_g, E_{\rm cut})$, and $d\sigma_{\rm hard}(E_{\rm cut})$ are defined in Eqs. (3.11), (3.31), (3.33), and (3.37), respectively. It is manifestly independent of m_g and insensitive to the choice of $E_{\rm cut}$, as long as $m_g \ll E_{\rm cut} \ll E_{\rm max}$, as we verified numerically.

The QCD-corrected cross section of the SM process $e^+e^- \to t\bar{t}H$ via a virtual photon can be obtained from our results as a special case, involving only a subclass of the Feynman diagrams shown in Figs. 3.1–3.3. As a by-product of our analysis, we confirmed the numerical results for this cross section obtained in Refs. [23, 24] and the description of this computation together with updated numerical results is contained in Chapter 4. In turn, this provides a nontrivial check for all parts of our analysis.

3.4.3 Extraction of the IR divergences

In Sec. 3.4.1, we mentioned that both the virtual and the soft corrections contain IR divergences, i.e. logarithms in m_g and that these have to cancel in the combination of the single contributions $\delta_{\rm soft}$ and $\delta_{\rm virt}$. In order to obtain this cancellation one has to express all the divergent functions arising in the soft and virtual corrections, respectively, in terms of the same variables. We have already seen in Eq. (3.34) the structure of the divergences

in $\delta_{\rm soft}$ in terms of the dimensionless Lorentz scalars defined in Eq. (3.10). As far as the virtual corrections are concerned, one has first to observe that only the $t\bar{b}H^-$vertex corrections in the diagrams with a virtual Higgs exchange and the $t\bar{b}\gamma H^-$ and $t\bar{b}ZH^-$ box corrections are IR divergent. After the reduction of the tensor coefficient functions has been performed, in the $t\bar{b}H^-$ vertex corrections we have the IR divergent scalar three-point function $C_0(p_1^2, p_2^2, (p_1+p_2)^2, m_t^2, 0, m_b^2)$. The explicit expression of this function can be found in Appendix A, where we followed Ref. [52]. Here we are just interested in its divergent part, that can be written in terms of dimensionless Lorentz scalars as follows:

$$C_0^{\rm IR} = \ln(m_g^2)\left[\frac{1}{s\sqrt{\lambda(z_3,a_1,a_2)}}\ln\left(\frac{z_3-a_1-a_2-\sqrt{\lambda(z_3,a_1,a_2)}}{2\sqrt{a_1a_2}}\right)\right]. \tag{3.39}$$

In the box contribution there are two IR divergent scalar four-point functions D_0, whose general solution is listed in Appendix A. We indicate by $D_0^{1,\rm IR}$ the divergent part of the four-point function $D_0(p_1^2, p_2^2, p_3^2, p^2, (p_1+p_2)^2, (p_2+p_3)^2, m_t^2, 0, m_b^2, m_t^2)$, which corresponds to the box diagrams with two top quark propagators. On the other hand, $D_0^{2,\rm IR}$ is defined as the divergent part of $D_0(p_1^2, p_2^2, p_3^2, p^2, (p_1+p_2)^2, (p_1+p_3)^2, m_b^2, 0, m_t^2, m_b^2)$ arising from the box diagrams with two bottom quark propagators. They read:

$$\begin{aligned}
D_0^{1,\rm IR} &= \frac{\ln(m_g^2)}{s(1-x_1)}\left[\frac{1}{s\sqrt{\lambda(z_3,a_1,a_2)}}\ln\left(\frac{z_3-a_1-a_2-\sqrt{\lambda(z_3,a_1,a_2)}}{2\sqrt{a_1a_2}}\right)\right], \\
D_0^{2,\rm IR} &= \frac{\ln(m_g^2)}{s(1-x_2)}\left[\frac{1}{s\sqrt{\lambda(z_3,a_1,a_2)}}\ln\left(\frac{z_3-a_1-a_2-\sqrt{\lambda(z_3,a_1,a_2)}}{2\sqrt{a_1a_2}}\right)\right],
\end{aligned} \tag{3.40}$$

and the comparison of Eqs. (3.39) and (3.40) leads to

$$\begin{aligned}
D_0^{1,\rm IR} &= \frac{1}{s(1-x_1)}C_0^{\rm IR}, \\
D_0^{2,\rm IR} &= \frac{1}{s(1-x_2)}C_0^{\rm IR}.
\end{aligned} \tag{3.41}$$

Also the infrared divergent part of Eq.(3.33) can be expressed in terms of $C_0^{\rm IR}$ in the following way:

$$\delta_{\rm soft}^{\rm IR}(m_g) = \frac{\alpha_s}{\pi}C_F\left\{2\ln(m_g^2) + 2s(z_3-a_1-a_2)C_0^{\rm IR}\right\}. \tag{3.42}$$

Notice that the term $2\ln(m_g^2)$ cancels exactly the same logarithm which arises from δZ_q defined in Eq. (3.27). After expressing all the IR divergent functions in terms of $C_0^{\rm IR}$ in Eq. (3.38), we could explicitly verify the analytical cancellation of the IR divergences between the virtual and soft-gluon corrections.

3.5 SUSY QCD corrections

To complete the calculation of the order α_s corrections to $e^+e^- \to t\bar{b}H^-$ and its charge conjugate $e^+e^- \to \bar{t}bH^+$ we have to consider also the SUSY QCD corrections. These are given by the self-energy, triangles and box diagrams depicted in Figs. 3.5 and 3.6. They involve an exchange of a gluino coupling to a quark and a squark. These corrections contain UV divergences, but they are IR finite. In this case, we do not have to consider also real corrections as we did for the QCD corrections, because the radiation of a single gluino from a quark in the final state is forbidden by R-parity. Even in case of models with R-parity violation, the process $e^+e^- \to t\bar{b}H^-\tilde{g}$ would be strongly suppressed or even not possible because of the phase space. Only the self-energies and the vertices 1 to 8 of Fig. 3.5 are divergent. It is necessary to regularize the divergences and to remove them via renormalization. In order to do this, we again use dimensional regularization. However, while the latter is a very convenient regularization scheme for the SM, because it respects all gauge symmetries, it does not respect supersymmetry. In fact, the supersymmetric Ward identities require the same number of fermionic and bosonic degrees of freedom in a supermultiplet. In dimensional regularization all the 4-vectors are continued to D dimensions and therefore, there is a mismatch between the gluon and gluino degrees of freedom, which are equal to $D-2$ and 2, respectively.

One way to overcome this problem is to use the dimensional reduction (DRed) [57]. In this procedure, the integration momenta are still D-dimensional, but all other tensors and spinors are kept 4-dimensional. It has been shown that DRed respects several supersymmetric Ward identities at one-loop level [58]. However, DRed is mathematically not consistent [59]. An alternative way to proceed is to use DReg and to introduce appropriate counterterms in order to restore the broken Ward identities.

In our case, we do not expect any problems with DReg, because we do not have corrections to the quark-squark-gluino coupling, which are known to break supersymmetry. Nevertheless, we checked this statement explicitly. To this aim, we have computed the divergent diagrams in the constrained differential renormalization (CDR) [60], that is equivalent to DRed, as shown in Ref. [50]. We obtained the same analytical expressions using DReg and CDR, thus we conclude that in our calculation DReg can be used without concerns.

In Eq. (3.26) we have given the general expression for the counterterms as a function of the quark self-energy. We now denote the counterterms connected to the SUSY QCD corrections by a tilde, to distinguish them from the counterterm introduced in Eq. (3.27) to eliminate the divergences from the QCD corrections. They read:

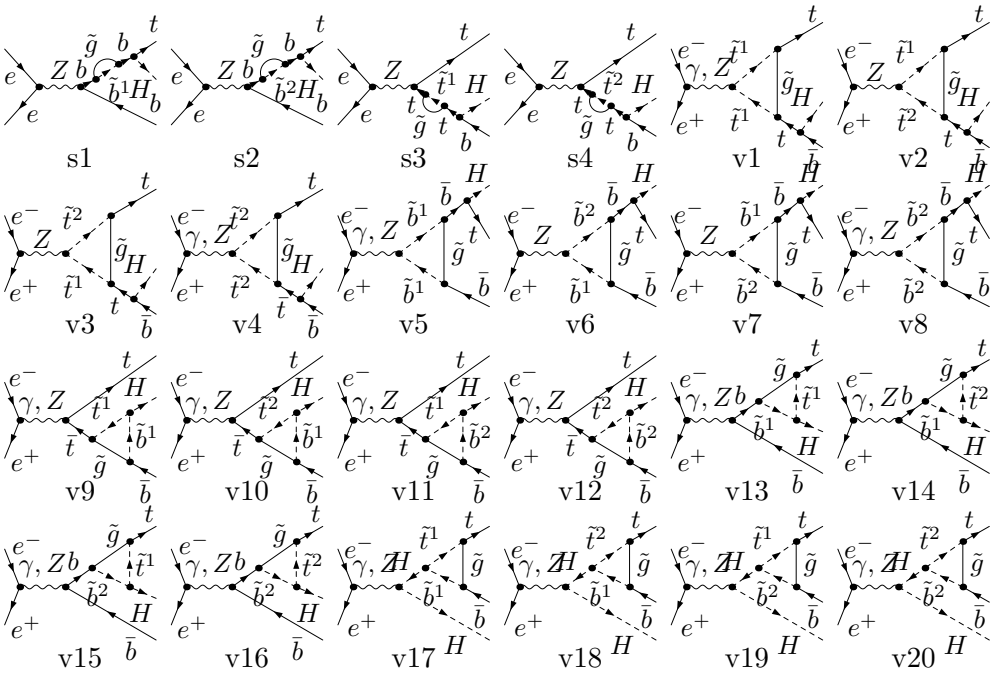

Figure 3.5: Self-Energy and vertex diagrams pertinent to the one-loop SUSY QCD corrections the process $e^+e^- \to t\bar{b}H^-$.

$$
\begin{aligned}
\delta\tilde{m}_q &= -\frac{\alpha_s}{4\pi}C_F \sum_i \Big\{ m_q \left(|S^q_{i1}|^2 + |S^q_{i2}|^2 \right) B_1(m_q^2, m_{\tilde{g}}, m_{\tilde{q}_i}) \\
&\quad + 2m_{\tilde{g}} \,\mathrm{Re}(S^q_{i1} S^{q*}_{i2}) B_0(m_q^2, m_{\tilde{g}}, m_{\tilde{q}_i}) \Big\}, \\
\delta\tilde{Z}^L_q &= -\frac{\alpha_s}{2\pi}C_F \sum_i \Big\{ |S^q_{i1}|^2 B_1(m_q^2, m_{\tilde{g}}, m_{\tilde{q}_i}) \\
&\quad + m_q^2 \left(|S^q_{i1}|^2 + |S^q_{i2}|^2 \right) B_1'(m_q^2, m_{\tilde{g}}, m_{\tilde{q}_i}) \\
&\quad + m_q m_{\tilde{g}} \,\mathrm{Re}(S^q_{i1} S^{q*}_{i2}) B_0(m_q^2, m_{\tilde{g}}, m_{\tilde{q}_i}) \Big\}, \\
\delta\tilde{Z}^R_q &= -\frac{\alpha_s}{2\pi}C_F \sum_i \Big\{ |S^q_{i2}|^2 B_1(m_q^2, m_{\tilde{g}}, m_{\tilde{q}_i}) \\
&\quad + m_q^2 \left(|S^q_{i1}|^2 + |S^q_{i2}|^2 \right) B_1'(m_q^2, m_{\tilde{g}}, m_{\tilde{q}_i}) \\
&\quad + m_q m_{\tilde{g}} \,\mathrm{Re}(S^q_{i1} S^{q*}_{i2}) B_0(m_q^2, m_{\tilde{g}}, m_{\tilde{q}_i}) \Big\},
\end{aligned} \tag{3.43}
$$

where S^q represents the squark mixing matrix defined in Sec. 2.3.3, with $i = 1, 2$, while B_0 and B_1 are scalar two-point functions defined in Appendix A.

We have used the Yukawa mixed scheme also for the SUSY QCD corrections, and the corresponding mass counterterms are given by:

$$
\delta\tilde{m}_q^{\mathrm{Yuk}} = \frac{\alpha_s}{4\pi}C_F m_q \Delta,
$$

$$\delta\tilde{m}_q^{\rm prop} \;=\; \delta\tilde{m}_q, \tag{3.44}$$

where $\delta\tilde{m}_q$ has been defined in Eq. (3.43) and we used the unitarity conditions of the squark mixing matrices S^q:

$$\sum_{k=1}^{2} S^q_{ik} S^{q*}_{jk} = \sum_{k=1}^{2} S^q_{ki} S^{q*}_{kj} = \delta_{ij}. \tag{3.45}$$

3.5.1 Cancellation of the UV divergences

In this section, we describe the structure of the UV divergences which are present in the individual contributions to the SUSY QCD corrections. In the following, we will denote by $\delta\tilde{m}_q^{\rm Yuk}$ and $\delta\tilde{m}_q^{\rm prop}$ the mass counterterm for the Yukawa coupling and for the quark propagator, respectively. In contrast to the one-loop QCD $tbH^\pm$ vertex, the one-loop SUSY QCD $tbH^\pm$ vertex is finite. This can be easily seen by power counting, as in this case we have two scalar (stop, sbottom) and one fermion (gluino) propagators, while in the QCD corrected vertex we had two fermions (top, bottom) and one vector (gluon) propagator. The fact that the $tbH^\pm$ vertex is finite has as a consequence that the following combination of $\delta\tilde{m}_q^{\rm Yuk}$ and the wave function renormalization constant of the quarks $\delta\tilde{Z}_q^L, \delta\tilde{Z}_q^R$:

$$\sum_{q=t,b} \left(\delta\tilde{m}_q^{\rm Yuk} \frac{\partial}{\partial m_q^{\rm Yuk}} + \frac{1}{4}(\delta\tilde{Z}_q^L + \delta\tilde{Z}_q^R) \right) \mathcal{T}_{\rm Born} \tag{3.46}$$

has to be finite as well. The only UV divergent vertices are the corrections to the $\gamma q\bar{q}$ and $Zq\bar{q}$ couplings. As for the QCD corrections, the self-energies and the boxes are UV divergent and UV finite, respectively.

By construction, the divergences contained in the counterterm $\delta\tilde{m}_q^{\rm prop}$ cancel with part of the divergences contained in the self-energy diagrams. The remaining divergences in the self-energy diagrams cancel against a part of the divergences contained in the vertices. The remaining poles in the vertex diagrams combine with the ones of the wave function renormalization constants to a finite result. Next we write down the identities that we could establish between the different contributions. We indicate by δ_v the contribution to the virtual corrections due to the vertex diagrams and with δ_s the contribution from the self-energy diagrams. The diagrams with a virtual photon (Z boson) exchange are indicated with the superscript γ (Z). The number refers to the tree-level and one-loop diagrams, which can be found in Figs. 3.1 and 3.5, respectively.

$$\left[\delta_v^{(\gamma 1)} + \delta_v^{(\gamma 4)} + \frac{1}{2}(\delta\tilde{Z}_t^L + \delta\tilde{Z}_t^R) \mathcal{T}_{\rm Born}^{(\gamma 3)} \right]_{div} \;=\; 0,$$

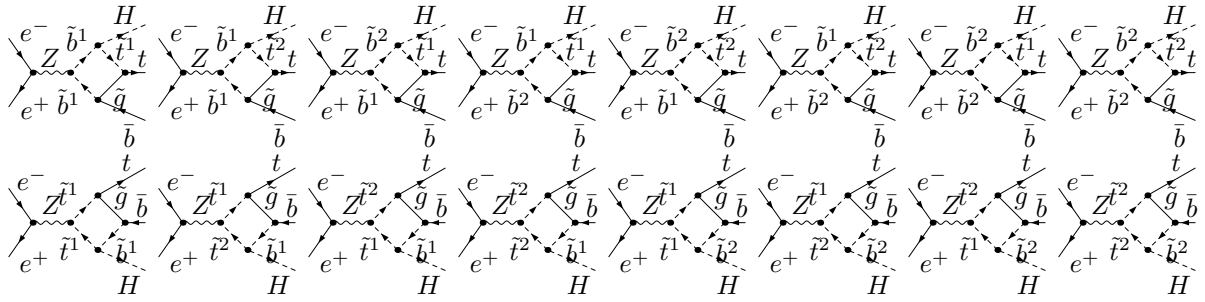

Figure 3.6: Box diagrams pertinent to the one-loop SUSY QCD corrections the process $e^+e^- \to t\bar{b}H^-$.

$$
\begin{aligned}
\left[\delta_v^{(\gamma 5)} + \delta_v^{(\gamma 8)} + \frac{1}{2}(\delta\tilde{Z}_b^L + \delta\tilde{Z}_b^R)\mathcal{T}_{\rm Born}^{(\gamma 2)}\right]_{div} &= 0, \\
\left[\delta_v^{(\gamma 1)} + \delta_v^{(\gamma 4)} + \delta_s^{(\gamma 1)} + \delta_s^{(\gamma 2)} + \delta\tilde{m}_t^{\rm prop}\frac{\partial\mathcal{T}_{\rm Born}^{(\gamma 3)}}{\partial m_q^{\rm prop}}\right]_{div} &= 0, \\
\left[\delta_v^{(\gamma 5)} + \delta_v^{(\gamma 8)} + \delta_s^{(\gamma 3)} + \delta_s^{(\gamma 4)} + \delta\tilde{m}_t^{\rm prop}\frac{\partial\mathcal{T}_{\rm Born}^{(\gamma 2)}}{\partial m_q^{\rm prop}}\right]_{div} &= 0,
\end{aligned}
\tag{3.47}
$$

where $\delta\tilde{Z}_{t,b}^{L,R}$ and $\delta\tilde{m}_{b,t}^{\rm prop}$ are given in Eqs. 3.43 and 3.44. The analogous identities for the Z diagrams read:

$$
\begin{aligned}
\left[\delta_v^{(Z1)} + \delta_v^{(Z2)} + \delta_v^{(Z3)} + \delta_v^{(Z4)} + \frac{1}{2}(\delta\tilde{Z}_t^L + \delta\tilde{Z}_t^R)\mathcal{T}_{\rm Born}^{(Z3)}\right]_{div} &= 0, \\
\left[\delta_v^{(Z5)} + \delta_v^{(Z6)} + \delta_v^{(Z7)} + \delta_v^{(Z8)} + \frac{1}{2}(\delta\tilde{Z}_b^L + \delta\tilde{Z}_b^R)\mathcal{T}_{\rm Born}^{(Z2)}\right]_{div} &= 0, \\
\left[\delta_v^{(Z1)} + \delta_v^{(Z2)} + \delta_v^{(Z3)} + \delta_v^{(Z4)} + \delta_s^{(Z1)} + \delta_s^{(Z2)} + \delta\tilde{m}_t^{\rm prop}\frac{\partial\mathcal{T}_{\rm Born}^{(Z3)}}{\partial m_q^{\rm prop}}\right]_{div} &= 0, \\
\left[\delta_v^{(Z5)} + \delta_v^{(Z6)} + \delta_v^{(Z7)} + \delta_v^{(Z8)} + \delta_s^{(Z3)} + \delta_s^{(Z4)} + \delta\tilde{m}_t^{\rm prop}\frac{\partial\mathcal{T}_{\rm Born}^{(Z2)}}{\partial m_q^{\rm prop}}\right]_{div} &= 0
\end{aligned}
\tag{3.48}
$$

Eventually, we have that the sum of all the SUSY QCD corrections is finite:

$$
\begin{aligned}
\delta_{\rm SQCD} = \frac{2}{|\mathcal{T}_{\rm Born}|^2}\,{\rm Re}\left\{\mathcal{T}_{\rm Born}^*\left[\sum_{q=t,b}\left(\delta\tilde{m}_q^{\rm Yuk}\frac{\partial}{\partial\tilde{m}_q^{\rm Yuk}} + \delta\tilde{m}_q^{\rm prop}\frac{\partial}{\partial\tilde{m}_q^{\rm prop}}\right.\right.\right. \\
\left.\left.\left. + \frac{1}{4}\left(\delta\tilde{Z}_q^L + \delta\tilde{Z}_q^R\right)\right)\mathcal{T}_{\rm Born} + \tilde{\mathcal{T}}_{\rm loop}\right]\right\},
\end{aligned}
\tag{3.49}
$$

where $\tilde{\mathcal{T}}_{loop}$ is the transition-matrix element corresponding to the Feynman diagrams of Figs. 3.5 and 3.6. Note, that in order to obtain the divergence cancellation it was necessary to use the unitarity conditions of the squark mixing matrices S^q given in Eq. (3.45).

Finally, we can generalize Eq.(3.38) and define the one-loop differential cross section which includes the QCD and the SUSY QCD corrections:

$$d\sigma_{1-\mathrm{loop}} = d\sigma_{\mathrm{Born}} \left[1 + \delta_{\mathrm{QCD}} + \delta_{\mathrm{SQCD}}\right], \tag{3.50}$$

where

$$\delta_{\mathrm{QCD}} = \delta_{\mathrm{virt}}(m_g) + \delta_{\mathrm{soft}}(m_g, E_{\mathrm{cut}}) + \delta_{\mathrm{hard}}(E_{\mathrm{cut}}) \tag{3.51}$$

and the expressions for $d\sigma_{\mathrm{Born}}$, $\delta_{\mathrm{virt}}(m_g)$, and $\delta_{\mathrm{soft}}(m_g, E_{\mathrm{cut}})$ can be found in Eqs. (3.11), (3.31), (3.33), respectively, while $\delta_{\mathrm{hard}}(E_{\mathrm{cut}})$ can be obtained from (3.37), rescaling $d\sigma_{\mathrm{hard}}$ through $d\sigma_{\mathrm{Born}}$.

3.6 Numerical results

We now discuss the influence of the order α_s corrections on the total cross sections of $e^+e^- \to t\bar{b}H^-$ and its charge conjugate counterpart, which we add. We first specify our input parameters. We use $m_W = 80.419$ GeV, $m_Z = 91.1882$ GeV, $m_t = 174.3$ GeV, $m_b = 4.6$ GeV, $G_F = 1.16639 \times 10^{-5}$ GeV^{-2} [40], and $\alpha_s^{(5)}(m_Z) = 0.1180$ [61]. We evaluate consistently $\alpha_s^{(n_f)}(\mu)$ and the running quark mass $\overline{m}_q^{(n_f)}(\mu)$ to lowest order in the $\overline{\mathrm{MS}}$ scheme with $n_f = 6$ active quark flavors performing the matching with $n_f = 5$ at scale m_t. The running of α_s and $\overline{m}_q$ is described by the following formulae [62]:

$$\frac{1}{\alpha_s^{(5)}(\mu)} = \frac{1}{\alpha_s^{(5)}(m_Z)} + \frac{\beta_0^{(5)}}{\pi} \ln\frac{\mu^2}{m_Z^2}, \tag{3.52}$$

$$\frac{1}{\alpha_s^{(6)}(\mu)} = \frac{1}{\alpha_s^{(5)}(m_t)} + \frac{\beta_0^{(6)}}{\pi} \ln\frac{\mu^2}{m_t^2}, \tag{3.53}$$

$$\overline{m}_t^{(6)}(\mu) = m_t \left[1 - \frac{\alpha_s^{(6)}(m_t)}{\pi} C_F\right] \left[\frac{\alpha_s^{(6)}(\mu)}{\alpha_s^{(6)}(m_t)}\right]^{\gamma_0/\beta_0^{(6)}}, \tag{3.54}$$

$$\overline{m}_b^{(6)}(\mu) = m_b \left[1 - \frac{\alpha_s^{(5)}(m_b)}{\pi} C_F\right] \left[\frac{\alpha_s^{(5)}(m_t)}{\alpha_s^{(5)}(m_b)}\right]^{\gamma_0/\beta_0^{(5)}} \left[\frac{\alpha_s^{(6)}(\mu)}{\alpha_s^{(6)}(m_t)}\right]^{\gamma_0/\beta_0^{(6)}}, \tag{3.55}$$

where

$$\beta_0^{(n_f)} = \frac{1}{4}\left(\frac{11}{3} C_A - \frac{4}{3} T_F n_f\right),$$
$$\gamma_0 = \frac{3}{4} C_F, \tag{3.56}$$

with $C_A = N_c$ and $T_F = 1/2$, are the first coefficients of the Callan-Symanzik beta function and the quark-mass anomalous dimension, respectively. For simplicity, we use a common renormalization scale μ in $\alpha_s^{(6)}(\mu)$ and $\overline{m}_q^{(6)}(\mu)$.

Concerning the QCD corrections, we study the cases $\sqrt{s} = 500$ GeV and 800 GeV. As for the MSSM input parameters, we consider the ranges $1 < \tan\beta < 40 \approx m_t/m_b$ and $250 < m_H < 320$ GeV if $\sqrt{s} = 500$ GeV or $400 < m_H < 620$ GeV if $\sqrt{s} = 800$ GeV.

As with the QCD corrections, we would like to vary $\tan\beta$ in the range $2 \leq \tan\beta \leq 40$, $250 \leq m_H \leq 320$ GeV for $\sqrt{s} = 500$ GeV and $400 \leq m_H \leq 620$ GeV for $\sqrt{s} = 800$ GeV for the SUSY QCD corrections as well.

The analysis of Ref. [63] shows that the MSSM possesses 124 independent parameters. Of these, 18 parameters correspond to the SM, one corresponds to a Higgs sector parameter (the analogue of the SM Higgs mass), and 105 are genuinely new parameters of the model. If one does not put any restrictions for the SUSY breaking parameters, it becomes extremely difficult to yield concrete predictions which can be checked by experiments. Thus, we have chosen to work within the mSUGRA scenario. We have seen in Sec. 2.3.3 that in this model, besides the SM parameters, we are left with the following SUSY breaking parameters: $\tan\beta, m_0, m_{\frac{1}{2}}, A_0$ and the sign of μ. All other parameters are fixed through the RGE. However, it turns out that the MSSM parameters are nearly independent of the value of A_0, as long as $|A_0| < 500$ GeV at the GUT scale.

For the supersymmetry breaking parameters we fix the values $m_{1/2} = 150$ GeV, $A_0 = 0$ and $\mu > 0$, while we vary m_0 as long as we obtain the desired value of m_H. Moreover, to be consistent with actual experimental limits, we excluded all the points in the parameter space which do not satisfy the following conditions [40]:

$$\begin{aligned}
m_{\tilde{t}_1} &\geq 95\,\text{GeV}, \qquad m_{\tilde{\chi}_1^0} \geq 39\,\text{GeV}, \\
m_{\tilde{b}_1} &\geq 93\,\text{GeV}, \qquad m_{\tilde{\chi}_1^+} \geq 85\,\text{GeV}, \\
m_{\tilde{q}} &\geq 195\,\text{GeV}, \qquad m_{\tilde{g}} \geq 300\,\text{GeV}, \\
m_{\tilde{l}} &\geq 99\,\text{GeV}, \qquad m_{h^0} \geq 91\,\text{GeV}, \\
\Delta\rho &\leq 0.0035,
\end{aligned} \tag{3.57}$$

where $m_{\tilde{t}_1}, m_{\tilde{b}_1}$ are the top, bottom squark masses, $m_{\tilde{q}} = m_{\tilde{u}} = m_{\tilde{d}} = m_{\tilde{c}} = m_{\tilde{s}}$ is the mass of the other squark generations, $m_{\tilde{l}}$ is the general slepton mass, $m_{\tilde{\chi}_1^0}$ and $m_{\tilde{\chi}_1^+}$ are the lightest neutralino (assumed to be the LSP) and chargino masses, $m_{\tilde{g}}$ is the gluino mass, and m_{h^0} the lightest MSSM Higgs mass, respectively. Finally, the quantity $\Delta\rho$ parameterizes the leading universal corrections to the electroweak precision observables induced by the mass splitting between fields in a isospin doublet [64] and it is defined as follows:

$$\Delta\rho = \frac{\Sigma_Z(0)}{m_Z^2} - \frac{\Sigma_W(0)}{m_W^2}, \tag{3.58}$$

with $\Sigma_{Z,W}$ denoting the transverse part the transverse parts of the unrenormalized Z and

W boson self-energies at zero momentum transfer, respectively. $\Delta\rho$ gives the dominant contribution to electroweak precision observables, like the weak mixing angle θ_w and the W boson mass. To compute this quantity one has to consider also loops involving supersymmetrical particles. Therefore, its value can restrict the MSSM parameter space.

Notice that for the numerical evaluation, we have chosen the squark mixing matrices to be real, therefore we have to compute also the mixing angles $\theta_{\tilde{q}}$ defined in Eq.(2.29). We determined the MSSM parameters with the help of the program package SUSPECT [65]. We found that for $\tan\beta = 2$ not all the experimental limits in Eq. (3.57) are satisfied. Therefore, we present only the results for $\tan\beta = 6$ and for $\tan\beta = 40$ for the c.m. energy $\sqrt{s} = 500$ GeV and $\sqrt{s} = 800$ GeV. For these two c.m. energies and $\tan\beta = 40$ we list below typical values obtained with SUSPECT:

- for $\sqrt{s} = 500$ GeV and $m_H = 260$ GeV:
  $m_{\tilde{t}_1} = 311.85$ GeV, $m_{\tilde{t}_2} = 425.8$ GeV, $m_{\tilde{b}_1} = 355.66$ GeV, $m_{\tilde{b}_2} = 409.22$ GeV, $m_{\tilde{q}} = 422.02$ GeV, $m_{\tilde{l}} = 263.63$ GeV, $m_{\tilde{\chi}_1^0} = 59.92$ GeV, $m_{\tilde{\chi}_1^+} = 96.32$ GeV, $m_{\tilde{g}} = 398.45$ GeV and $m_{h^0} = 106.76$ GeV, $\Delta\rho = 1.4 \times 10^{-4}$, $\theta_{\tilde{t}} = 0.98$, $\theta_{\tilde{b}} = 0.61$;

- for $\sqrt{s} = 800$ GeV and $m_H = 410$ GeV:
  $m_{\tilde{t}_1} = 416.44$ GeV, $m_{\tilde{t}_2} = 524.07$ GeV, $m_{\tilde{b}_1} = 486.82$ GeV, $m_{\tilde{b}_2} = 551.88$ GeV, $m_{\tilde{q}} = 600.48$ GeV, $m_{\tilde{l}} = 503.26$ GeV, $m_{\tilde{\chi}_1^0} = 60.81$ GeV, $m_{\tilde{\chi}_1^+} = 98.22$ GeV, $m_{\tilde{g}} = 415.3$ GeV, $m_{h^0} = 108.02$ GeV, $\Delta\rho = 1.1 \times 10^{-4}$, $\theta_{\tilde{t}} = 1.1796$, $\theta_{\tilde{b}} = 0.3146$.

Next, we subdivide the section in three parts. We start in subsection 3.6.1 by selecting the renormalization scheme and scale that are most appropriate for the problem under consideration. In subsection 3.6.2, we present our results for the Born and QCD corrected cross section, while in subsection 3.6.3 we discuss the impact of the SUSY QCD corrections and present the results for the QCD- and SUSY QCD-corrected cross section.

3.6.1 Renormalization scheme and scale dependence

In Sec. 3.4, we have defined the Yukawa mixed scheme, arguing that this choice is preferable, since no large logarithms arise in this scheme. Next, we want to motivate this choice. To this aim, we discuss the results in two other renormalization schemes, namely the OS scheme and another mixed scheme proposed in Ref. [22], in which everything is renormalized in the OS scheme but the bottom mass.

Let us first consider the OS scheme. In this scheme the corrections turned out to be very large and negative (they reduce the Born result by almost 70% for $\tan\beta = 40$). This effect is due to the presence of large logarithms of the type $\ln(m_b/m_H)$ in the

corrections. These logarithmic terms are indeed connected to the renormalization of the Yukawa coupling, namely to the b-quark mass, in an analogous way as in the cases of the decay $h \to b\bar{b}$ [66] and of the decay $H^+ \to t\bar{b}$ [67].[5]

In order to avoid these large logarithms, we propose (see also Ref. [22]) a "mixed scheme" in which the pole b-quark mass m_b is replaced with the running b-quark mass $\overline{m}_b(\mu)$ and the bottom mass counterterms $\delta m_b^{\text{Yuk,prop}}$ with the $\overline{\text{MS}}$ mass counterterm:

$$\delta\overline{m}_b = -\frac{3\alpha_s}{4\pi} C_F m_b \Delta. \tag{3.59}$$

This mixed scheme introduces a dependence on the choice of the scale, at which we compute the running b-quark mass. We have studied the μ dependence of the Born and QCD-corrected results in these two different renormalization schemes. The OS scheme uses the pole masses m_t and m_b as basic parameters, while the mixed scheme (denoted by the label $\overline{\text{MS}}$) uses m_t and the $\overline{\text{MS}}$ mass $\overline{m}_b^{(6)}(\mu)$. Both schemes employ the $\overline{\text{MS}}$ definition of $\alpha_s^{(6)}(\mu)$. As a typical example, we consider in Fig. 3.7 the case of $\sqrt{s} = 500$ GeV, $\tan\beta = 40$, and $m_H = 260$ GeV. We allow μ to vary over two orders of magnitude, from 10 to 1000 GeV. In the OS scheme, the Born result is μ independent, while the QCD-corrected one depends on μ via $\alpha_s^{(6)}(\mu)$. In the mixed scheme, the μ dependence enters at leading-order (LO) via $\overline{m}_b^{(6)}(\mu)$ and at NLO via $\alpha_s^{(6)}(\mu)$ and $\overline{m}_b^{(6)}(\mu)$. Obviously, the theoretical uncertainties due to scheme and typical scale variations are significantly reduced as we pass from LO to NLO. On the one hand, the OS-scheme to mixed-scheme ratio is brought down to the vicinity of unity, from 1.46–2.92 to 0.78–1.43, depending on the value of μ. On the other hand, the μ dependence within the mixed scheme is reduced by a factor of 5, from 0.020 fb to 0.004 fb in absolute terms. Furthermore, we observe that, in the OS scheme, the QCD corrections lead to a dramatic reduction of the cross section, by 36–67%. As explained above, this is because they contain large logarithmic terms of the form $\alpha_s^{(6)}(\mu)\ln(M^2/m_b^2)$, where M is a generic mass scale in the ball park of some suitable average of the final-state-particle masses, m_b, m_t, and m_H. In the mixed scheme with μ of order M, such terms are shifted from the QCD corrections to the Born result, where they are absorbed into the running of $\overline{m}_b^{(6)}(\mu)$ from $\mu = m_b$ to $\mu = M$. This is reflected in Fig. 3.7 by the fact that, in the mixed scheme, the QCD corrections are relatively modest, ranging from -39% to $+30\%$.

We now proceed to compare the mixed scheme and the Yukawa mixed scheme. We recall that in the latter, we use the $\overline{\text{MS}}$ mass exclusively in the Yukawa coupling, while everywhere else we use the pole mass. For theoretical consistency, we decided to treat

[5] For the relation between the fermion pole mass and the $\overline{\text{MS}}$ Yukawa coupling see also [68].

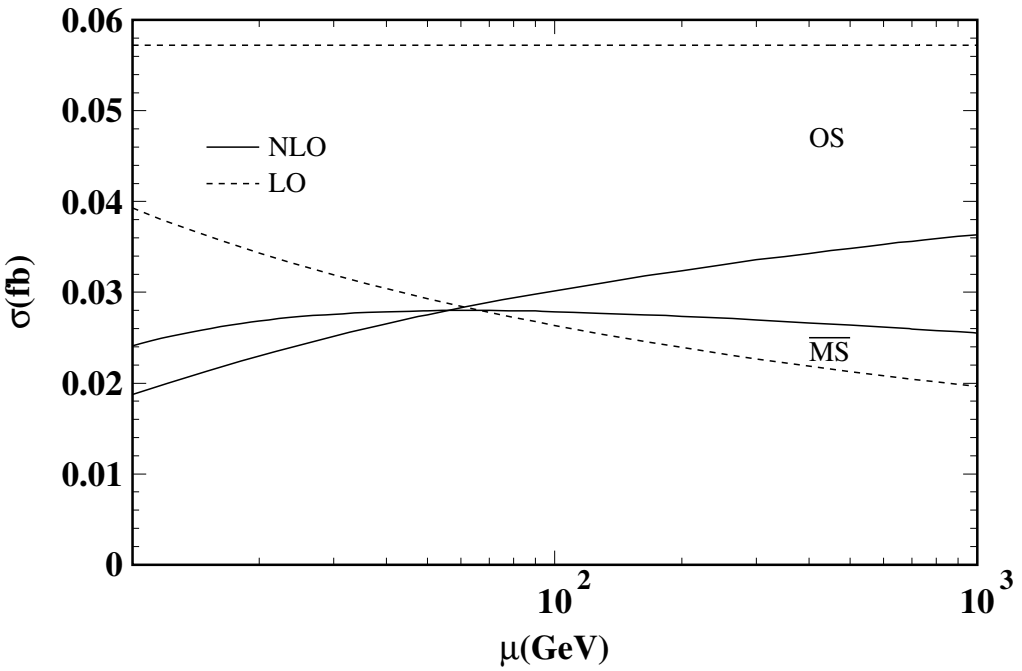

Figure 3.7: Total cross section of $e^+e^- \to t\bar{b}H^-, \bar{t}bH^+$ as a function of μ for $\sqrt{s} = 500$ GeV, $\tan\beta = 40$, and $m_H = 260$ GeV. The dashed and solid curves correspond to the Born and QCD-corrected results, respectively. The upper and lower sets of curves refer to the OS and mixed schemes, respectively.

the top mass in the same way as the bottom mass, even if the logarithms $\ln(M^2/m_t^2)$ do not give rise large corrections. Defining the three different sources for the quark masses as $m^{\rm Yuk}$ for the mass in the Yukawa coupling, $m^{\rm prop}$ for the mass in the propagator and $m^{\rm bound}$ for the mass in the integrations boundaries, we summarize the differences between the three schemes in Tab. 3.1.

In Fig. 3.8, we investigate the scale dependence of the mixed scheme and the Yukawa mixed scheme. One can see that the results for LO and NLO QCD cross sections remain almost unchanged passing from the mixed scheme to the Yukawa mixed scheme. Actually, this result was expected, as on the one hand, the top quark mass appears in the cross section only in the combination $m_t/\tan\beta$ and thus is suppressed for $\tan\beta = 40$. On the other hand, changing $\overline{m}_b$ to m_b in the phase-space boundaries and the bottom propagator only lead to negligible variations in the numerical results.

Let us now turn to the question of how to fix the value of μ in a reasonable way. Scale-setting procedures frequently discussed in the literature include the concept of fastest

Masses and cts	OS scheme	Mixed scheme	Yukawa mixed scheme
m_b^{Yuk}	m_b	$\overline{m}_b$	$\overline{m}_b$
m_t^{Yuk}	m_t	m_t	$\overline{m_t}$
m_b^{prop}	m_b	$\overline{m}_b$	m_b
m_t^{prop}	m_t	m_t	m_t
m_b^{bound}	m_b	$\overline{m}_b$	m_b
m_t^{bound}	m_t	m_t	m_t
δm_b^{Yuk}	δm_b	$\delta\overline{m}_b$	$\delta\overline{m}_b$
δm_t^{Yuk}	δm_t	δm_t	$\delta\overline{m_t}$
δm_b^{prop}	δm_b	$\delta\overline{m}_b$	δm_b
δm_t^{prop}	δm_t	δm_t	δm_t

Table 3.1: Choice for quark masses and relative counterterms (cts) depending on the renormalization scheme.

apparent convergence (FAC) [69], the principle of minimal sensitivity (PMS) [70], and the proposal by Brodsky, Lepage, and Mackenzie (BLM) [71] to resum the leading light-quark contribution to the renormalization of the strong-coupling constant. The latter is not yet applicable to the problem under consideration, which is of LO in the strong-coupling constant. The FAC and PMS prescriptions lead us to select the values of μ where the Born and QCD-corrected results intersect and where the latter exhibits a local extremum, respectively. In Ref. [22], we based our choice of the scale on Fig. 3.7. From this plot, we observed that these two μ values approximately coincide, at about 60 GeV. Incidentally, in the close vicinity of these two μ values, also the QCD-corrected results in the OS and mixed schemes cross over, so that also the scheme dependence at NLO vanishes in this neighborhood, at least as for the two schemes considered here. Since the μ dependence is logarithmic, it is suggesting that a democratic way of combining the three scales m_b, m_t, and m_H is by taking their geometric means, $\mu = \sqrt[3]{m_b m_t m_H}$. In the present case, this educated guess yields $\mu \approx 60$ GeV, which nicely agrees with the triply distinguished point identified above. We checked that this choice works similarly well for the case of $\sqrt{s} = 800$ GeV, $\tan\beta = 40$, and $m_H = 410$ GeV.

Finally, in Fig. 3.9, we have studied the μ dependence of the LO total cross section, of the QCD-corrected one (NLO QCD), and of the cross section including of QCD and SUSY QCD corrections (NLO QCD + SQCD). All the curves are obtained in the Yukawa mixed scheme. We can see that the crossing point between the LO and the QCD- and SUSY

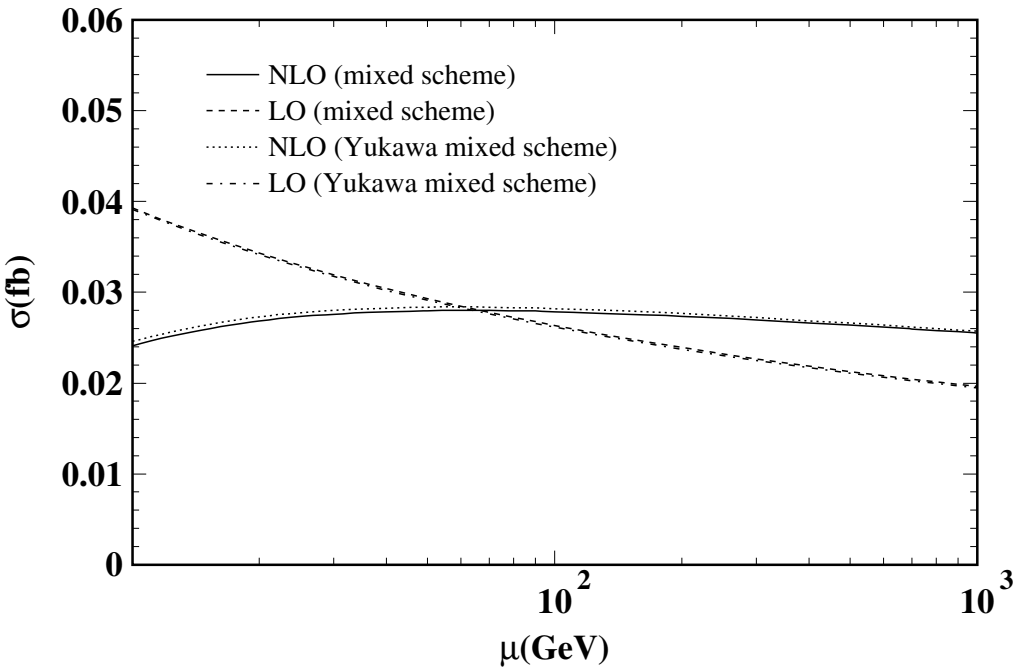

Figure 3.8: Total cross section of $e^+e^- \to t\bar{b}H^-, \bar{t}bH^+$ as a function of μ for $\sqrt{s} = 500$ GeV, $\tan\beta = 40$, and $m_H = 260$ GeV. The LO and NLO results for the mixed scheme and the Yukawa mixed scheme are compared.The LO curves in the two schemes almost coincide (dashed and dashed-dotted curves). The solid curve refers to the NLO in the mixed scheme whereas the dotted curve to the Yukawa mixed scheme.

QCD-corrected results is shifted to the much smaller scale $\mu \approx 10$ GeV. However, this scale seems quite unnatural considering the big energy scales involved in our process. Observing that the SUSY QCD corrections are not very large near to the point $\mu = \sqrt[3]{m_b m_t m_H}$, we can argue that this is still a suitable scale for our calculation.

3.6.2 QCD corrections

Let us first consider the results for the Born and QCD corrected cross section. Figures 3.10 and 3.11 refer to $\sqrt{s} = 500$ GeV, while Figs. 3.12 and 3.13 refer to $\sqrt{s} = 800$ GeV. We investigate the m_H dependence for various values of $\tan\beta$ in Figs. 3.10 and 3.12 and the $\tan\beta$ dependence for typical values of m_H in Figs. 3.11 and 3.13. In each figure, we present the Born and QCD-corrected results in the Yukawa mixed scheme with $\mu = \sqrt[3]{m_b m_t m_H}$. For comparison, in Figs. 3.11 and 3.13, we also present the corresponding results in the OS scheme with the same scale choice.

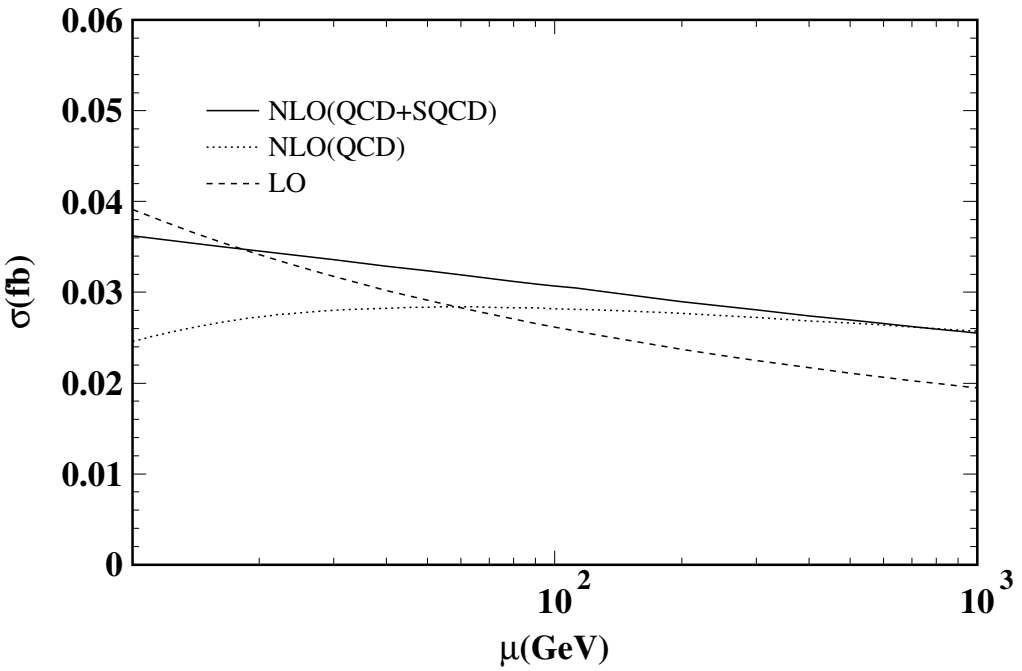

Figure 3.9: Total cross section of $e^+e^- \to t\bar{b}H^-, \bar{t}bH^+$ as a function of μ for $\sqrt{s} = 500$ GeV, $\tan\beta = 40$, and $m_H = 260$ GeV. The dashed, pointed and solid curves correspond to the Born, QCD- and SUSY QCD-corrected results. They were all computed in the Yukawa mixed scheme.

We observe that the total cross sections exhibit minima close to $\tan\beta \approx \sqrt{m_t/m_b} \approx 6$, independently of order and scheme. This may be understood by observing that the average strength of the $t\bar{b}H^-$ coupling, which is proportional to $\sqrt{m_t^2 \cot^2\beta + m_b^2 \tan^2\beta}$, is then minimal [72]. Depending on $\sqrt{s}$, $\tan\beta$, and m_H, the QCD corrections may be of either sign. By construction, they are generally rather modest in the mixed scheme, although they may reach a magnitude of 50% for specific values of $\sqrt{s}$, $\tan\beta$, and m_H, as may be seen from Fig. 3.12. On the other hand, in the OS scheme, the QCD corrections lead to a substantial reduction in cross section at large values of $\tan\beta$, as can be seen in Figs. 3.11 and 3.13. As explained above, this may be attributed to large logarithms arising from the $t\bar{b}H^-$ Yukawa coupling.

It is interesting to investigate the relative importance of the contributions due to photon and Z-boson exchanges. To this end, we evaluate the photon-induced part of the total cross section by putting $\mathcal{V}_e = \mathcal{A}_e = 0$ and compare it with the full result. We find that the bulk of the total cross section is due to photon exchange. In fact, for the typical

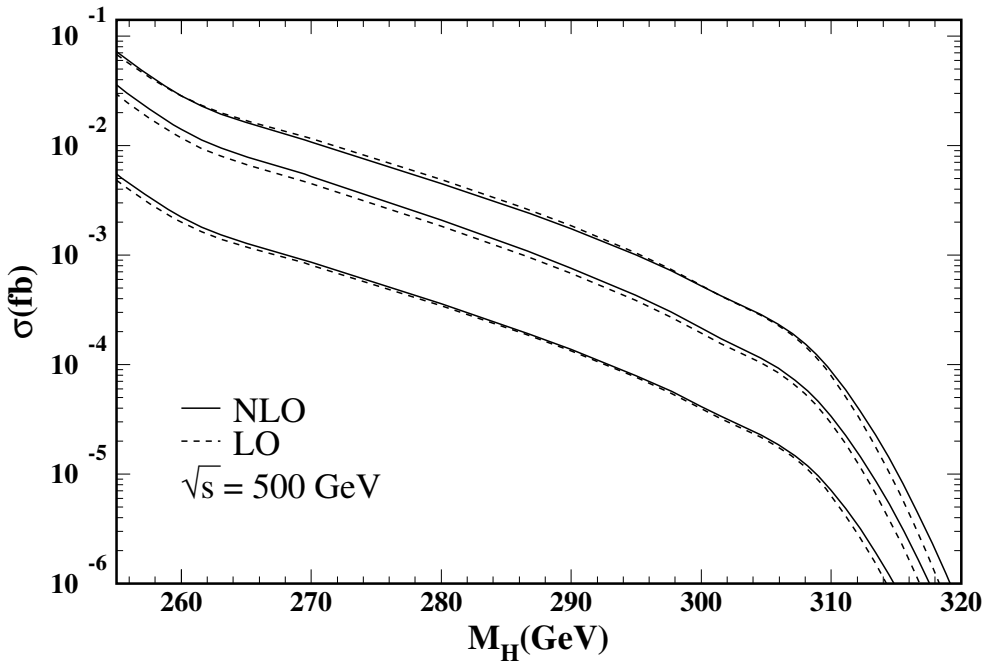

Figure 3.10: Total cross section of $e^+e^- \to t\bar{b}H^-, \bar{t}bH^+$ without (dotted curves) and with (solid curves) QCD corrections in the Yukawa mixed scheme as a function of m_H for $\sqrt{s} = 500$ GeV and various values of $\tan\beta$. The middle, lower, and upper sets of curves correspond to $\tan\beta = 2$, 6, and 40, respectively.

values $\sqrt{s} = 500$ GeV and $m_H = 260$ GeV, the photon-induced part exhausts 78%, 80%, and 82% of the full result if $\tan\beta = 2, 6$, and 40, respectively.

3.6.3 SUSY QCD corrections

Let us now turn to the SUSY QCD corrections. Notice that they have been evaluated in the Yukawa mixed scheme. For consistency, also the QCD results plotted in the next figures are presented in the same scheme. As we already mentioned, the results do not differ substantially from those computed in the mixed scheme. Figures. 3.14 and 3.15 both refer to the c.m. energy $\sqrt{s} = 500$ GeV, but in the first figure we have chosen $\tan\beta = 6$, while in the second one $\tan\beta = 40$. They represent the results for the the relative QCD and SUSY QCD corrections $\delta_{\rm QCD}$ and $\delta_{\rm SQCD}$, defined in Eqs. (3.51) and (3.49), respectively. For $\sqrt{s} = 800$ GeV, the same quantities are shown in Figs 3.16 and 3.17, which refer to $\tan\beta = 6$ and $\tan\beta = 40$, respectively. We investigate their dependence on m_H, which varies from 250 GeV to 320 GeV for $\sqrt{s} = 500$ GeV and

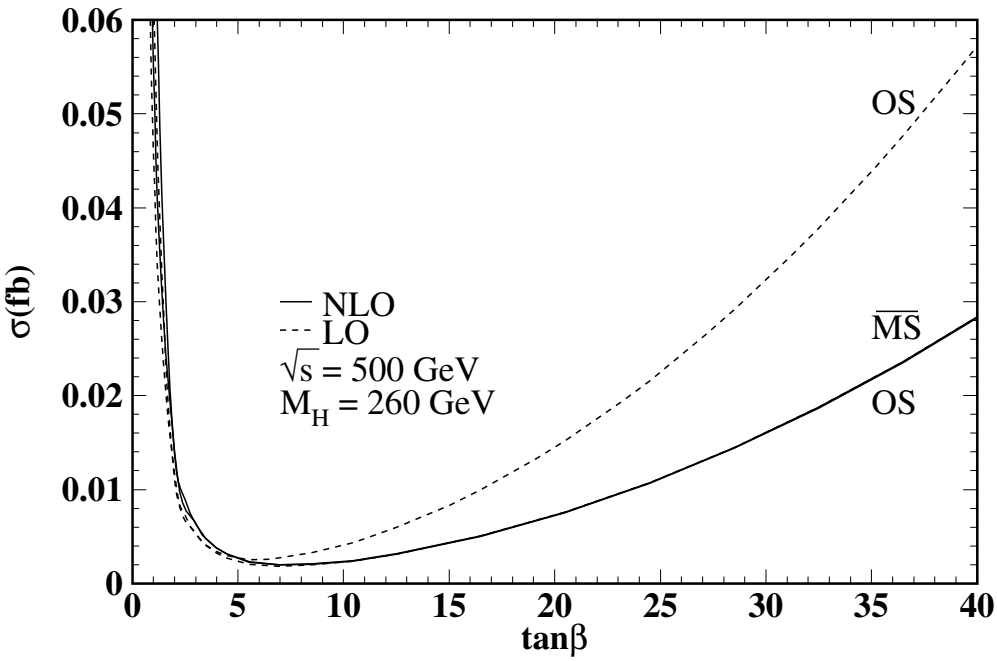

Figure 3.11: Total cross section of $e^+e^- \to t\bar{b}H^-, \bar{t}bH^+$ without (dotted curves) and with (solid curves) QCD corrections as a function of $\tan\beta$ for $\sqrt{s} = 500$ GeV and $m_H = 260$ GeV. The upper and lower sets of curves refer to the OS and Yukawa mixed schemes, respectively.

from 400 GeV to 620 GeV for $\sqrt{s} = 800$ GeV. At the same time, we indicate also the correspondent value of the universal scalar mass m_0.

One can see that the SUSY QCD corrections are positive and vary between 15% and 16% of the Born cross section for $\sqrt{s} = 500$ GeV and $\tan\beta = 6$ (Fig. 3.14), and approximately from 14% to 15% for $\tan\beta = 40$ (Fig. 3.15). For $\sqrt{s} = 800$ GeV, they are about 15% for $\tan\beta = 6$ (Fig. 3.16) and slightly more than 12% for $\tan\beta = 40$ (Fig. 3.17). Notice that the QCD corrections become very large in comparison to the Born cross section for the Higgs mass values near to the kinematic limit, i.e. close to $m_H = 320$ GeV for $\sqrt{s} = 500$ GeV and $m_H = 620$ GeV for $\sqrt{s} = 800$ GeV, where the cross section goes to zero. Indeed, this is due to a Coulomb singularity arising from the diagrams where a gluon is exchanged between the final state quarks. For this reason, the Born cross section approches zero whereas the QCD-corrected one goes to a finite value. A common characteristic of the four figures under consideration, is that in all of them the curve representing the relative SUSY QCD corrections is almost constant. To understand

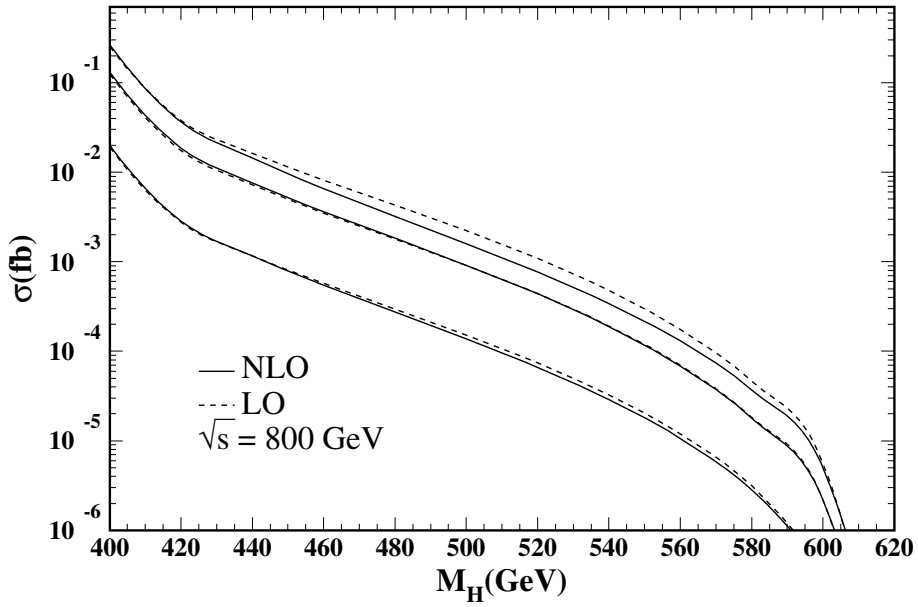

Figure 3.12: Same as in Fig. 3.10, for $\sqrt{s} = 800$ GeV.

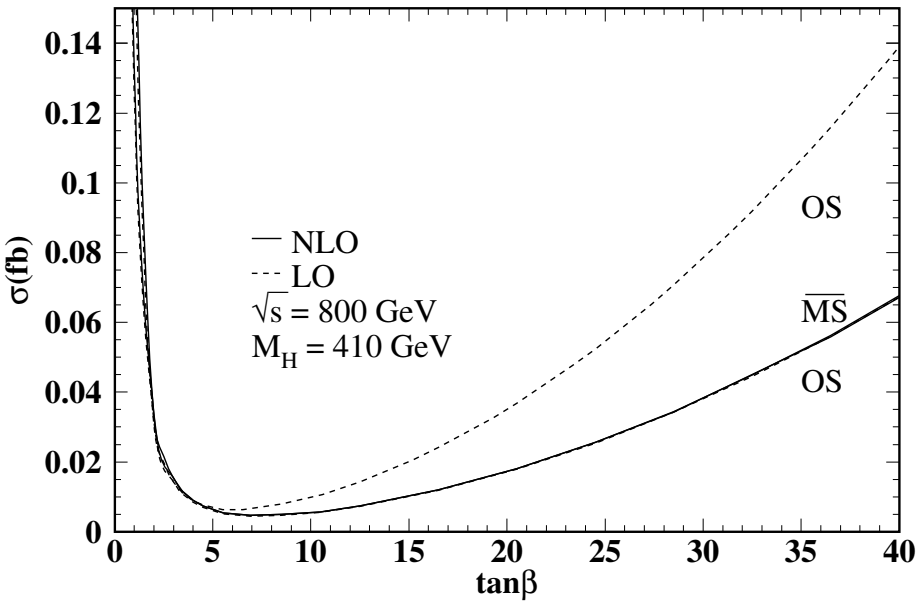

Figure 3.13: Same as in Fig. 3.11, for $\sqrt{s} = 800$ GeV and $m_H = 410$ GeV.

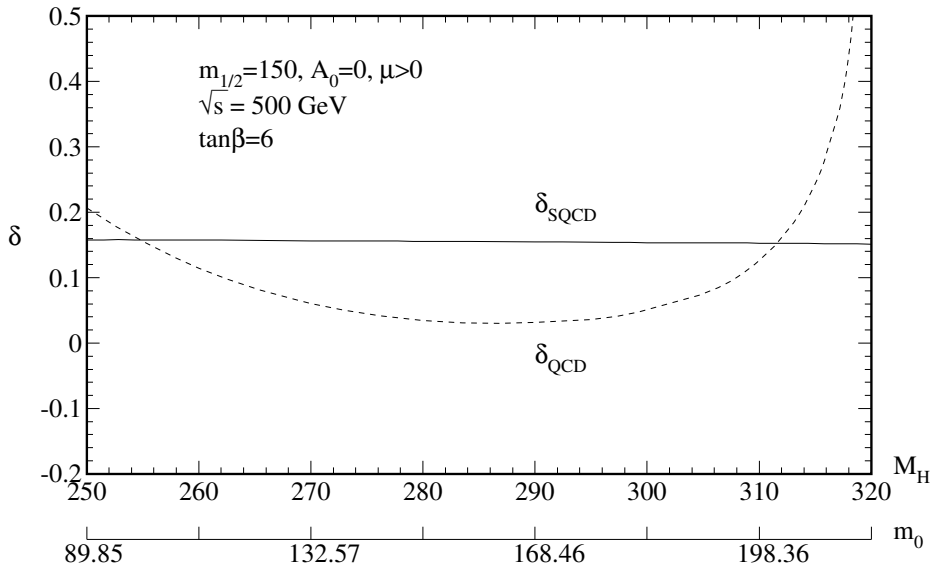

Figure 3.14: QCD (dotted curve) and SUSY QCD (solid curve) corrections for $e^+e^- \to t\bar{b}H^-, \bar{t}bH^+$ as a function of m_H and m_0, for $\sqrt{s} = 500$ GeV, $\tan\beta = 6$, $m_{1/2} = 150$ GeV, $A_0 = 0$ and $\mu \geq 0$.

the reason for this behaviour, we have plotted in Fig. 3.18 the dependence on m_H of the individual terms contributing to the SUSY QCD corrections, namely the corrections arising from the counterterms and from the self-energy, vertex, and box diagrams. We are aware that all these contributions except the box diagrams, taken individually, are UV divergent and that only their sum is finite. We subtract these divergences in the $\overline{\text{MS}}$ scheme. In this way, we introduce an additional dependence on the renormalization scheme and on the scale μ. We set also in this case $\mu = \sqrt[3]{m_b m_t m_H}$. Nevertheless, Fig. 3.18 can still be useful to understand which are the dominant contributions to the corrections for our choice of parameters.

In fact, we see that the dominant contributions are given by the counterterms. Among these, we have ascertained that the largest contribution comes from the wave function renormalization constants. This explains why the SUSY QCD-corrected cross section seems to be almost proportional to the Born cross section, or, in other words, why the relative corrections are almost constant (see Eq. (3.49)). On the other hand, we observe in Fig. 3.18 that all other virtual contributions are quite small. In particular, those arising from the box diagrams are almost zero. This fact can be understood by considering that

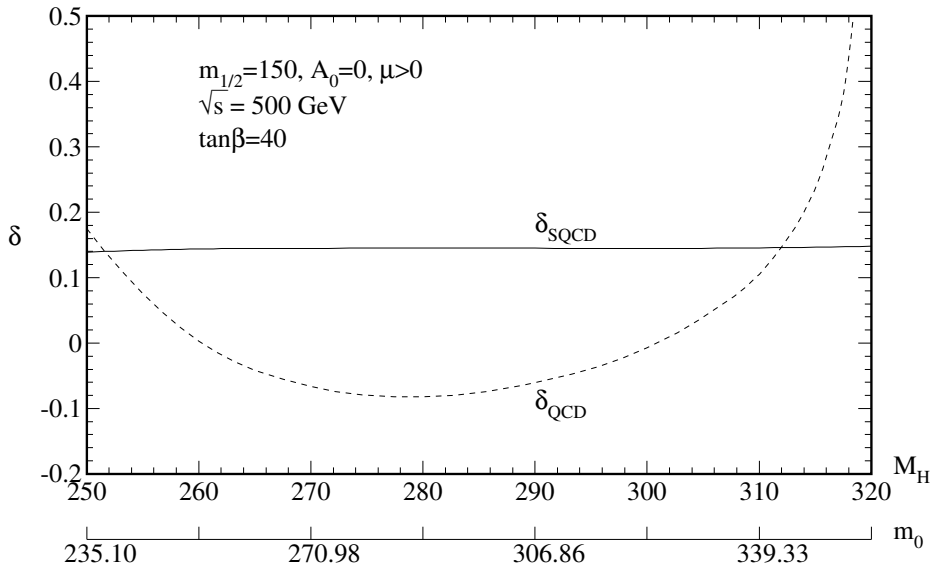

Figure 3.15: The same as in Fig. 3.14 with $\tan\beta = 40$.

in all loops we have very large masses and the box diagram contributions are specially strongly suppressed.

Finally, we present the results for the total cross section including the QCD and the SUSY QCD corrections. In Figs. 3.19 and 3.20, we have investigated the $\tan\beta$ dependence of the Born, the QCD-corrected and QCD- and SUSY QCD-corrected cross section. In Fig. 3.19, we have $\sqrt{s} = 500$ GeV and $m_H = 260$ GeV. Notice that for $\tan\beta \leq 4$ we have set the SUSY QCD corrections to zero, as not all the experimental constrains given in Eq. (3.57) are satisfied. Therefore, for $\tan\beta \leq 4$ the total cross section coincides with the QCD-corrected one. The same is true also for Fig. 3.20, where the precluded region for the SUSY QCD corrections is $\tan\beta \leq 3$. The QCD-curves almost coincide with the Born results for $\tan\beta \geq 6$. The SUSY QCD corrections are positive and they become bigger for larger $\tan\beta$ values up to $\tan\beta = 40$ where, together with the QCD corrections, they increase the Born cross section from 0.028 to 0.033 fb. In Fig.3.20, we observe that also for $\sqrt{s} = 800$ GeV and $m_H = 410$ GeV they are positive and slowly growing for larger values of $\tan\beta$. For $\tan\beta = 40$ they increase the cross section from 0.067 to 0.076 fb.

The e^+e^- TeV Energy Superconducting Linear Accelerator (TESLA), which is being developed and planned at DESY, has a design luminosity of $3.4 \times 10^{34}\text{cm}^{-2}\text{s}^{-1}$ ($5.8 \times 10^{34}\text{cm}^{-2}\text{s}^{-1}$) at $\sqrt{s} = 500$ GeV ($\sqrt{s} = 800$ GeV) per year [7]. Thus, a total cross section

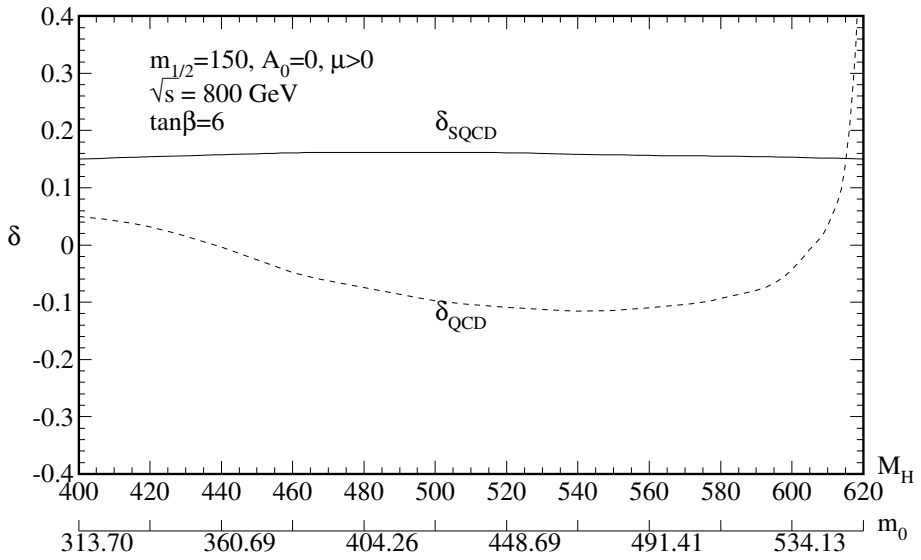

Figure 3.16: QCD (dotted curve) and SUSY QCD (solid curve) corrections for $e^+e^- \to t\bar{b}H^-, \bar{t}bH^+$ as a function of m_H and m_0, for $\sqrt{s} = 800$ GeV, $\tan\beta = 6$, $m_{1/2} = 150$ GeV, $A_0 = 0$ and $\mu \geq 0$.

of typically 0.03 fb (0.07 fb) will yield about 10 (40) signal events per year.

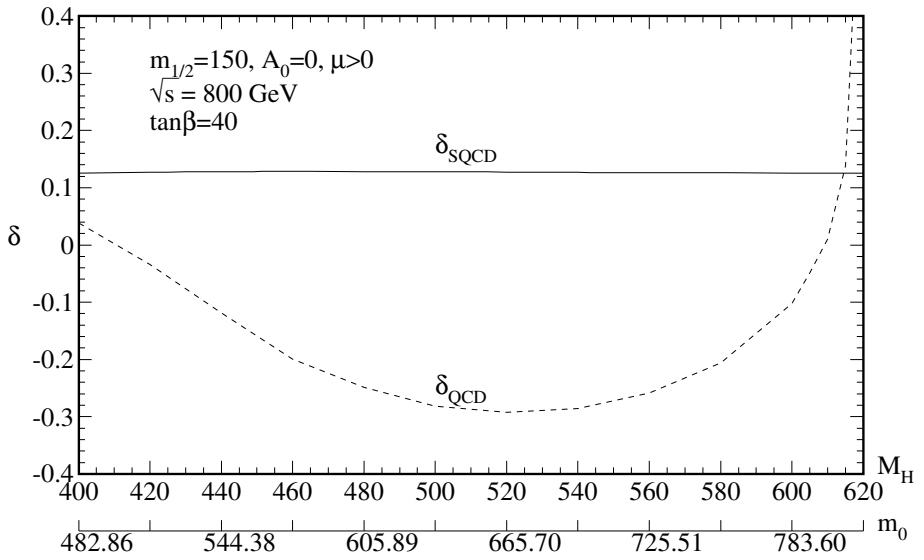

Figure 3.17: The same as in Fig. 3.16 with $\tan\beta = 40$.

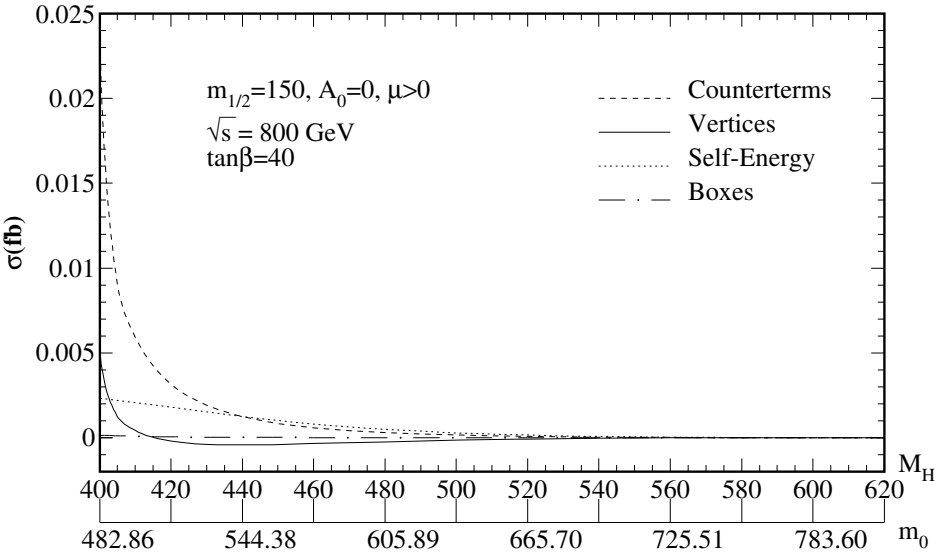

Figure 3.18: Contributions to the SUSY QCD corrections for $e^+e^- \to t\bar{b}H^-, \bar{t}bH^+$ as a function of m_H and m_0, for $\sqrt{s} = 800$ GeV, $\tan\beta = 40$, $m_{1/2} = 150$ GeV, $A_0 = 0$ and $\mu \geq 0$.

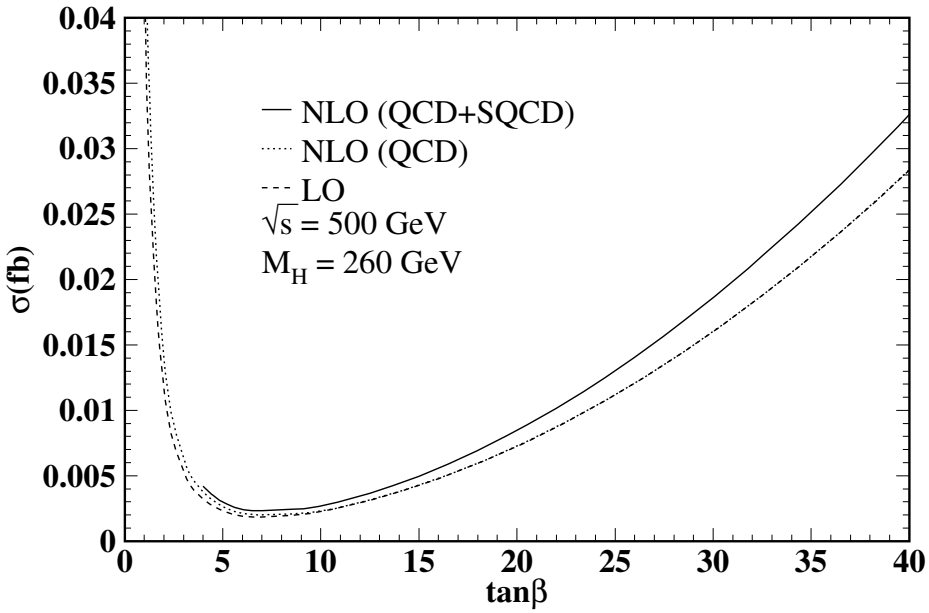

Figure 3.19: Total cross section of $e^+e^- \to t\bar{b}H^-, \bar{t}bH^+$, at tree level (dashed curve), including QCD corrections (dotted curve) and both QCD and SUSY QCD corrections (solid curve) as a function of $\tan\beta$ for $\sqrt{s} = 500$ GeV, $m_H = 260$, $m_{1/2} = 150$ GeV, $A_0 = 0$ and $\mu \geq 0$.

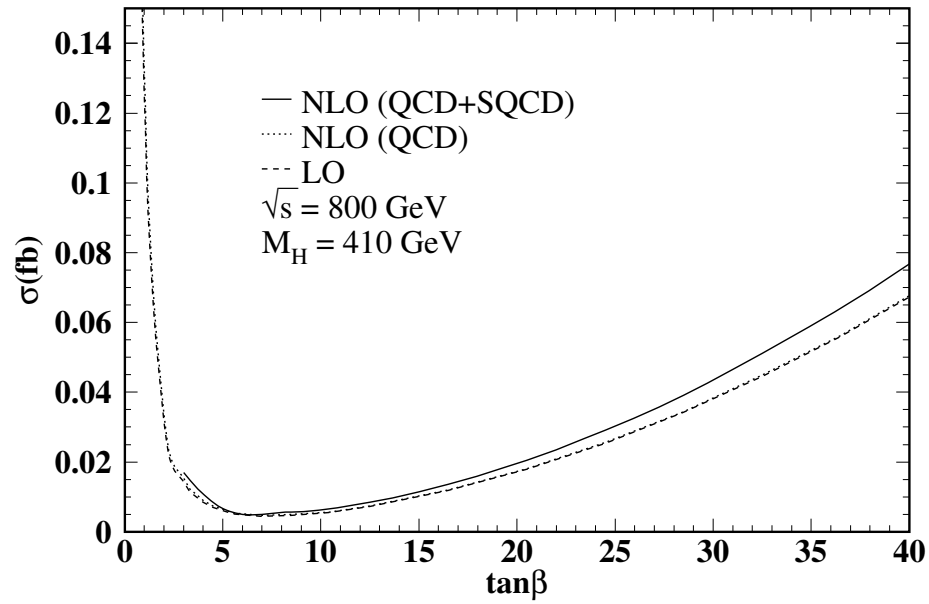

Figure 3.20: Same as in Fig. 3.19, for $\sqrt{s} = 800$ GeV, $m_H = 410$.

Chapter 4

SM Higgs Boson Bremsstrahlung

4.1 Introduction

In this chapter, we shall discuss the SM process $e^+e^- \to t\bar{t}h$. It is has first been considered at the Born level in Ref. [19] and at order α_s in Refs. [23, 24]. The product of a Higgs boson in association with two top quarks is a very important process to be measured at a future linear collider like TESLA. Its cross section depends sensitively on the top Yukawa coupling, which will be directly accessible if $m_h < 2m_t$. This process leads to a distinctive signature consisting of two W bosons and four b-quark jets. The experimental accuracy on the determination of the top Yukawa coupling has been studied in Ref. [73] and amounts to 5.5% for $\sqrt{s} = 800$ GeV and $L = 1000$ fb^{-1} (see also [7]).

Given the importance of the reaction $e^+e^- \to t\bar{t}h$, we present here a third independent calculation for the total cross section to the order α_s. We found analytical agreement with the Born results of Ref. [19] , and numerical agreement with the NLO results of Refs. [23, 24].

We note in passing, that in the literature, also the corresponding MSSM processes $e^+e^- \to t\bar{t}h^0, H^0, A^0$ have been considered [74]. In the case of the lightest MSSM neutral Higgs boson, the calculation of the corrections goes along the same lines. Next to the trivial change of the coupling factors, only one new diagram has to be considered, which involves the CP-odd Higgs boson, A^0. In the limit where $m_{A^0,H^0,H^\pm} \gg m_Z$, A^0, H^0 and $H^\pm$ decouple from the theory and we are left with an Higgs sector which is identical to the SM one, except for the couplings to the gauge bosons and the ones to the fermions. The former can be obtained from the SM ones, by multiplying with $\sin(\beta - \alpha)$. On the other hand, a factor $\cos\alpha/\sin\beta$ $(-\sin\alpha/\cos\beta)$ is needed in the case of the Yukawa couplings to the up-type (down-type) quarks.

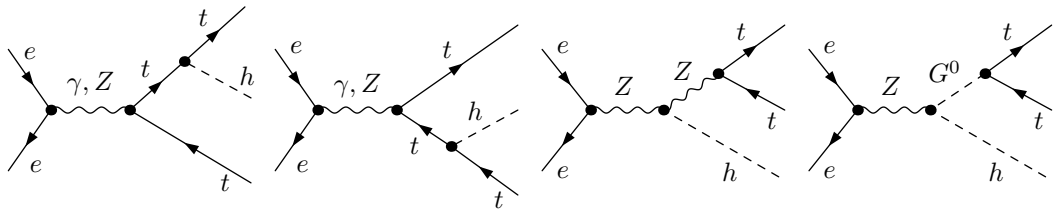

Figure 4.1: Tree-level Feynman diagrams pertinent to the process $e^+e^- \to t\bar{t}h$.

The outline of the chapter is the following: in Sec. 4.2, we present the results for the Born cross section and in Sec. 4.3, we shall consider the QCD corrections to the order α_s. Like in the case of the single charged Higgs boson production, we have to combine virtual and real corrections in order to obtain a finite result. In Sec. 4.4, we present updated numerical results for the total cross section.

4.2 Born cross section

Regarding the kinematics of $e^+e^- \to t\bar{t}h$, we shall adopt the same notation as in Sec. 3.3, with k_1 and k_2 being the four-momenta of the incoming electron and positron and p_1, p_2, and p_3, those of the t quark, $\bar{t}$ quark, and the SM h boson, respectively. In analogy to Eq. (3.11), we write

$$d\sigma^{\rm SM}_{\rm Born} = \frac{1}{2s}\,\frac{1}{4}|\mathcal{T}^{\rm SM}_{\rm Born}|^2 d{\rm PS}_3(p; p_1, p_2, p_3), \tag{4.1}$$

where $\mathcal{T}^{\rm SM}_{\rm Born}$ is the transition-matrix element corresponding to the Feynman diagrams of Fig. 4.1, and the summation over the lepton and quark spins is implied.

We can use the expressions for the lepton tensor and the three-particle phase space given in Eqs. (3.9) and (3.13), respectively. Since in this case we have $a_1 = a_2$, the scalar products of Eq. (3.14) are simplified as follows:

$$\begin{aligned} p_1 \cdot p_2 &= \frac{s}{2}(z_3 - 2a_1), \\ p_1 \cdot p_3 &= \frac{s}{2}(1 - x_1 - 2a_3), \\ p_1 \cdot p_3 &= \frac{s}{2}(1 - x_2 - 2a_3), \end{aligned} \tag{4.2}$$

where $z_3 = 1 + a_3 - x_3$ is defined in Eq. (3.15). Using the dimensionless variables defined in Eq. (3.10), the doubly-differential Born cross section reads:

$$\frac{d\sigma^{\rm SM}_{\rm Born}}{dx_1\,dx_2} = \frac{G_F^3 m_Z^4}{32\pi^3\sqrt{2}}\left[\mathcal{Q}_e^2 g_{\gamma\gamma}(x_1,x_2) + \mathcal{Q}_e\mathcal{V}_e g_{\gamma Z}(x_1,x_2) + \left(\mathcal{V}_e^2 + \mathcal{A}_e^2\right) g_{ZZ}(x_1,x_2)\right], \tag{4.3}$$

where $\mathcal{Q}_e$, $\mathcal{V}_e$, and $\mathcal{A}_e$ are defined in Eq. (3.17), while the form factors $g_{\gamma\gamma}(x_1, x_2)$, $g_{\gamma Z}(x_1, x_2)$, and $g_{ZZ}(x_1, x_2)$ are listed in Appendix B. Notice that $g_{\gamma\gamma}(x_1, x_2)$ can be obtained from the expression for $f_{\gamma\gamma}(x_1, x_2)$ defined in Appendix B. To this end, one has to set in $f_{\gamma\gamma}(x_1, x_2)$ $a_1 = a_2$, $\tan\beta = -1$, $\mathcal{H}_\gamma = 0$, and finally divide by a factor 2. With these substitutions, one can pass from the $t\bar{b}H^-$ coupling to the SM $t\bar{t}h$ one. It is not possible to obtain in the same way also g_{ZZ} and $g_{\gamma Z}$, because for the neutral Higgs we have two more diagrams, where the Higgs boson is emitted from the Z boson or from the Goldstone boson (G_0) line. For $a_1 = a_2$, also the integration boundaries assume a simpler form and Eqs. (3.18) and (3.19) can be re-written as follows:

$$\begin{aligned} 2\sqrt{a_1} \;&<\; x_1 \;<\; 1 + a_1 - \sqrt{a_1 a_3}, \\ x_2^- \;&<\; x_2 \;<\; x_2^+, \end{aligned} \tag{4.4}$$

with

$$x_2^\pm = \frac{1}{2z_1}\left[(2 - x_1)(z_1 + a_1 - a_3) \pm y_1\sqrt{\lambda(z_1, a_1, a_3)}\right], \tag{4.5}$$

where the Källén function is given in Eq. (3.20).

4.3 QCD corrections

4.3.1 Virtual corrections

The diagrams contributing to the virtual corrections to $O(\alpha_s)$ are shown in Fig. 4.2. They include t-quark self-energy corrections, $t\bar{t}\gamma$, $t\bar{t}Z$, and $t\bar{t}h$ vertex corrections; and $t\bar{t}\gamma h$ and $t\bar{t}Zh$ box corrections. These corrections contain both IR and UV divergences. The IR divergences in the virtual corrections and in the cross section for real-gluon emission, have been regularized by introducing an infinitesimal mass, m_g. The UV divergences arise in the self-energy and vertex contributions, while the box contributions are finite. These UV divergences have been consistently regularized in DReg and removed through the renormalization procedure. We need to renormalize the top quark mass and wave function in $\mathcal{T}^{\rm SM}_{\rm Born}$. Their bare expressions have to be substituted by the respective renormalized ones, defined in Eq. (3.26).

The virtual QCD corrections can be cast into the form

$$d\sigma^{\rm SM}_{\rm virt} = d\sigma^{\rm SM}_{\rm Born}\delta^{\rm SM}_{\rm virt}(m_g), \tag{4.6}$$

with

$$\delta^{\rm SM}_{\rm virt}(m_g) = \frac{2}{|\mathcal{T}^{\rm SM}_{\rm Born}|^2}\,{\rm Re}\left\{\mathcal{T}^{\rm SM*}_{\rm Born}\left[\left(2\delta m_t^{\rm Yuk}\frac{\partial}{\partial m_t^{\rm Yuk}}\right.\right.\right.$$

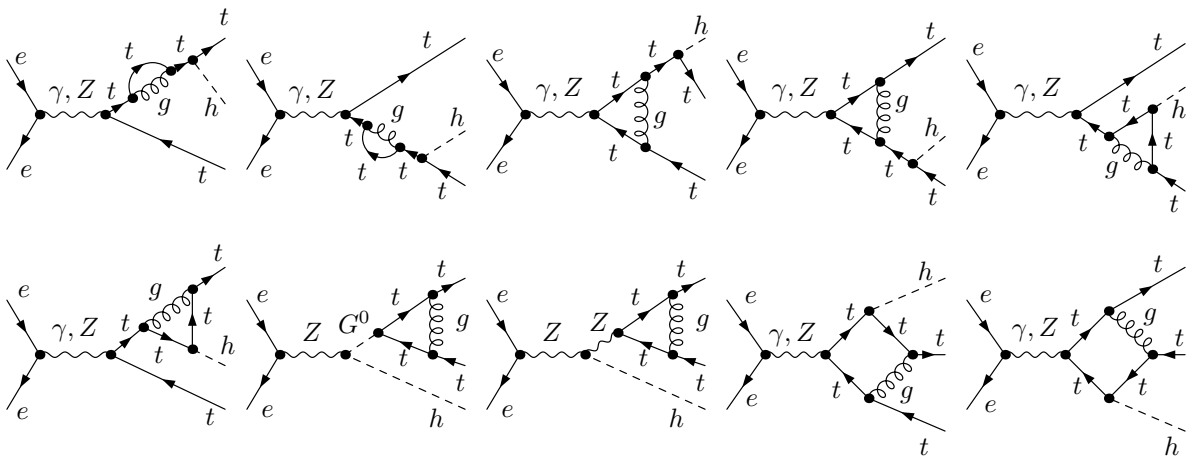

Figure 4.2: Virtual QCD corrections the process $e^+e^- \to t\bar{t}h$.

$$+2\delta m_t^{\text{prop}} \frac{\partial}{\partial m_q^{\text{prop}}} + \delta Z_t \Bigg) \mathcal{T}_{\text{Born}}^{\text{SM}} + \mathcal{T}_{\text{loop}}^{\text{SM}} \Bigg] \Bigg\}, \tag{4.7}$$

where $\mathcal{T}_{\text{loop}}^{SM}$ is the transition-matrix element corresponding to the Feynman diagrams depicted in Fig 4.2. Notice that in this case we choose to work in the OS scheme, hence we set $\delta m_t^{\text{Yuk}} = \delta m_t^{\text{prop}} = \delta m_t$, where δm_t and δZ_t are defined in Eq. (3.27). This choice is justified by observing that the logarithms arising from the counterterm for the mass in the top Yukawa coupling are of the type $\ln(m_t^2/m_h^2)$. As m_t and m_h are of the same order of magnitude, these kind of logarithms do not give rise to large corrections like the ones which we encountered in the case of the bottom Yukawa coupling.

4.3.2 Real corrections

The real QCD corrections arise from the $2 \to 4$ tree-level Feynman diagrams shown in Fig. 4.3. As mentioned before, we introduce an infinitesimal gluon mass m_g to regularize the IR divergences generated by the emission of soft gluons. Like in Sec. 3.4.2, we separate the gluon phase space into a soft and a hard region, by introducing the unphysical gluon-energy cutoff, E_{cut}. The soft- and hard-gluon contributions both depend on E_{cut}, while their sum is of course independent of it. The soft-gluon contribution is given by

$$d\sigma_{\text{soft}}^{\text{SM}} = d\sigma_{\text{Born}} \delta_{\text{soft}}^{\text{SM}}(m_g, E_{\text{cut}}), \tag{4.8}$$

where $\delta_{\text{soft}}^{\text{SM}}$ is identical to the expression in Eq. (3.33). Specifying the result of Eq. (3.34) to the case of $a_1 = a_2$ leads to

$$\delta_{\text{soft}}(m_g, E_{\text{cut}}) = \frac{\alpha_s}{\pi} C_F \left\{ \left(\frac{\alpha}{2} \frac{z_3 - 2a_1}{(\alpha^2 - 1)a_1} \ln \alpha^2 - 1 \right) \ln \frac{4E_{\text{cut}}^2}{m_g^2} \right.$$

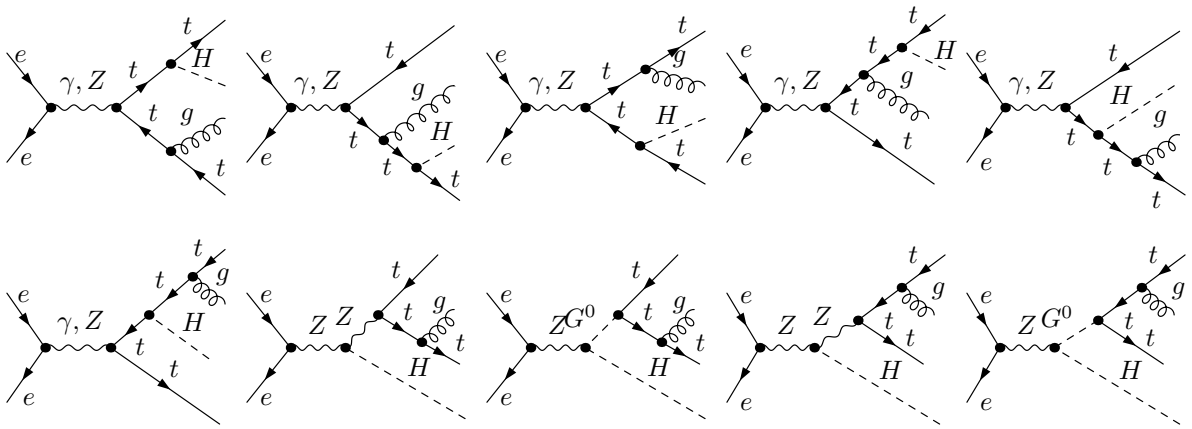

Figure 4.3: Real QCD corrections to the process $e^+e^- \to t\bar{t}h$.

$$
\begin{aligned}
&+ \alpha \frac{z_3 - 2a_1}{(\alpha^2-1)a_1} \left[\mathrm{Li}_2\left(1 - \alpha\frac{x_1+y_1}{v}\right) + \mathrm{Li}_2\left(1 - \alpha\frac{x_1-y_1}{v}\right) \right. \\
&- \mathrm{Li}_2\left(1 - \frac{x_2+y_2}{v}\right) - \mathrm{Li}_2\left(1 - \frac{x_2-y_2}{v}\right) + \frac{1}{4}\left(\ln^2\frac{x_1-y_1}{x_1+y_1} - \ln^2\frac{x_2-y_2}{x_2+y_2}\right)\Big] \\
&\left. - \frac{1}{2}\left(\frac{x_1}{y_1}\ln\frac{x_1-y_1}{x_1+y_1} + \frac{x_2}{y_2}\ln\frac{x_2-y_2}{x_2+y_2}\right)\right\}, \qquad (4.9)
\end{aligned}
$$

where

$$
\begin{aligned}
\alpha &= \frac{1}{2a_1}\left[z_3 - 2a_1 + \sqrt{z_3(z_3-4a_1)}\right], \\
v &= 2\frac{(\alpha^2-1)a_1}{\alpha x_1 - x_2}. \qquad (4.10)
\end{aligned}
$$

The hard-gluon contribution is given by

$$
d\sigma^{\mathrm{SM}}_{\mathrm{hard}}(E_{\mathrm{cut}}) = \frac{1}{2s}\frac{1}{4}|\mathcal{T}^{\mathrm{SM}}_{\mathrm{real}}|^2\theta(q^0 - E_{\mathrm{cut}})d\mathrm{PS}_4(p; p_1, p_2, p_3, q), \qquad (4.11)
$$

where $\mathcal{T}^{\mathrm{SM}}_{\mathrm{real}}$ is the transition-matrix element corresponding to the Feynman diagrams of Fig. 4.3. Eq. 4.11 has to be integrated over the full four-particle phase space, with the condition $q^0 > E_{\mathrm{cut}}$. As in the case of $e^+e^- \to t\bar{b}H^-g$ we use the `Fortran` routine `VEGAS` in order to perform the numerical integration. Finally, we can write down the expression of the QCD corrected differential cross section:

$$
d\sigma^{\mathrm{SM}}_{\mathrm{QCD}} = d\sigma^{\mathrm{SM}}_{\mathrm{Born}}[1 + \delta^{\mathrm{SM}}_{\mathrm{virt}}(m_g) + \delta^{\mathrm{SM}}_{\mathrm{soft}}(m_g, E_{\mathrm{cut}})] + d\sigma^{\mathrm{SM}}_{\mathrm{hard}}(E_{\mathrm{cut}}), \qquad (4.12)
$$

where $d\sigma^{\mathrm{SM}}_{\mathrm{Born}}$, $\delta^{\mathrm{SM}}_{\mathrm{virt}}(m_g)$, $\delta^{\mathrm{SM}}_{\mathrm{soft}}(m_g, E_{\mathrm{cut}})$, and $d\sigma^{\mathrm{SM}}_{\mathrm{hard}}(E_{\mathrm{cut}})$ are defined in Eqs. (4.3), (4.7), (4.9), and (4.11), respectively. It is manifestly independent of m_g and insensitive to the

choice of $E_{\rm cut}$, as long as $m_g \ll E_{\rm cut} \ll E_{\rm max}$. We checked this statement numerically and in Fig. 4.4, we have plotted the soft- and hard-gluon contributions, and their combination as function of $E_{\rm cut}$. One can see that the latter is constant for $E_{\rm cut} \geq 0.1$. For our numerical evaluation, we have chosen $E_{\rm cut} = 0.4$ GeV, where the soft- and hard-gluon contribution do not depend strongly on $E_{\rm cut}$. Eventually, we have extracted the IR divergences and verified their cancellation analytically. The technique used in this context has in Sec. 3.4.3.

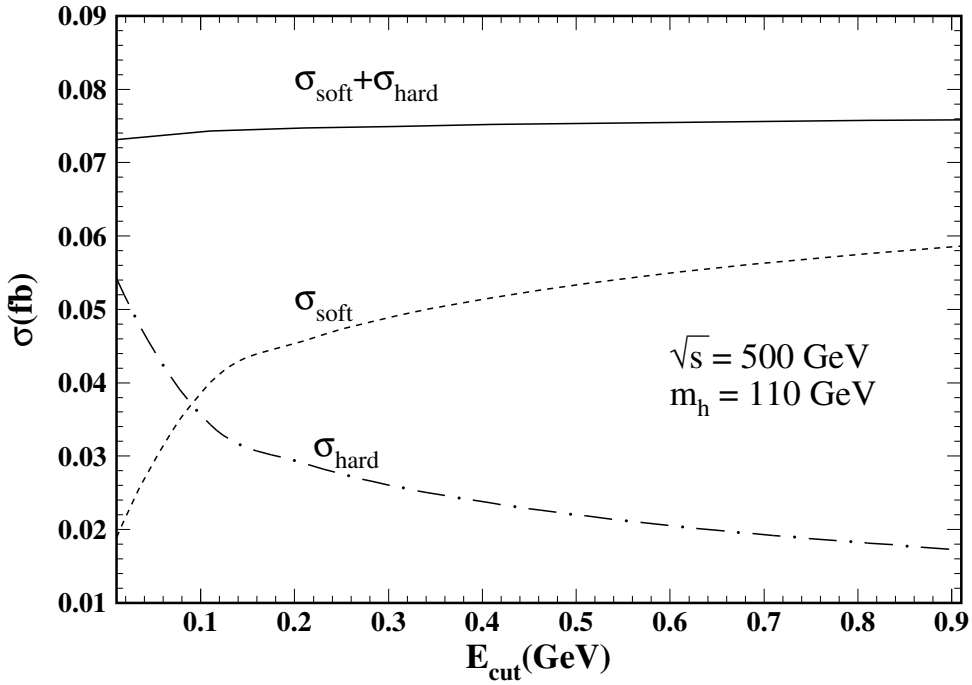

Figure 4.4: Soft- and hard-gluon contributions to the total cross section of $e^+e^- \to t\bar{t}hg$ as a function of the gluon-energy cut-off $E_{\rm cut}$ for $\sqrt{s} = 500$ GeV and $m_h = 110$ GeV.

The results for the QCD-corrected total cross section agree numerically with [23, 24] both for the special case of a virtual photon exchange and for the case when the contributions from the Z boson are included. This provides us with a further check of the parameterization of the four-particle phase space given in Appendix C.

4.4 Numerical results

In this section, we present our numerical result for the QCD-corrected total cross section for the process $e^+e^- \to t\bar{t}h$. Our input parameters are the same as in Sec. 3.6, except

for the choice of the α_s value. As we have used the OS renormalization scheme, the only dependence on the scale μ which arises in the results is given by the dependence of $\alpha_s^{(6)}(\mu)$. We have set $\alpha_s = \alpha_s^{(6)}(\sqrt{s})$, while the results for other choices of α_s can be easily obtained from ours just by rescaling its value in the virtual and real corrections.

We have investigated the dependence on m_h of the LO and NLO cross section, for the c.m. energies $\sqrt{s} = 500$ GeV and $\sqrt{s} = 800$ GeV. Note that the size of the QCD corrections is large at modest energies and becomes smaller if the energy is increased. This behaviour is due to the rescattering diagrams, where the gluon is exchanged between the final state top quarks. Close to the $t\bar{t}$ threshold this leads to Coulomb-like singularities which were discussed in detail in Ref. [23]. At high energies these rescattering corrections become less important and the negative $t\bar{t}h$-vertex corrections are dominant in comparison with the positive gluon emission contributions [23, 75]). In Fig. 4.5, we varied m_h from 110 to 140 GeV, where the cross section becomes quite small because of the phase-space suppression. We can see that the QCD corrections are positive and indeed very large.

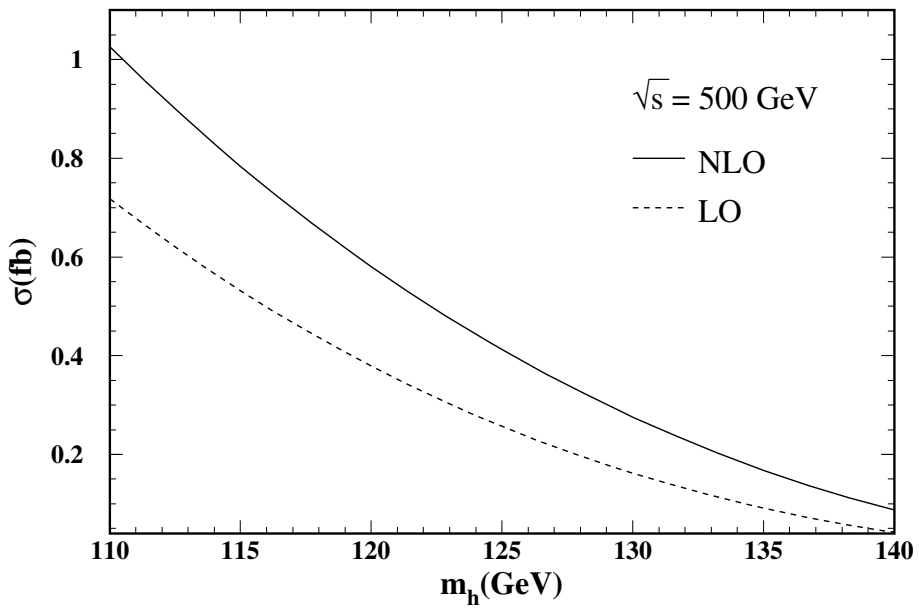

Figure 4.5: Total cross section of $e^+e^- \to t\bar{t}h$ without (dotted curves) and with (solid curves) QCD corrections in the OS scheme as a function of m_h for $\sqrt{s} = 500$ GeV.

They increase the LO cross section by about 43% for $m_h = 110$ GeV and by 106% for $m_h = 140$ GeV. For $m_h = 120$ GeV, the NLO cross section amounts to about 0.55 fb. With the luminosity of $3.4 \times 10^{34}\text{cm}^{-2}\text{s}^{-1}$ planned for TESLA [7] this means around 187 events

per year. In Fig. 4.6, we present the results for the total cross section for $\sqrt{s} = 800$ GeV as a function of the Higgs boson mass, which we vary between 110 GeV and 200 GeV. In

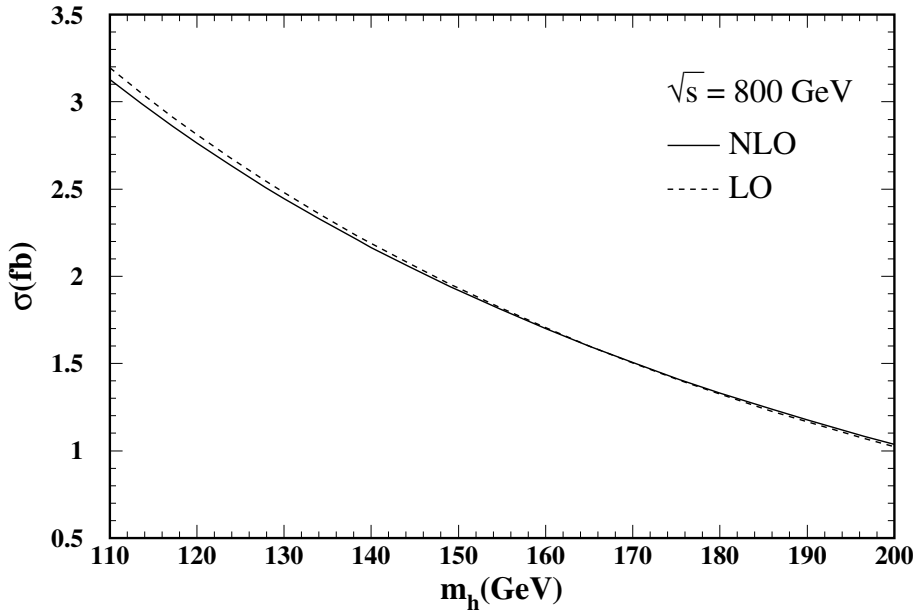

Figure 4.6: Same as in Fig. 4.5, for $\sqrt{s} = 800$ GeV.

this case, the corrections are very small and are both negative and positive. They reduce the LO cross section by 2% for $m_h = 110$ GeV and increase it by 1.4% for $m_h = 110$ GeV. For $m_h = 120$ GeV the NLO cross section amounts to about 2.7 fb, which corresponds to around 1570 events per year.

Finally, for the typical Higgs boson mass value $m_h = 120$ GeV, we have studied the dependence of the cross section on the c.m. energy. The results are plotted in Fig. 4.7, where we varied the c.m. energy from $\sqrt{s} = 500$ GeV to $\sqrt{s} = 2$ TeV. We observe that the cross section is maximal around $\sqrt{s} = 800$ GeV where it amounts to about 2.7 fb and decrease slowly to 0.72 fb for $\sqrt{s} = 2$ TeV. The corrections are minimal about $\sqrt{s} = 700$ GeV. For $\sqrt{s} = 800$ GeV, they reduce the Born cross section by -1.7%, while they become larger for higher energy scales and amount to about -20% for $\sqrt{s} = 2$ TeV.

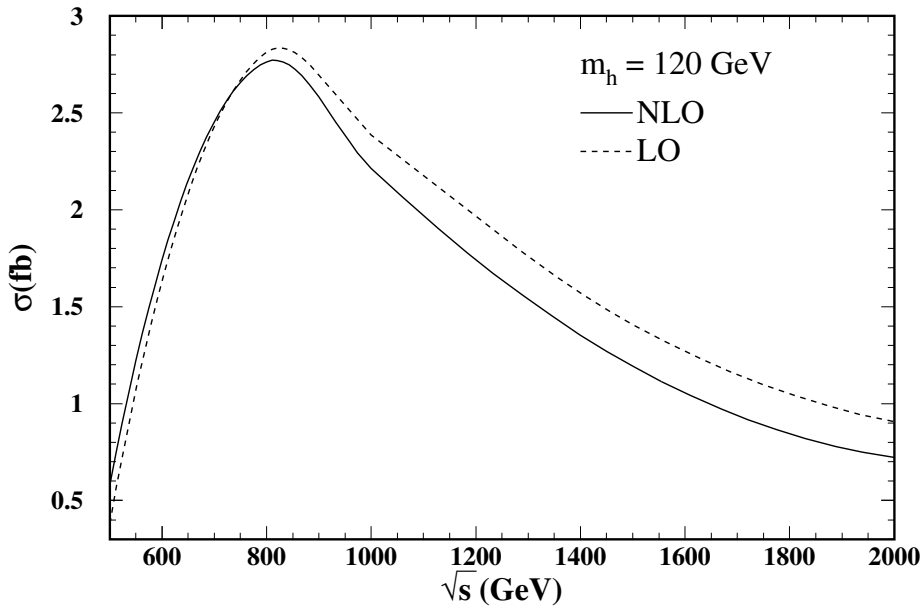

Figure 4.7: Total cross section of $e^+e^- \to t\bar{t}h$ without (dotted curves) and with (solid curves) QCD corrections in the OS scheme as a function of $\sqrt{s}$ for $m_h = 120$ GeV.

Chapter 5

Higgs Boson production with polarized beams

5.1 Introduction

In this chapter, we generalize the results of the previous sections to the case of polarized electron and positron beams. In Sec. 5.2, we briefly review the technical issues concerning the electron and positron polarization at a e^+e^- linear collider based on studies presented in Refs. [7] and [76]. Indeed, polarization of both beams at the next linear colliders is a realistic possibility. In Sec. 5.3, we give the expression of the polarized lepton tensor, which generalizes the formula given in Eq. (3.6). The numerical analysis is presented for $e^+e^- \to t\bar{b}H^-$ and for $e^+e^- \to t\bar{t}h$ in Secs. 5.4 and 5.5, respectively. We first investigate the role of the beam polarization at Born level. We discuss the differences arising in the expressions for the Born cross section in the unpolarized and 100% polarized cases. Special emphasis is put in studying the behaviour of the individual contributions arising from the diagrams with a the virtual photon, a virtual Z boson, and their interference terms. Eventually, the results for the polarized NLO cross section are presented for both considered processes for a realistic choice of the polarization.

5.2 Beam polarization

At SLC at SLAC, highly polarized electron beams with the help of a strained lattice GaAs photo-cathode have already been achieved [77]. Thus, there is good reason to expect that electron polarization $\mathcal{P}_{e^-}$ in excess of 80% together with polarimetry at the $< 0.5\%$ will be possible at future linear colliders.

For the positron, it is intrinsically harder to achieve polarization. A fundamental difference is that the production of each positron requires $10 - 100$ MeV photons, rather than the few eV photons per electron at an electron photo-cathode. Nevertheless, methods for achieving $40 - 60\%$ positron polarization $\mathcal{P}_{e^+}$ have been proposed and are currently under development. Positron polarizations of $40 - 45\%$ should be possible with no loss of luminosity. Higher polarization could be achieved at the price of reduced intensity (e.g. $\mathcal{P}_{e^+} = 60\%$ at $\simeq 55\%$ of full intensity [78]). In our analysis, we will assume the experimentally realistic polarizations $\mathcal{P}_{e^-} = 80\%$ for the electron beam and $\mathcal{P}_{e^+} = 45\%$ for the positron beam.

5.3 Polarized lepton tensor

In the following, we will use the same notation as in Sec. 3.2. First, we consider the expression for the lepton tensor for polarized incoming particles, which generalizes Eq. (3.3):

$$L^{\mu\nu}_{\rm pol} = \mathrm{tr}\left[\bar{v}(k_2,\lambda_2)\ \not{k}_1\gamma^\nu\left(v'_e - a'_e\gamma_5\right)u(k_1,\lambda_1)\bar{u}(k_1,\lambda_1)\ \not{k}_2\gamma^\mu(v_e - a_e\gamma_5)v(k_2,\lambda_2)\right]. \quad (5.1)$$

In this case, we do not sum over the spins and we instead use the following relations[1]

$$\begin{aligned} u(k_1,\lambda_1)\bar{u}(k_1,\lambda_1) &= \frac{1}{2}\left(1 + \lambda_1\gamma_5\right)\ \not{k}_1, \\ v(k_2,\lambda_2)\bar{v}(k_2,\lambda_2) &= \frac{1}{2}\left(1 - \lambda_2\gamma_5\right)\ \not{k}_2. \end{aligned} \quad (5.4)$$

Hence, we have

$$\begin{aligned} L^{\mu\nu}_{\rm pol} \;=\; & \Big[\left(v_e v'_e + a_e a'_e\right)\left(1 - \lambda_1\lambda_2\right) + \left(v_e a'_e + v'_e a_e\right)\left(\lambda_2 - \lambda_1\right)\Big]\{k_1 k_2\}^{\mu\nu} \\ & + i\Big[\left(v_e a'_e + a_e v'_e\right)\left(1 - \lambda_1\lambda_2\right) + \left(v_e v'_e + a_e a'_e\right)\left(\lambda_2 - \lambda_1\right)\Big]\epsilon^{\mu\nu\alpha\beta}k_{1\alpha}k_{2\beta}, \end{aligned} \quad (5.5)$$

[1]Here, we have assumed that leptons in the initial state are massless. In general, for massive fermions we have the relation

$$\{u(k,\lambda)\bar{u}(k,\lambda), v(k,\lambda)\bar{v}(k,\lambda)\} = \frac{1}{2}\left(1 + \lambda\gamma_5\ \not{s}\right)\left(\not{k} \pm m\right), \quad (5.2)$$

where s is the unit vector in the direction of the spin axis in the particle's rest frame, boosted in the c.o.m. frame. It is identical to the longitudinal polarization vector of a vector boson, and fulfills $s \cdot k = 0$ and $s^2 = -1$. In the ultrarelativistic limit, $k^0 \gg m$, the vector s becomes increasingly parallel to k, i.e. $s \sim k/m$, hence

$$\left(1 + \lambda\gamma_5\ \not{s}\right)\left(\not{k} \pm m\right) \sim \left(1 + \lambda\gamma_5\frac{\not{k}}{m}\right)\left(\not{k} \pm m\right) = \left(1 \pm \lambda\gamma_5\right)\ \not{k}. \quad (5.3)$$

where $\{k_1 k_2\}^{\mu\nu} = k_1^\mu k_2^\nu + k_1^\nu k_2^\mu - k_1 \cdot k_2 g^{\mu\nu}$. Similarly as in Sec. 3.2, for Lorentz invariance, we can write the integral of $L^{\mu\nu}_{\rm pol}$ as a linear combination of $g^{\mu\nu}$ and the momenta $p^\mu p^\nu$ as follows

$$\int \frac{d\Omega}{4\pi} L^{\mu\nu}_{\rm pol} = A g^{\mu\nu} + B p^\mu p^\nu. \tag{5.6}$$

Contracting the last expression with $g^{\mu\nu}$ and $p^\mu p^\nu$, respectively, one finds the solution for the coefficients A and B, and the lepton tensor reads

$$\int \frac{d\Omega}{4\pi} L^{\mu\nu}_{\rm pol} = \frac{1}{3}\Big[\left(v_e v'_e + a_e a'_e\right)\left(1 - \lambda_1\lambda_2\right) + \left(v_e a'_e + v'_e a_e\right)\left(\lambda_2 - \lambda_1\right)\Big](p^\mu p^\nu - s g^{\mu\nu}). \tag{5.7}$$

After summing over $\lambda_{1,2} = \pm 1$ one obtains the expression of Eq. (3.9) for the unpolarized case.

If we define $\sigma^{\lambda_1\lambda_2}$ as the cross section of the process with the electron and positron having helicity λ_1 and λ_2, respectively, we have that $\sigma^{++} = \sigma^{--} = 0$, which follows from angular momentum conservation. Thus, the result for the cross section will be a linear combination of σ^{+-} and σ^{-+}. Denoting with f_{e^-} (f_{e^+}) the percentage of positively polarized electrons (positrons), this combination reads

$$\sigma^{\rm pol} = f_{e^-}\left(1 - f_{e^+}\right)\sigma^{+-} + \left(1 - f_{e^-}\right) f_{e^+}\sigma^{-+}. \tag{5.8}$$

For example, a 80% positively polarized electron beam will contain 90% of electrons positively polarized and 10% negatively polarized, and we will have $f_{e^-} = 0.9$. Analogously, a 45% negatively polarized positron beam means $f_{e^+} = 0.275$. In general, knowing the results for σ^{+-} and σ^{-+}, one can recover the unpolarized result, which is given by:

$$\sigma^{\rm unpol} = \frac{1}{4}\left(\sigma^{+-} + \sigma^{-+}\right). \tag{5.9}$$

We now turn to the process $e^+e^- \to t\bar{b}H^-$. From the expression of the polarized lepton tensor given in Eq. (5.7), we can obtain the 100% polarized differential cross sections. They read

$$\begin{aligned}
\frac{d\sigma^{+-}_{\rm Born}}{dx_1\, dx_2} &= \frac{G_F^3 m_Z^4}{16\pi^3\sqrt{2}}\Big[\mathcal{Q}_e^2 f_{\gamma\gamma}(x_1,x_2) + \\
&\quad + \mathcal{Q}_e\left(\mathcal{V}_e - \mathcal{A}_e\right) f_{\gamma Z}(x_1,x_2) + \left(\mathcal{V}_e - \mathcal{A}_e\right)^2 f_{ZZ}(x_1,x_2)\Big], \\
\frac{d\sigma^{-+}_{\rm Born}}{dx_1\, dx_2} &= \frac{G_F^3 m_Z^4}{16\pi^3\sqrt{2}}\Big[\mathcal{Q}_e^2 f_{\gamma\gamma}(x_1,x_2) + \\
&\quad + \mathcal{Q}_e\left(\mathcal{V}_e + \mathcal{A}_e\right) f_{\gamma Z}(x_1,x_2) + \left(\mathcal{V}_e + \mathcal{A}_e\right)^2 f_{ZZ}(x_1,x_2)\Big],
\end{aligned} \tag{5.10}$$

where $\mathcal{Q}_e$, $\mathcal{V}_e$, and $\mathcal{A}_e$ are defined in Eq. (3.17), while the form factors $f_{\gamma\gamma}(x_1,x_2)$, $f_{\gamma Z}(x_1,x_2)$, and $f_{ZZ}(x_1,x_2)$ are listed in Appendix B. Inserting the expressions of Eq. (5.10) in

Eq. (5.9), leads to the unpolarized differential cross section of Eq. (3.16). For practical convenience, we summarize in Tab. 5.1, the coefficients of the form factors for the unpolarized and totally polarized cross sections. We denote by $\sigma_{\gamma\gamma}, \sigma_{ZZ}$, and $\sigma_{\gamma Z}$, the contributions to the cross section arising from the diagrams with a virtual photon, with a virtual Z boson, and their interference terms, respectively. The expressions for $\sigma^{\text{unpol}}_{\text{Born}}$, $\sigma^{+-}_{\text{Born}}$, and $\sigma^{-+}_{\text{Born}}$ are obtained integrating Eq. (3.16) and Eq. (5.10) over the variables x_1 and x_2, respectively. The integration boundaries can be found in Eq. (3.18). In Tab. 5.1, we have introduced integrated form factors, in order to make the formulae compact. The corresponding quantities are denoted by a hat and defined by

$$\hat{f}_{VV'} = \frac{G_F^3 m_Z^4}{32\pi^3\sqrt{2}} \int \mathrm{d}x_1 \mathrm{d}x_2 \; f_{VV'}(x_1, x_2), \tag{5.11}$$

where $V, V' = \gamma, Z$. The variables x_1 and x_2 are integrated over the intervals given in Eq. (3.18).

Cross section	$\sigma_{\gamma\gamma}$	σ_{ZZ}	$\sigma_{\gamma Z}$
σ^{unpol}	$\mathcal{Q}_e^2 \hat{f}_{\gamma\gamma}$	$(\mathcal{V}_e^2 + \mathcal{A}_e^2)\, \hat{f}_{ZZ}$	$\mathcal{Q}_e \mathcal{V}_e \hat{f}_{\gamma Z}$
σ^{+-}	$2\mathcal{Q}_e^2 \hat{f}_{\gamma\gamma}$	$2\,(\mathcal{V}_e - \mathcal{A}_e)^2\, \hat{f}_{ZZ}$	$2\mathcal{Q}_e\,(\mathcal{V}_e - \mathcal{A}_e)\, \hat{f}_{\gamma Z}$
σ^{-+}	$2\mathcal{Q}_e^2 \hat{f}_{\gamma\gamma}$	$2\,(\mathcal{V}_e + \mathcal{A}_e)^2\, \hat{f}_{ZZ}$	$2\mathcal{Q}_e\,(\mathcal{V}_e + \mathcal{A}_e)\, \hat{f}_{\gamma Z}$

Table 5.1: Coefficient of the integrated form factors for different choices of polarization

The analogous results for the process $e^+e^- \to t\bar{t}h$ can be obtain by substituting the quantities $f_{VV'}$ with the corresponding form factors $g_{VV'}$ defined in Eq. (4.3).

5.4 Polarized cross section for $e^+e^- \to t\bar{b}H^-$

We will use the input parameters listed in Sec. 3.6 and subdivide this section in two parts. In subsection 5.4.1, we investigate the LO results for the totally polarized cross sections and we compare them with the results for the unpolarized cross section. Our aim is to determine the best choice for the polarization, in order to obtain larger values for the cross sections. In subsection 5.4.2, we present the results for the NLO cross section in

the experimentally more realistic situation of a 80% polarized electron beam and a 45% polarized positron beam.

5.4.1 Polarized Born cross section for $e^+e^- \to t\bar{b}H^-$

Let us compare the results for the unpolarized cross sections[2] $\sigma^{\rm unpol}$, σ^{+-}, and σ^{-+} defined in Eqs. (3.16) and (5.10). In Figs. 5.1, 5.2, and 5.3, we investigate their dependence on m_H for $\sqrt{s} = 500$ GeV and $\tan\beta = 2, 6$ and 40, respectively. In Fig. 5.1, we can

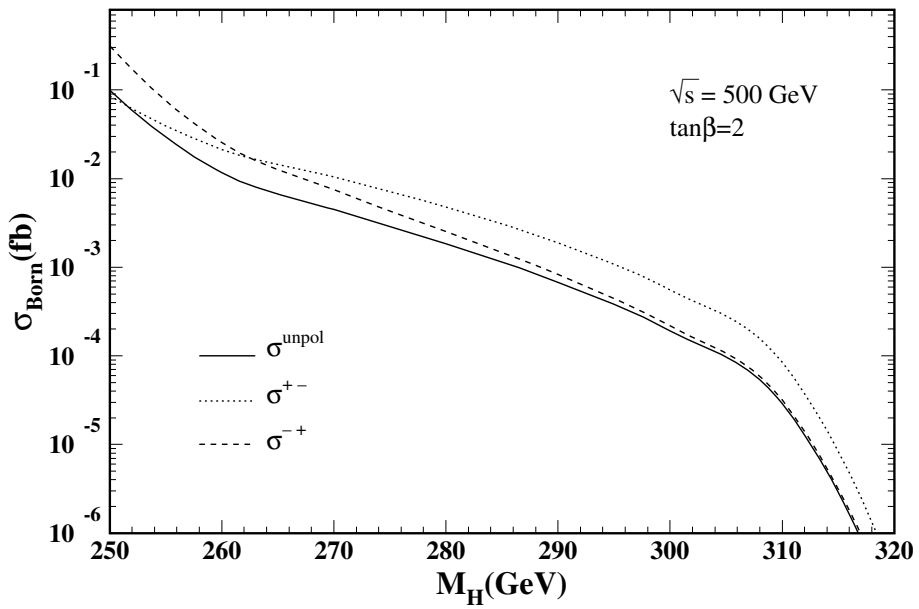

Figure 5.1: Polarized and unpolarized LO cross section for $e^+e^- \to t\bar{b}H^-, \bar{t}bH^+$ as a function of m_H for $\sqrt{s} = 500$ GeV and $\tan\beta = 2$.

see that σ^{+-} and σ^{-+} are always larger than $\sigma^{\rm unpol}$, except for $m_H < 252$ GeV where σ^{+-} is slightly smaller than $\sigma^{\rm unpol}$. Moreover, we observe that the plots for σ^{+-} and σ^{-+} intersect close to $m_H = 262$ GeV and σ^{-+} (σ^{+-}) is the best choice for the polarization for $250 \leq m_H \leq 262$ GeV ($m_H > 262$ GeV). In Fig. 5.2, the dominant contribution is given by σ^{-+} for all Higgs masses considered and represents the best polarization. The plots corresponding to σ^{+-} and $\sigma^{\rm unpol}$ intersect for $m_H = 253$ GeV and thus for $m_H > 253$ GeV, σ^{+-} is larger than $\sigma^{\rm unpol}$. In Fig. 5.3, σ^{-+} is always much larger that $\sigma^{\rm unpol}$, increasing

[2]In this subsection, in order to simplify the notation, we have omitted subscript Born.

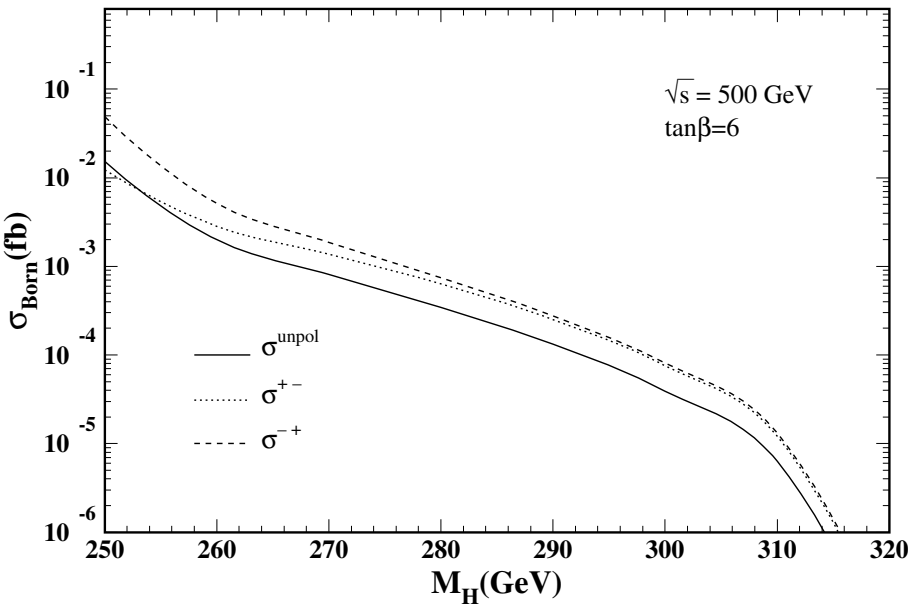

Figure 5.2: Same as in Fig. 5.1 for $\tan\beta = 6$.

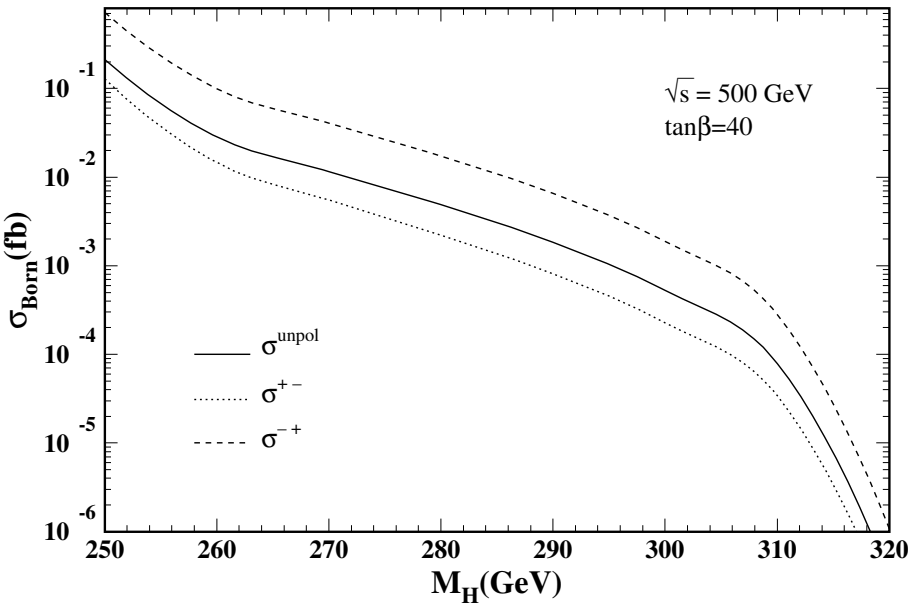

Figure 5.3: Same as in Fig. 5.1 for $\tan\beta = 40$.

its values up to three times. The plot for σ^{+-}, instead lies below the unpolarized one for all considered m_H values.

We have studied the m_H dependence for $\sqrt{s} = 800$ GeV and $\tan\beta = 2, 6$ and 40 as well, and we found an analogous behaviour as for $\sqrt{s} = 500$ GeV. We observe that for both energies σ^{+-}, which is almost dominant for $\tan\beta = 2$ becomes much smaller than $\sigma^{\rm unpol}$ for $\tan\beta = 40$. The opposite happens to σ^{-+}, which acquires importance going from $\tan\beta = 2$ to $\tan\beta = 40$. This is essentially due to two reasons. The first reason is to be ascribed to the different numerical values of the weights of teh integrated form factors $\hat{f}_{VV'}$ which change considerably when passing from the unpolarized to the polarized case (see Tab. 5.1). This is summarized in Tab. 5.2. Hence, for different values

Polarization		Coefficients	$\sqrt{s} = 500$ GeV
$\sigma^{\rm unpol}$	$\gamma\gamma$	$\mathcal{Q}_e^2$	0.6914
	ZZ	$(\mathcal{V}_e^2 + \mathcal{A}_e^2)$	0.2708
	γZ	$\mathcal{Q}_e \mathcal{V}_e$	-0.0477
σ^{+-}	$\gamma\gamma$	$2\mathcal{Q}_e^2$	1.3828
	ZZ	$2\left(\mathcal{V}_e - \mathcal{A}_e\right)^2$	0.4228
	γZ	$2\mathcal{Q}_e\left(\mathcal{V}_e - \mathcal{A}_e\right)$	0.7646
σ^{-+}	$\gamma\gamma$	$2\mathcal{Q}_e^2$	1.3828
	ZZ	$2\left(\mathcal{V}_e + \mathcal{A}_e\right)^2$	0.6603
	γZ	$2\mathcal{Q}_e\left(\mathcal{V}_e + \mathcal{A}_e\right)$	-0.9556

Table 5.2: Prefactors of the quantities $\hat{f}_{VV'}$ for different choices of polarization. The definition of $\mathcal{Q}_e$, $\mathcal{V}_e$ and $\mathcal{A}_e$ can be found in Eq. (3.17). The dependence on $\sqrt{s}$ for $\sqrt{s} \gg m_Z$ is marginal.

of the polarization the form factors turn out to be differently weighed. This explains why for the same value of $\tan\beta$ the plots for $\sigma^{\rm unpol}$, σ^{+-} and σ^{-+} can intersect.

The second reason is related to the numerical values of the integrated form factors $\hat{f}_{\gamma\gamma}, \hat{f}_{ZZ}$ and $\hat{f}_{\gamma Z}$. In Tab. 5.3, we list these values for $\sqrt{s} = 500$ GeV, $m_H = 280$ GeV, $\tan\beta = 2$, and $\tan\beta = 40$. Finally, in Tab 5.4, we have listed the numerical values of $\sigma_{\gamma\gamma}$, σ_{ZZ} and $\sigma_{\gamma Z}$ for different choices of the polarization [3]. From this table, we can see that for the unpolarized cross section the dominant contribution arises from $\sigma_{\gamma\gamma}$, while this is no longer true for σ^{+-} and σ^{-+}. For these polarizations, the contributions arising from

[3]The values of the tables and Figs. 5.4, 5.5, and 5.6 refer only to $e^+e^- \to t\bar{b}H^-$, whereas in all other figures the cross section for $e^+e^- \to t\bar{b}H^-, \bar{t}bH^+$ is shown.

Integrated form factors ($\times 10^{-3}$fb)	$\tan\beta = 2$	$\tan\beta = 40$
$\hat{f}_{\gamma\gamma}$	1.2503	2.5463
$\hat{f}_{ZZ}$	0.3121	1.8159
$\hat{f}_{\gamma Z}$	0.6956	-4.1549

Table 5.3: Integrated form factors for different choices of polarization for $\sqrt{s} = 500$ GeV and $m_H = 280$ GeV expressed in 10^{-3}fb).

σ_{ZZ} and in particular those of $\sigma_{\gamma Z}$ become essential. Moreover, we observe that $\sigma_{\gamma Z}$ can be of both signs, depending on the choice of the polarization and $\tan\beta$. This explains why for different values of $\tan\beta$ different choices of polarizations lead to larger results for the cross section. These observations can be visualized in Figs. 5.4, 5.5, and 5.6, where we have plotted the contributions $\sigma_{\gamma\gamma}$, σ_{ZZ}, $\sigma_{\gamma Z}$, and their sum $\sigma_{\rm tot}$, as function of $\tan\beta$ for unpolarized beams, 100% $e^-\uparrow$ 100% $e^+\downarrow$, and 100% $e^-\downarrow$ 100% $e^+\uparrow$, respectively. In these figures, we have chosen the same values of the coordinates in order to facilitate the comparison between the results for different polarizations.

We can conclude that for $\tan\beta = 2$, both polarizations are needed, to obtain a larger cross section, while incrementing $\tan\beta$, the best choice for the polarization is given by a negatively polarized electron beam and a positively polarized positron beam.

Cross section	$\sigma_{\gamma\gamma}$	σ_{ZZ}	$\sigma_{\gamma Z}$	$\sigma_{\rm tot}$
$\underline{\tan\beta = 2}$				
$\sigma^{\rm unpol}$	0.8645	0.0845	-0.0332	0.9158
σ^{+-}	1.7289	0.1319	0.5319	2.3929
σ^{-+}	1.7289	0.2061	-0.6647	1.2703
$\underline{\tan\beta = 40}$				
$\sigma^{\rm unpol}$	1.7605	0.4917	0.1983	2.4506
σ^{+-}	3.5211	0.7678	-3.1771	1.1118
σ^{-+}	3.5211	1.1992	3.9704	8.6907

Table 5.4: Numerical values of the contributions $\sigma_{\gamma\gamma}$, σ_{ZZ}, and $\sigma_{\gamma Z}$ to the total cross section as a function of the choice of polarization for $\sqrt{s} = 500$ GeV and $m_H = 280$ GeV. The symbol $\sigma_{\rm tot}$ represents the sum of these contributions. All the results are given in 10^{-3}fb).

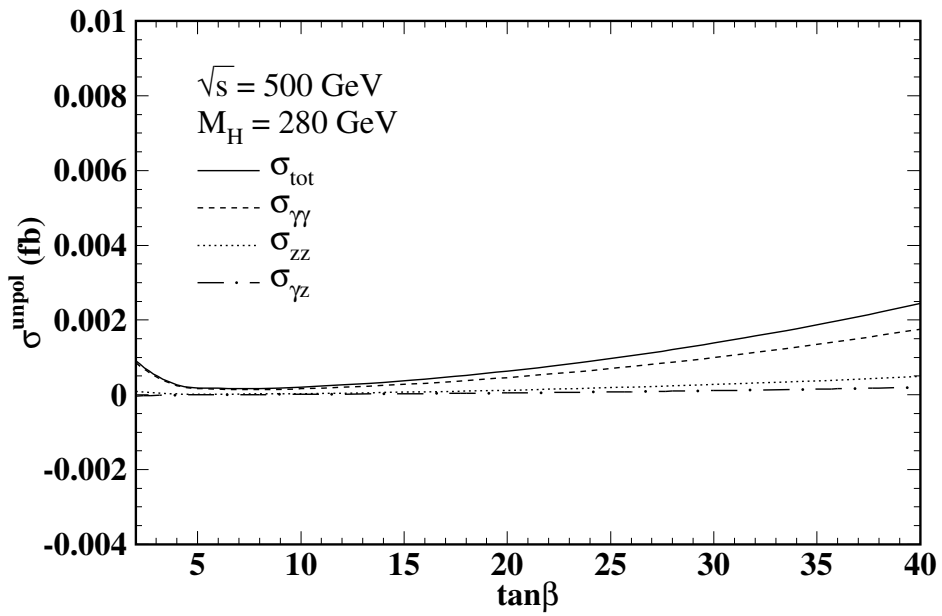

Figure 5.4: The contributions $\sigma_{\gamma\gamma}$, σ_{ZZ}, $\sigma_{\gamma Z}$, and their sum $\sigma_{\rm tot}$ as a function of $\tan\beta$ for $\sqrt{s} = 500$ GeV, $m_H = 280$ GeV, and unpolarized beams. The curves refer only to the process $e^+e^- \to t\bar{b}H^-$.

As a consequence of this analysis, we can conclude that $\sigma_{\gamma\gamma}$ represents the main contribution to the cross section only in the unpolarized case, whereas the introduction of polarization makes σ_{ZZ} and in particular the interference term $\sigma_{\gamma Z}$ very important.

5.4.2 Polarized QCD- and SUSY QCD-corrected cross section for $e^+e^- \to t\bar{b}H^-$

In the previous subsection, we have studied the impact of polarization on the Born cross section. To this aim, we have investigated the results for 100% polarized beams. However, as already discussed in Sec. 5.2, this choice of the polarization is not accessible. In practice at most an 80% polarized electron beam and and a 45% polarized positron beam, can be achieved. Therefore, in this subsection, we will present the QCD- and SUSY QCD-corrected results for this choice of polarization. Again, we plotted the dependence of the LO and NLO results for c.m. energies $\sqrt{s} = 500$ and 800 GeV as functions of m_H for different values of $\tan\beta$. For $\tan\beta = 2$, the NLO results include only the QCD corrections, because, as we saw in Sec. 3.6, the SUSY parameters do not satisfy the experimental limits

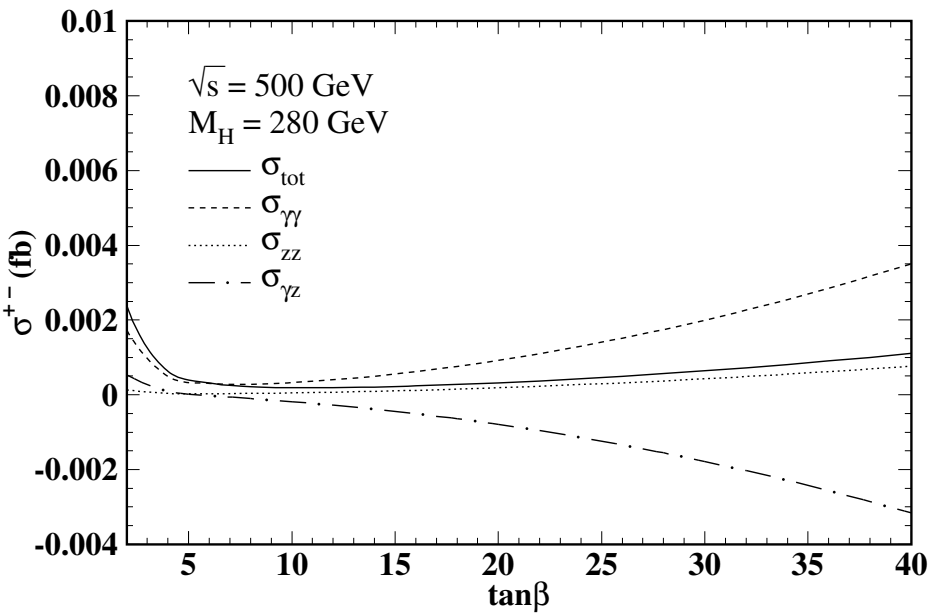

Figure 5.5: The contributions $\sigma_{\gamma\gamma}$, σ_{ZZ}, $\sigma_{\gamma Z}$, and their sum $\sigma_{\rm tot}$ for unpolarized beams as a function of $\tan\beta$ for $\sqrt{s} = 500$ GeV and $m_H = 280$ GeV for the polarization 100% $e^-\uparrow$ 100% $e^+\downarrow$. The curves refer only to the process $e^+e^- \to t\bar{b}H^-$.

for this choice of $\tan\beta$. In the following, we denote with an upward (downward) arrow $\uparrow$ ($\downarrow$) the positive (negative) polarization. In Fig. 5.7, we see that for $m_H < 292$ GeV, the polarization leading to a larger cross section is with 80% $e^-\downarrow$ and 45% $e^+\uparrow$, while for the larger values of m_H, the cross section with the the opposite combination of the polarization, namely 80% $e^-\uparrow$ and 45% $e^+\downarrow$, becomes important. With this choice, the cross section can be increased up to almost 120%. Setting a minimum of 10 events for the process to be observed, we find that for the unpolarized case only the region of $m_H < 256$ GeV can be reached by the experiments, while for the polarized case the upper limit is shifted to $m_H < 260$ GeV, assuming the design luminosity $\mathrm{L} = 3.4 \times 10^{34}\mathrm{cm}^{-2}\mathrm{s}^{-1}$. Nevertheless, for the same value of m_H the number of events is more than two times larger than without beam polarization. In Fig. 5.8, we have chosen $\tan\beta = 6$. We see that the polarization yielding the largest cross section is with 80% $e^-\downarrow$ and 45% $e^+\uparrow$. With this choice, the cross section can be increased up to about 115%. However, except for $m_H = 250$ GeV, the cross section is too small to be observed. In Fig. 5.9, we have chosen $\tan\beta = 40$. We see that with the polarization 80% $e^-\downarrow$ and 45% $e^+\uparrow$, the cross section can be increased up to about 118%, shifting the 10 events limit from 260 GeV to

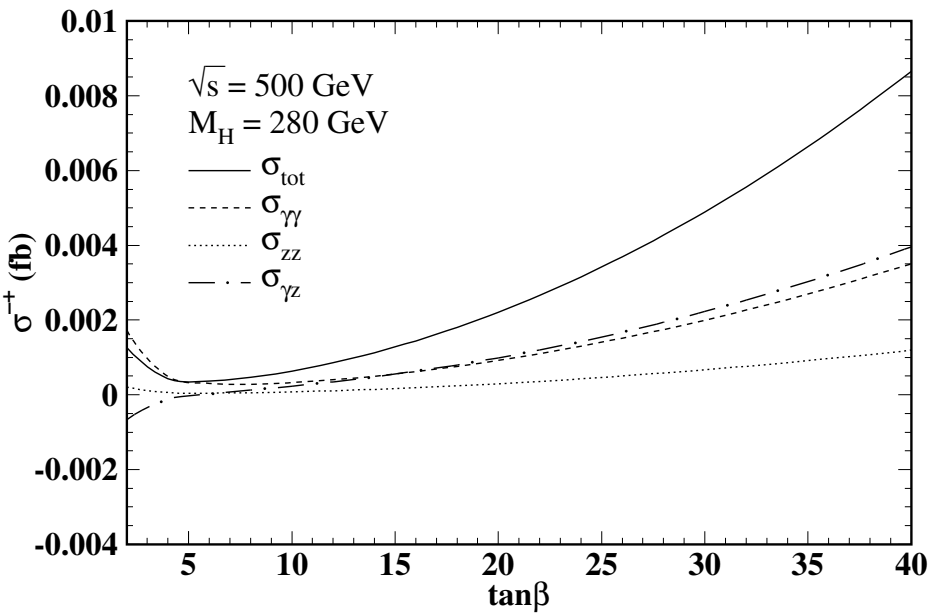

Figure 5.6: Same as in Fig. 5.5 for the polarization 100% $e^-\downarrow$ 100% $e^+\uparrow$. The curves refer only to the process $e^+e^- \to t\bar{b}H^-$.

268 GeV. Let us now turn to the plots for $\sqrt{s} = 800$ GeV. In Fig. 5.10, where $\tan\beta = 2$, the best polarization is with 80% $e^-\downarrow$ and 45% $e^+\uparrow$ for $m_h < 535$ GeV, while for the other values of m_H, the best option is 80% $e^-\uparrow$ and 45% $e^+\downarrow$. The polarized cross section is more than 2 times larger than the unpolarized one. In Fig. 5.11, we have $\tan\beta = 6$. We see that the best polarization is with 80% $e^-\downarrow$ and 45% $e^+\uparrow$ for $m_h < 550$ GeV, while for $m_h > 550$ GeV, the other polarization yields larger results. The cross section can be increased up to about 115%. However, except for $m_H = 400$ GeV, the cross section is too small to be observed. In Fig. 5.12, we have chosen $\tan\beta = 40$. We see that the plots corresponding to the NLO results for the polarizations 80% $e^-\downarrow$ and 45% $e^+\uparrow$ and 80% $e^-\uparrow$ and 45% $e^+\downarrow$ intersect in two point for $m_H = 435$ GeV and for $m_H = 455$ GeV. For $m_H < 435$ GeV and $m_H > 455$ GeV, the most suitable polarization is 80% $e^-\downarrow$ and 45% $e^+\uparrow$, while for $435 < m_H < 455$ GeV, the other one is to be preferred. This is because the NLO corrections are large and negative for the first polarization choice, and positive for the second one. With the help of polarization, the cross section can be increased by up to 112% for $m_H = 400$, where it amounts to almost 0.65 fb, corresponding to 375 events for the designed luminosity of TESLA.

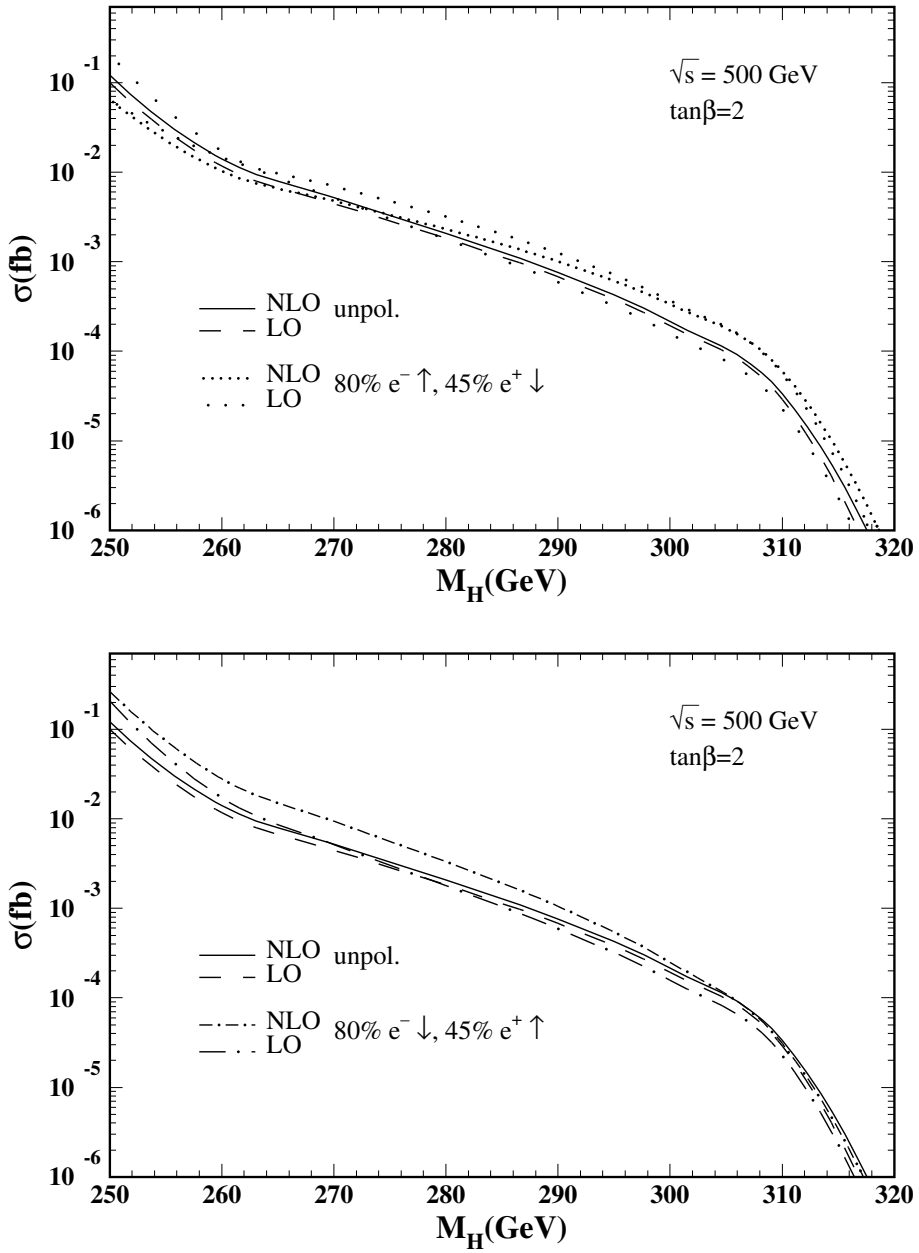

Figure 5.7: Study of the polarization for LO and NLO QCD-corrected cross section for $e^+e^- \to t\bar{b}H^-, \bar{t}bH^+$ as a function of m_H, for $\sqrt{s} = 500$ GeV and $\tan\beta = 2$.

5.5 Polarized cross section for $e^+e^- \to t\bar{t}h$

In this section, we discuss the influence of polarization for the process $e^+e^- \to t\bar{t}h$. We first study the impact of the polarization on the integrated Born form factors $\hat{g}_{VV'}$, which

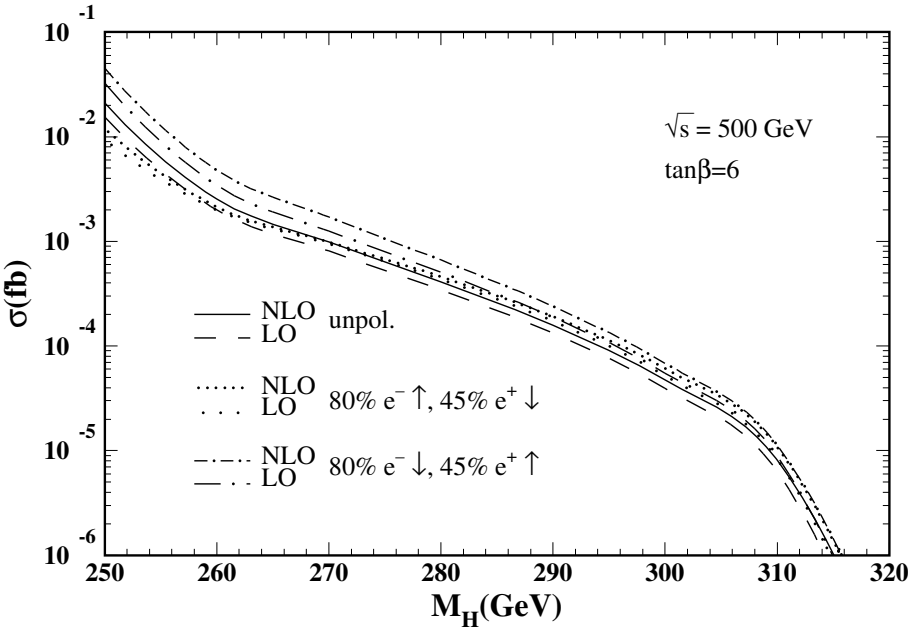

Figure 5.8: Study of the polarization for LO and NLO total cross section including the SUSY QCD corrections for $e^+e^- \to t\bar{b}H^-, \bar{t}bH^+$ as a function of m_H, for $\sqrt{s} = 500$ GeV.and $\tan\beta = 2$.

are defined in analogy to Eq. (5.11). In Tab. 5.5, their numerical values are given for $\sqrt{s} = 500$ GeV and $m_h = 120$ GeV.

Integrated form factors	fb
$\hat{g}_{\gamma\gamma}$	0.4871
$\hat{g}_{ZZ}$	0.0894
$\hat{g}_{\gamma Z}$	-0.3765

Table 5.5: Integrated form factors for the process $e^+e^- \to t\bar{t}h$ for different choices of polarization for $\sqrt{s} = 500$ GeV and $m_h = 120$ GeV expressed in fb.

In Tab. 5.6, we have listed the results for the individual contributions to the cross section arising from the diagrams with a virtual photon ($\sigma_{\gamma\gamma}$), a virtual Z (σ_{ZZ}), and their interference terms ($\sigma_{\gamma Z}$), both for unpolarized and 100% polarized beams. They are obtained from Tab. 5.5, multiplying the integrated form factors $\hat{g}_{VV'}$ for the coefficients given in Tab. 5.2. From Tab. 5.6, we observe that again $\sigma_{\gamma Z}$ acquires more importance if we consider the polarized cross section. In the unpolarized case, it represents only

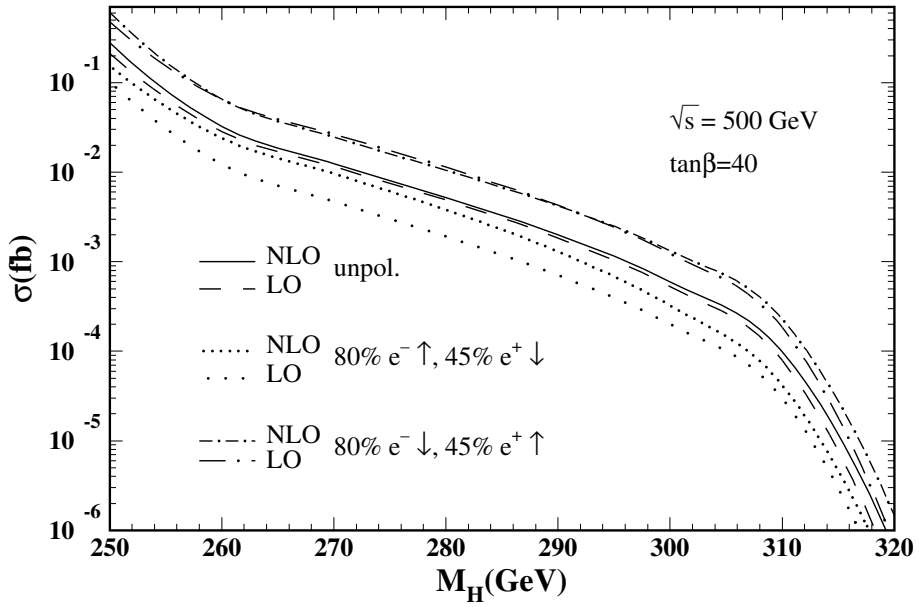

Figure 5.9: Same as in Fig. 5.8 for $\tan\beta = 40$.

4.7% of the total cross section and 5.3% of $\sigma_{\gamma\gamma}$, which amounts to 88% of $\sigma^{\rm unpol}$. For the polarization 100% $e^-\uparrow$ and 100% $e^+\downarrow$, $\sigma_{\gamma Z}$ is negative and its absolute value amounts to 42% of $\sigma_{\gamma\gamma}$. For the opposite choice of polarization, $\sigma_{\gamma Z}$ is positive and represents 32% of the total cross section, and 53% of $\sigma_{\gamma\gamma}$. On the other hand, σ_{ZZ}, remains always small, reaching at most 9% of the total cross section. In contrast to $e^+e^- \to t\bar{b}H^-$, $\sigma_{\gamma\gamma}$ remains always dominant for each choice of the polarization. As a consequence, one can see that all curves in Fig. 5.13 have the same shape and furthermore that the polarized cross sections are always larger than the unpolarized ones.

Cross section	$\sigma_{\gamma\gamma}$	σ_{ZZ}	$\sigma_{\gamma Z}$	$\sigma_{\rm tot}$
$\sigma^{\rm unpol}$	0.3368	0.0242	0.0179	0.3789
σ^{+-}	0.6736	0.0378	−0.2878	0.4235
σ^{-+}	0.6736	0.0590	0.3597	1.0923

Table 5.6: Contributions to the cross section for the process $e^+e^- \to t\bar{t}h$ for different choices of polarization, $\sqrt{s} = 500$ GeV and $m_H = 120$ GeV. We denote by $\sigma_{\rm tot}$ the sum of $\sigma_{\gamma\gamma}$, σ_{ZZ}, and $\sigma_{\gamma Z}$. They are expressed in fb.

Let us now turn to the NLO corrections and consider also realistic values for the

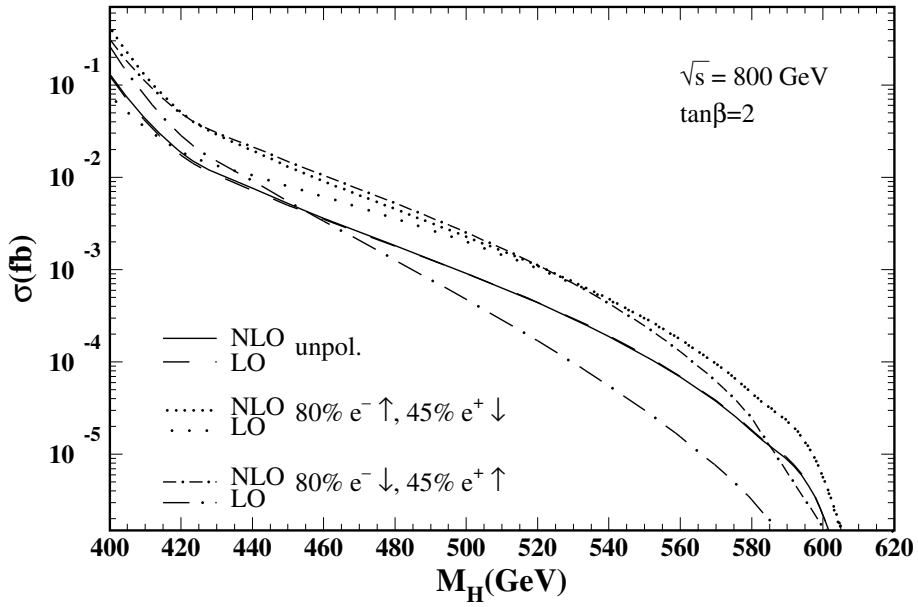

Figure 5.10: Study of the polarization for LO and NLO total cross section including the SUSY QCD corrections for $e^+e^- \to t\bar{b}H^-, \bar{t}bH^+$ as a function of m_H, for $\sqrt{s} =$ 800 GeV.and $\tan\beta = 2$.

polarization. In Figs. 5.14 and 5.15 we compare the results for the unpolarized cross section, with the ones obtained using the polarizations 80% $e^- \uparrow$ 45% $e^+ \downarrow$ and 80% $e^- \downarrow$ 45% $e^+ \uparrow$ for $\sqrt{s} = 500$ GeV (Fig. 5.14) and $\sqrt{s} = 800$ GeV (Fig. 5.15), respectively. In contrast to the case of 100% polarization, one obtains a smaller cross section for positive polarized electrons than in the unpolarized case. Furthermore, the QCD corrections are positive for $\sqrt{s} = 500$ GeV and negative for $\sqrt{s} = 800$ GeV. In Fig. 5.14, one can see that for the polarization 80% $e^- \downarrow$ 45% $e^+ \uparrow$ the cross section is increased by about 90% as compared to the unpolarized one. Regarding $\sqrt{s} = 800$ GeV, we observe in Fig. 5.14 that using the appropriate polarization (80% $e^- \downarrow$ 45% $e^+ \uparrow$), one can enhance the cross section by about 84% for $m_h = 110$ GeV from 2.99 fb to 5.8 fb (i.e. from about 1730 to 3360 events/year) and by about 90% for $m_h = 200$ GeV from 1 fb to 1.9 fb (i.e. from about 580 to 1100 events/year).

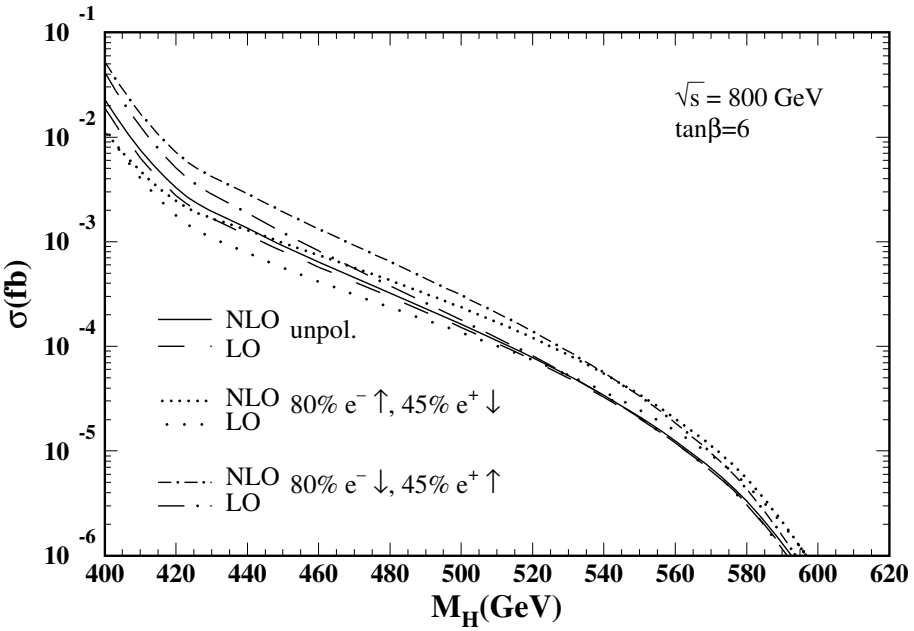

Figure 5.11: Study of the polarization for LO and NLO total cross section including the SUSY QCD corrections for $e^+e^- \to t\bar{b}H^-, \bar{t}bH^+$ as a function of m_H, for $\sqrt{s} = 800$ GeV.and $\tan\beta = 6$.

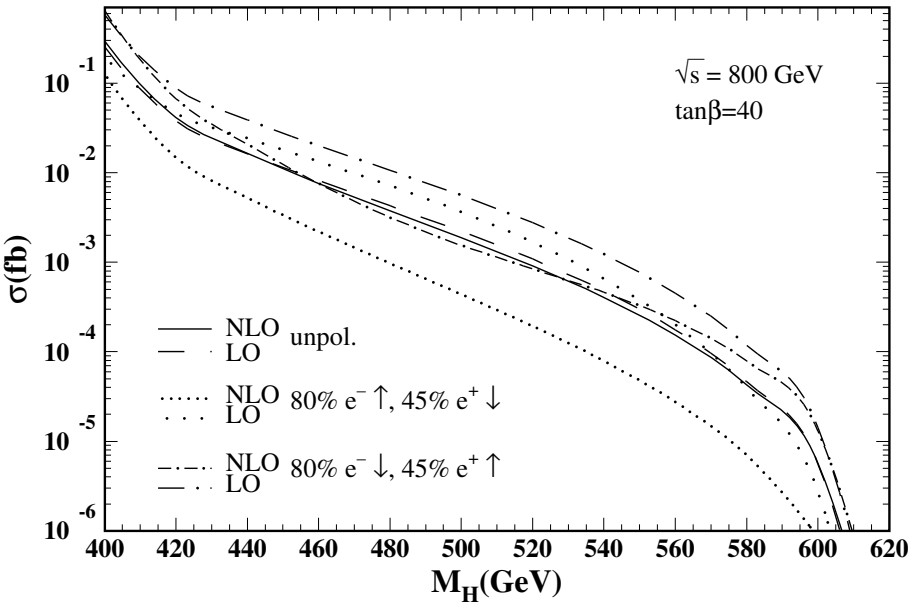

Figure 5.12: Same as in Fig. 5.11 for $\tan\beta = 40$.

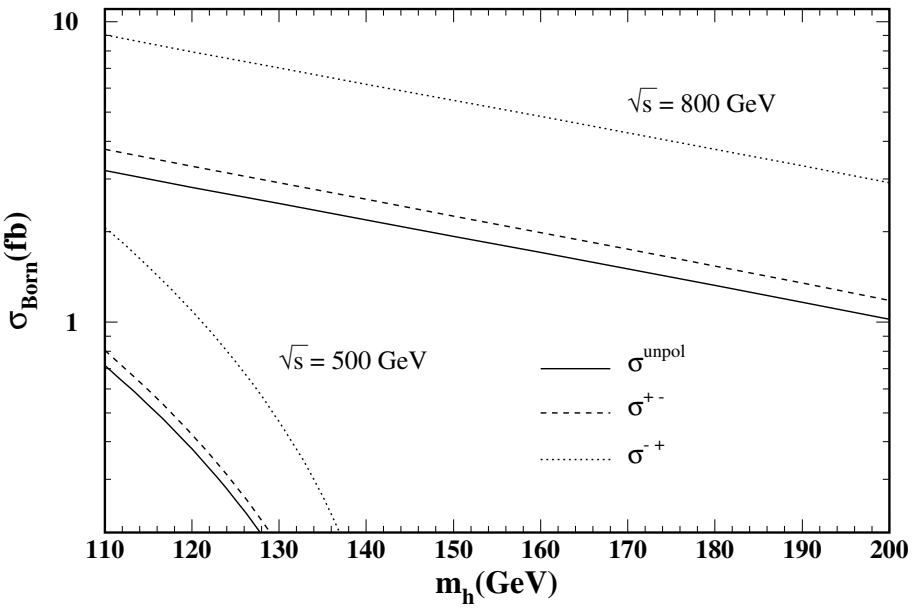

Figure 5.13: Polarized Born cross section for $e^+e^- \to t\bar{t}h$ for $\sqrt{s} = 500$ GeV and $\sqrt{s} = 800$ GeV.

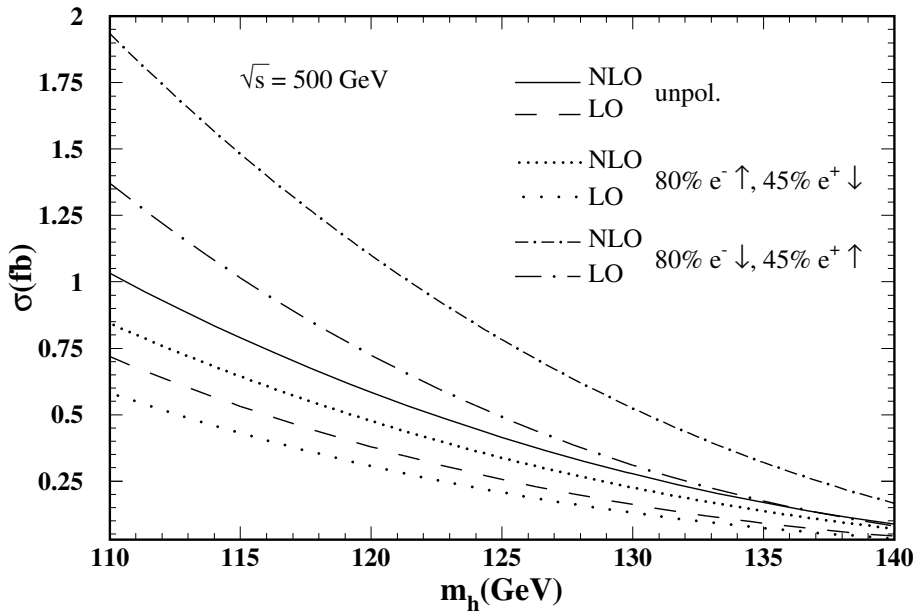

Figure 5.14: LO and NLO cross sections for $e^+e^- \to t\bar{t}h$ for $\sqrt{s} = 500$ GeV for different choices of the polarization.

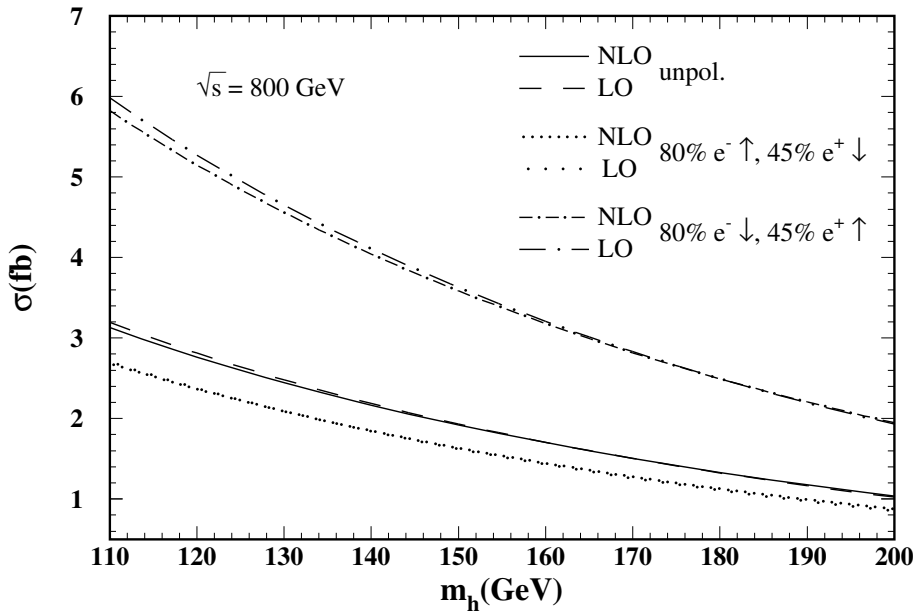

Figure 5.15: Polarized and unpolarized LO and NLO cross section for $e^+e^- \to t\bar{t}h$ for $\sqrt{s} = 800$ GeV.

Chapter 6

Conclusions

In the last years, considerable theoretical and experimental effort has been devoted to the search for the Higgs boson. The complete understanding of the Higgs mechanism would answer fundamental questions like the origin of the masses of the particles observed until now, like the masses of the gauge bosons or the masses of the fermions. In this thesis, we worked in the framework of supersymmetry, which represents an extension of the SM. The motivation for this choice has been discussed in detail in the second chapter of this work, where we provided an introductive description of supersymmetrical theories and in particular to the minimal supersymmetric extension of the SM.

Within the extended Higgs sector of the MSSM, the charged Higgs bosons play an extremely important role, because their detection would imply an unequivocal signal for new physics beyond the SM. Therefore, we devoted the main part of this thesis to investigate the possibility of producing charged Higgs bosons at the next generation of linear colliders. In particular, we have concentrated our attention on the single charged Higgs boson production, by considering the process $e^+e^- \to t\bar{b}H^-$ and its charge conjugate $e^+e^- \to b\bar{t}H^+$. In the third chapter, we have presented the analytical calculation of the next-to-leading order cross section for this reaction, which includes virtual and real QCD corrections and virtual SUSY QCD corrections. We have verified the cancellation of the IR and UV divergences arising from the different contributions and presented an extensive numerical analysis for the total cross section as a function of different values of the charged Higgs boson mass, and of the parameter $\tan\beta$ for typical energies accessible at TESLA. We have considered different choices of the renormalization scheme, providing a detailed comparison of the results in the OS scheme and in two so-called mixed schemes, differing from the former in the choice of the Yukawa coupling renormalization. In particular, we presented our results in the Yukawa mixed scheme, where the mass term arising in the

Yukawa coupling is renormalized in the $\overline{\rm MS}$ scheme, while the remaining counterterms are computed in the OS scheme. We motivated this choice, by showing that the OS renormalization of the Yukawa coupling yields very large logarithms and unnaturally big corrections to the cross section. In the Yukawa mixed scheme, on the other hand, these logarithms are re-absorbed in the $\overline{\rm MS}$ definition of the quark masses arising in the Yukawa coupling and the corrections are moderate for most of the parameter space regions. Moreover, the theoretical uncertainties due to scheme and typical scale variation are significantly reduced passing from the leading-order to the next-to-leading order results. We found that the QCD corrections to the total cross section may be of either sign, depending on the values of $\sqrt{s}$, $\tan\beta$, and m_H and may reach at most a magnitude up to 50%. Furthermore, we could establish that the contribution of the SUSY QCD corrections is important as well, being positive and amounting to about $12-16\%$, depending on the region of the SUSY parameter space and the c.m. energy. Although a complete background analysis is still to be done, if we assume a minimal cut of 10 events for the detection and the design luminosity of TESLA, we can conclude that this process can be observed for large regions of the parameter space, in particular for $\sqrt{s} = 800$ GeV and for Higgs masses near to the production threshold and large values of $\tan\beta$. Furthermore, the cross section of this process has a strong dependence on $\tan\beta$, and its measurement can provide informations on this important parameter.

In order to have a check on our results for the single charged Higgs boson production, we recomputed the results for the SM model process $e^+e^- \to t\bar{t}h$ via a virtual photon [23, 24], which can be obtained from a subclass of the corresponding Feynman diagrams for $e^+e^- \to b\bar{t}H^+$, changing the Yukawa coupling in an appropriate way. Moreover, we completed the computation of the order α_s cross section including also the diagrams with a virtual Z boson and we found agreement with the literature [23, 24]. In the fourth chapter, we discussed the details of this calculation and presented an updated numerical analysis. We confirmed that this process is very important and that the QCD corrections can modify substantially the results for the Born cross section. In fact, they are positive and amount to about 43% for $\sqrt{s} = 500$ GeV, whereas for $\sqrt{s} = 800$ GeV, they are negative and reduce the Born cross section by at most 2%.

Another interesting point that has been addressed in this work is the role played by the beam polarization in order to increase the size of the unpolarized cross sections. Hence, we dedicated the fifth chapter of this thesis to this issue. We have first derived a general expression for the lepton tensor for polarized electron and positron, which can be used for every reaction with e^+e^- in the initial state which take place via a virtual photon or Z boson in the s-channel. In particular, for both the processes $e^+e^- \to b\bar{t}H^+$

and $e^+e^- \to t\bar{t}h$ we have investigated how the Born and order α_s cross sections can be enhanced by a suitable choice of the polarization. We found that using polarized beams, the cross section for $e^+e^- \to t\bar{b}H^-$, can be enhanced up to 120%, enlarging considerably the region of the parameter space where this process could be observed at the next LC. A similar analysis has been performed for the process $e^+e^- \to t\bar{t}h$, where the results for the cross section can be increased up to 90%, giving rise to almost double the number of events per year.

On the basis of this analysis, we can conclude that polarization at the next generation of linear collider will represent an essential tool to explore the nature and properties of the Higgs sector of the theory.

To conclude, we would like to mention that an extension of this work to the neutral Higgs sector of the MSSM is in progress. The computation of the SUSY QCD corrections and the study of the polarization for the processes $e^+e^- \to q\bar{q}h^0, H^0, A^0$ will complete the investigation of the Higgs boson production at the next LC.

Appendix A

Loop Integrals

In this Appendix we give the expressions for the divergent integrals encountered in our calculation. In Sec. A.1, we list the UV divergent scalar and tensor integrals while in Sec. A.2 we give the expression of the IR divergent integrals.

A.1 UV divergent integrals

In this section we define the one-loop integrals which occur in our calculation. The one-loop integrals in $D = 4 - 2\epsilon$ dimensions are classified according to the number N of the propagators in the denominator and the number P of the integration momenta which appear in the numerator. For $P + D - 2N \geq 0$ these integrals are ultraviolet divergent.

The scalar 1-point function is defined by:

$$A_0(m^2) = \frac{(2\pi\mu)^{4-D}}{i\pi^2}\int d^Dq \frac{1}{q^2-m^2}. \tag{A.1}$$

The scalar and 2-point function reads:

$$B_{0,\mu,\mu\nu}(p^2,m_0^2,m_1^2) = \frac{(2\pi\mu)^{4-D}}{i\pi^2}\int d^Dq \frac{1, q_\mu, q_\mu q_\nu}{[q^2-m_0^2][(q+p)^2-m_1^2]}. \tag{A.2}$$

The scalar 3-point fucntion $C_0(p_1^2,p_2^2,p_{12}^2,m_0^2,m_1^2,m_2^2)$ and 4-point function $D_0(p_1^2,p_2^2,p_3^2,p_4^2,p_{12}^2,p_{34}^2,m_0^2,m_1^2,m_2^2,m_3^2)$ are given by:

$$\begin{aligned} C_{0,\mu,\mu\nu} &= \frac{(2\pi\mu)^{4-D}}{i\pi^2}\int d^Dq \frac{1, q_\mu, q_\mu q_\nu}{D_0D_1D_2} \\ D_{0,\mu,\mu\nu} &= \frac{(2\pi\mu)^{4-D}}{i\pi^2}\int d^Dq \frac{1, q_\mu, q_\mu q_\nu}{D_0D_1D_2D_3} \end{aligned} \tag{A.3}$$

where $p_{12}^2 = (p_1 + p_2)^2$, $p_{34}^2 = (p_3 + p_4)^2$, and

$$\begin{aligned} D_0 &= [q^2 - m_0^2 + i\epsilon], \\ D_1 &= [(q + p_1)^2 - m_1^2 + i\epsilon], \\ D_2 &= [(q + p_1 + p_2)^2 - m_2^2 + i\epsilon], \\ D_3 &= [(q + p_1 + p_2 + p_3)^2 - m_3^2 + i\epsilon]. \end{aligned}$$

All tensor integrals can all be expressed as polynomial of the external momenta and of the metric tensor as a consequence of Lorenz covariance [79]. The Lorenz-invariant coefficient of those polynomials can be represented as linear combinations of scalar many-point functions, that is:

$$\begin{aligned} B_\mu &= p^\mu B_1, \\ B_{\mu\nu} &= g_{\mu\nu} B_{00} + p_\mu p_\nu B_{11}, \\ C_\mu &= p_{1\mu} C_1 + p_{2\mu} C_2, \\ C_{\mu\nu} &= g_{\mu\nu} C_{00} + \sum_{i,j=1}^{2} p_{i\mu} p_{j\nu} C_{ij}, \\ D_\mu &= \sum_{i=1}^{3} p_{i\mu} D_i \\ D_{\mu\nu} &= g_{\mu\nu} D_{00} + \sum_{i,j=1}^{3} p_{i\mu} p_{i\nu} D_{ij} \end{aligned} \tag{A.4}$$

We have restricted ourselves to the functions which we need for our calculation, for a complete description of the tensor integral reduction see Ref. [54]. The considered integrals contain the following UV divergences:

$$\begin{aligned} A_0^{\mathrm{UV}}(m^2) &= m^2 \Delta, \\ B_0^{\mathrm{UV}}(p^2, m_0^2, m_1^2) &= \Delta, \\ B_1^{\mathrm{UV}}(p^2, m_0^2, m_1^2) &= -\frac{1}{2}\Delta, \\ B_{00}^{\mathrm{UV}}(p^2, m_0^2, m_1^2) &= \left(\frac{m_0^2 + m_1^2}{4} - \frac{p^2}{12}\right)\Delta, \\ C_{00}^{\mathrm{UV}}(p_1^2, p_2^2, p_{12}^2, m_0^2, m_1^2, m_2^2) &= \frac{1}{4}\Delta, \end{aligned} \tag{A.5}$$

where

$$\Delta = \frac{1}{\epsilon} - \gamma_E + \ln(4\pi), \tag{A.6}$$

and γ_E is the Euler-Mascheroni constant. All other integrals considered here are UV finite.

A.2 IR divergent integrals

In this section we will list the expression of the IR divergent integrals that occur in our calculation. These integrals have been computed by Ref. [52]. We adopt here their notation.

Let us first define the function

$$K(s'+i\epsilon, m_2, m_4) \equiv \frac{1-\sqrt{1-\frac{4m_2m_4}{s'-(m_2-m_4)^2}}}{1+\sqrt{1-\frac{4m_2m_4}{s'-(m_2-m_4)^2}}}, \tag{A.7}$$

valid for $s'-(m_2-m_4)^2 \neq 0$, where we indicate with $s'=(p_1+p_4)^2=(p_2+p_3)$ and $t=(p_1+p_2)^2=(p_3+p_4)$ the Mandelstam variables for the process $14 \to 23$ depicted in Fig. A.1 [1]. We restrict us to the case $s'-(m_2-m_4)^2 \neq 0$ because we do not consider collinear divergences. Furthermore, we define the variables:

$$\begin{aligned} x_s &\equiv -K(s'+i\epsilon, m_2, m_4), \\ x_2 &\equiv -K(m_2^2+i\epsilon, m_2, m_3), \\ x_3 &\equiv -K(m_3^2+i\epsilon, m_3, m_4). \end{aligned} \tag{A.8}$$

In Fig. A.1 we show a generic IR divergent four-point scalar function, where the gluon mass regulator m_g, m_2, and m_4 are real and positive parameters, whereas m_3 is real and non-negative. With the help of the function K and the variables t and s' defined above

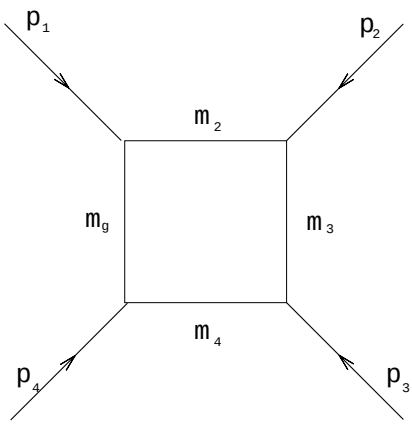

Figure A.1: Generic IR divergent four-point function.

[1] We indicate with a prime the first Mandelstam variable to avoid confusion with the squared c.m. energy s.

the four-point scalar function is given by:

$$
\begin{aligned}
D_0 \;=\; & \frac{x_s}{m_2 m_4 (t-m_3^2)(1-x_s^2)} \left\{ 2\ln(x_s)\left[\ln(1-x_s^2) - \ln\left(\frac{m_g m_3}{m_3^2 - t - i\epsilon}\right)\right] \right. \\
& -\frac{\pi^2}{2} + \mathrm{Li}_2(x_s^2) + \ln^2(x_2) + \ln^2(x_3) - \sum_{\sigma,\rho=\pm 1} \mathrm{Li}_2\left(x_s^2 x_2^\rho x_3^\sigma\right) \\
& \left. + \left[\ln(x_s) + \ln(x_2^\rho) + \ln(x_3^\sigma)\ln\left(1 - x_s^2 x_2^\rho x_3^\sigma\right)\right]\right\},
\end{aligned}
\tag{A.9}
$$

where $D_0 = D_0\left(p_1^2, p_2^2, p_3^2, p_4^2, (p_1+p_2)^2, (p_2+p_3)^2, m_g^2, m_2^2, m_3^2, m_4^2\right)$.

The expression for the three-point IR divergent $C_0 = C_0\left(p_1^2, p_4^2, (p_1+p_4)^2, m_g^2, m_2^2, m_4^2\right)$ function depicted in Fig. A.2 can be obtained from the four-point scalar function using the following relation:

$$
C_0 = \lim_{m_3 \to \infty} \left(-m_3^2 D_0\left(p_1^2, p_2^2, p_3^2, p_4^2, (p_1+p_2)^2, (p_2+p_3)^2, m_g^2, m_2^2, m_3^2, m_4^2\right)\right) \tag{A.10}
$$

Hence, the following result can be derived:

$$
\begin{aligned}
C_0 \;=\; & \frac{x_s}{m_2 m_4 (1-x_s^2)} \left\{ \ln(x_s)\left[-\frac{1}{2}\ln(x_s) + 2\ln(1-x_s^2) - \ln\left(\frac{m_g^2}{m_2 m_4}\right)\right] \right. \\
& \left. -\frac{\pi^2}{6} + \mathrm{Li}_2(x_s^2) + \frac{1}{2}\ln^2\left(\frac{m_2}{m_4}\right) + \mathrm{Li}_2\left(1 - x_s^2\frac{m_2}{m_4}\right) + \mathrm{Li}_2\left(1 - x_s^2\frac{m_4}{m_2}\right)\right\},
\end{aligned}
\tag{A.11}
$$

where again $C_0 = C_0\left(p_1^2, p_4^2, (p_1+p_4)^2, m_g^2, m_2^2, m_4^2\right)$.

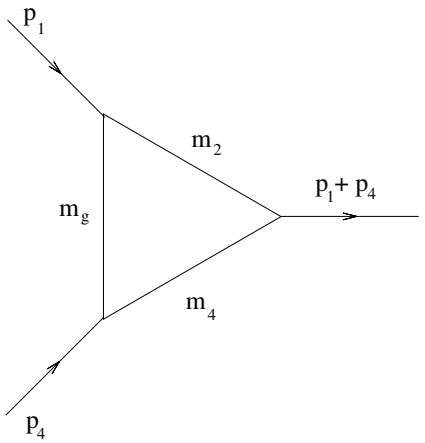

Figure A.2: Generic IR divergent three-point function.

Using the dimensionless variables defined in Sec. 3.3, we have that $s' = sz_3$ and that $x_s = -K(s' + i\epsilon, m_b, m_t) = -K(s' + i\epsilon, m_b, m_t)$. Finally, we list two expressions that we

used to obtain Eq. (3.39):

$$\begin{aligned} x_s &= -\frac{z_3 - a_1 - a_2 - \lambda^{\frac{1}{2}}(z_3, a_1, a_2)}{2\sqrt{a_1}\sqrt{a_2}}, \\ \frac{x_s}{m_b m_t}\frac{1}{(1-x_s^2)} &= -\frac{1}{s\lambda^{\frac{1}{2}}(z_3, a_1, a_2)}. \end{aligned} \tag{A.12}$$

Appendix B

Born form factors

In this Appendix, we list compact expressions for the form factors $f_{\gamma\gamma}(x_1, x_2)$, $f_{\gamma Z}(x_1, x_2)$, and $f_{ZZ}(x_1, x_2)$ appearing in Eq. (3.16) relative to the process $e^+e^- \to t\bar{b}H^-$ and the form factors $g_{\gamma\gamma}(x_1, x_2)$, $g_{\gamma Z}(x_1, x_2)$, and $g_{ZZ}(x_1, x_2)$ appearing in Eq. (4.3) relative to the process $e^+e^- \to t\bar{t}h$. It is possible to combine the propagators of the t quark, b quark, and H^- boson with their couplings to the photon and Z boson by defining the effective couplings

$$\begin{aligned} \mathcal{Q}_q &= -\frac{2c_w s_w Q_q}{1-x_q}, \qquad \mathcal{V}_q = \frac{I_q - 2s_w^2 Q_q}{1-x_q}, \qquad \mathcal{A}_q = \frac{I_q}{1-x_q}, \\ \mathcal{H}_\gamma &= \frac{2c_w s_w}{1-x_3}, \qquad \mathcal{H}_Z = \frac{s_w^2 - c_w^2}{1-x_3}, \end{aligned} \tag{B.1}$$

where $q = t, b$ and we have identified $x_t = x_1$ and $x_b = x_2$. The $t\bar{b}H^-$ coupling introduces $\tan\beta$ dependence through the combinations

$$T_\pm = a_1 \cot^2\beta \pm a_2 \tan^2\beta. \tag{B.2}$$

We find

$$\begin{aligned} f_{ZZ} &= 2\mathcal{V}_t^2\{4a_1a_2(2+2a_1-x_1) + T_+[(1+2a_1)(1+a_1+a_2-a_3-x_1) - x_2(1-x_1)]\} \\ &\quad + 4\mathcal{V}_t\mathcal{V}_b\{2a_1a_2(4+2a_1+2a_2-2a_3-x_1-x_2) \\ &\quad + T_+[(1+a_2-a_3-x_1)(1+a_1-a_3-x_2) + (a_1+a_2)(1+a_1+a_2-a_3) - a_1a_2]\} \\ &\quad + 2\mathcal{V}_b^2\{4a_1a_2(2+2a_2-x_2) + T_+[(1+2a_2)(1+a_1+a_2-a_3-x_2) - x_1(1-x_2)]\} \\ &\quad - 4\mathcal{V}_t\mathcal{A}_t T_-[(1-x_2)(1+2a_1-x_1) - a_1 + a_2 - a_3] \\ &\quad + 4\mathcal{V}_t\mathcal{A}_b T_-[(1+a_2-a_3-x_1)(1+a_1+2a_2-a_3-x_2) \\ &\quad + (a_1-a_2)(1+a_1+a_2-a_3) - 3a_1a_2] \end{aligned}$$

$$
\begin{aligned}
&- 4\mathcal{V}_b\mathcal{A}_t T_-[(1+a_1-a_3-x_2)(1+2a_1+a_2-a_3-x_1)\\
&- (a_1-a_2)(1+a_1+a_2-a_3)-3a_1a_2]\\
&+ 4\mathcal{V}_b\mathcal{A}_b T_-[(1-x_1)(1+2a_2-x_2)+a_1-a_2-a_3]\\
&- 2\mathcal{A}_t^2\{4a_1a_2(2+6a_1-3x_1)-T_+[(1-6a_1)(1+a_1+a_2-a_3-x_1)-x_2(1-x_1)]\}\\
&- 4\mathcal{A}_t\mathcal{A}_b\{2a_1a_2(4+6a_1+6a_2-6a_3-3x_1-3x_2)+T_+[(1+2a_1+a_2-a_3-x_1)\\
&\times(1+a_1+2a_2-a_3-x_2)-(a_1+a_2)(1+a_1+a_2-a_3)+7a_1a_2]\}\\
&- 2\mathcal{A}_b^2\{4a_1a_2(2+6a_2-3x_2)-T_+[(1-6a_2)(1+a_1+a_2-a_3-x_2)-x_1(1-x_2)]\}\\
&+ 2\mathcal{V}_t\mathcal{H}_Z\{4a_1a_2(1-2a_1+2a_2-2a_3-x_2)+T_+[(1+2a_2-2a_3-x_1)\\
&\times(1-a_1-a_2-a_3-x_1-x_2)-2a_1(a_1+a_3)+2a_2(1+a_1+2a_2-2a_3)]\}\\
&- 2\mathcal{V}_b\mathcal{H}_Z\{4a_1a_2(1+2a_1-2a_2-2a_3-x_1)+T_+[(1+2a_1-2a_3-x_2)\\
&\times(1-a_1-a_2-a_3-x_1-x_2)-2a_2(a_2+a_3)+2a_1(1+2a_1+a_2-2a_3)]\}\\
&- 2\mathcal{A}_t\mathcal{H}_Z T_-[(1+2a_1+2a_2-2a_3-x_1)(1+a_1-a_2-a_3-x_1-x_2)\\
&+ 2a_2(1-2a_1+2a_2-2a_3)]\\
&- 2\mathcal{A}_b\mathcal{H}_Z T_-[(1+2a_1+2a_2-2a_3-x_2)(1-a_1+a_2-a_3-x_1-x_2)\\
&+ 2a_1(1+2a_1-2a_2-2a_3)]\\
&- \mathcal{H}_Z^2[4a_1a_2(3-4a_3-2x_1-2x_2)\\
&+ T_+(3-4a_3-2x_1-2x_2)(1+a_1+a_2-a_3-x_1-x_2)]. \qquad \text{(B.3)}
\end{aligned}
$$

The formulas for $f_{\gamma\gamma}(x_1,x_2)$ and $f_{\gamma Z}(x_1,x_2)$ may be obtained from Eq. (B.3) by adjusting the coupling constants. Specifically, one has to substitute

$$
\mathcal{V}_q \to \mathcal{Q}_q, \qquad \mathcal{A}_q \to 0, \qquad \mathcal{H}_Z \to \mathcal{H}_\gamma \qquad \text{(B.4)}
$$

in the first case and

$$
\begin{aligned}
\mathcal{V}_q\mathcal{V}_{q'} &\to \mathcal{Q}_q\mathcal{V}_{q'}+\mathcal{Q}_{q'}\mathcal{V}_q, \qquad \mathcal{V}_q\mathcal{A}_{q'}\to\mathcal{Q}_q\mathcal{A}_{q'}, \qquad \mathcal{A}_q\mathcal{A}_{q'}\to 0,\\
\mathcal{V}_q\mathcal{H}_Z &\to \mathcal{Q}_q\mathcal{H}_Z+\mathcal{V}_q\mathcal{H}_\gamma, \qquad \mathcal{A}_q\mathcal{H}_Z\to\mathcal{A}_q\mathcal{H}_\gamma, \qquad \mathcal{H}_Z^2\to 2\mathcal{H}_\gamma\mathcal{H}_Z \qquad \text{(B.5)}
\end{aligned}
$$

in the second one $(q, q' = t, b)$.

We now turn to the form factors of the process $e^+e^- \to t\bar{t}h$ appearing in Eq. (4.3). Analogously to Eq. (B.1), we define the effective couplings

$$
\begin{aligned}
\mathcal{Q}_{t,t'} &= -\frac{2c_w s_w Q_t}{1-x_{1,2}}, \qquad \mathcal{V}_{t,t'}=\frac{I_t-2s_w^2Q_t}{1-x_{1,2}},\\
\mathcal{A}_{t,t'} &= \frac{I_t}{1-x_{1,2}}, \qquad \mathcal{A}_Z=\frac{a_Z}{(1-x_1-x_2-a_3-a_Z)}, \qquad \text{(B.6)}
\end{aligned}
$$

where $a_Z = m_Z^2/s$. We obtain

$$
\begin{aligned}
g_{ZZ} \;=\; & 2\left(\mathcal{V}_t\mathcal{V}_{t'} + \mathcal{A}_t\mathcal{A}_{t'}\right)\Bigg\{a_1\Bigg[(2-x_1-x_2)^2 - a_3\Bigg(\frac{(2-x_1-x_2)^2}{(1-x_1)(1-x_2)} \\
& 2(1-x_1-x_2-a_3)) + 2a_1\left(4(2-x_1-x_2-a_3)+\right. \\
& \left.\frac{(2-x_1-x_2)^2}{(1-x_1)(1-x_2)}(4a_1-a_3+2)\right)\Bigg] \\
& + 2a_Z\mathcal{A}_Z^2(1-x_1)(1-x_2)\left[a_3+(1-x_1)(1-x_2)+2(x_1+x_2-1)+4a_1\right] \\
& - 4\mathcal{A}_Z a_1 a_Z\left[(2-x_1-x_2)(a_3-4a_1-2)-2(1-x_1)(1-x_2)+(2-x_1-x_2)^2\right]\Bigg\} \\
& + 2\mathcal{A}_t\mathcal{A}_{t'}\Bigg\{-2a_1\left[(1-x_1)(1-x_2)(x_1+x_2-1)\right. \\
& - a_3\left((1-x_1)(1-x_2)+8a_1+2(2-x_1-x_2)-2a_3\right) \\
& \left.+a_1(2-x_1-x_2)\left(14-x_1-x_2+3\frac{2-x_1-x_2}{(1-x_1)(1-x_2)}(4a_1-a_3)\right)\right] \\
& + 2\mathcal{A}_Z^2 a_Z a_1(1-x_1)(1-x_2)\Big[(4a_3-(2-x_1-x_2)^2-12a_Z) \\
& \left.+\frac{1}{a_Z}\left(4a_3-(2-x_1-x_2)^2(1-x_1-x_2-a_3+a_Z)\right)\right] \\
& - 4\mathcal{A}_Z a_1(2-x_1-x_2)\left[\left((1-x_1)(1-x_2)-a_3\right)(1-x_1-x_2-a_3)\right. \\
& \left.+a_1\left(12a_Z-4a_3+(2-x_1-x_2)^2\right)-3a_Z\left(a_3-\frac{2(1-x_1)(1-x_2)}{2-x_1-x_2}\right)\right]\Bigg\}. \qquad \text{(B.7)}
\end{aligned}
$$

The formulas for $g_{\gamma\gamma}(x_1,x_2)$ and $g_{\gamma Z}(x_1,x_2)$ may be obtained from Eq. (B.7) with the help of the substitution

$$
\mathcal{V}_{t,t'} \to \mathcal{Q}_{t,t'}, \qquad \mathcal{A}_{t,t'} \to 0, \qquad \mathcal{A}_Z \to 0 \qquad \text{(B.8)}
$$

to obtain $g_{\gamma\gamma}(x_1,x_2)$ and

$$
\begin{aligned}
\mathcal{V}_t\mathcal{V}_{t'} \;&\to\; \mathcal{Q}_t\mathcal{V}_{t'} + \mathcal{Q}_{t'}\mathcal{V}_t, \qquad \mathcal{A}_t\mathcal{A}_{t'} \to 0, \\
\mathcal{V}_t\mathcal{A}_Z \;&\to\; \mathcal{Q}_t\mathcal{A}_Z, \qquad \mathcal{A}_q\mathcal{A}_Z \to 0, \qquad \mathcal{A}_Z^2 \to 0 \qquad \text{(B.9)}
\end{aligned}
$$

to obtain $g_{\gamma Z}(x_1,x_2)$, respectively.

Appendix C

Four-particle phase space

In this Appendix, we present the parameterization of the four-particle phase space that we use to evaluate the hard-gluon contribution. We generically denote the four-momenta and masses of the final-state particles as p_i and m_i $(i = 1, \ldots, 4)$, respectively. Similarly as in Sec. 3.3, we define $p = \sum_{i=1}^4 p_i$, $s = p^2$, $a_i = m_i^2/s$, $x_i = 2p\cdot p_i/s$, and $y_i = \sqrt{x_i^2 - 4a_i}$. Due to four-momentum conservation, we have $\sum_{i=1}^4 x_i = 2$. We decompose the four-particle phase space into three nested two-particle phase spaces as [43]

$$d\mathrm{PS}_4(p; p_1, p_2, p_3, p_4) = \frac{ds_{12} ds_{34}}{(2\pi)^2} d\mathrm{PS}_2(p; p_{12}, p_{34})\, d\mathrm{PS}_2(p_{12}; p_1, p_2)\, d\mathrm{PS}_2(p_{34}; p_3, p_4), \quad \text{(C.1)}$$

where $p_{ij} = p_i + p_j$ and $s_{ij} = p_{ij}^2$, with $(i, j) = (1, 2), (3, 4)$. As in Sec. 3.3, we work in the c.m. frame, take the z axis of the coordinate system to point along $\boldsymbol{k_1} = -\boldsymbol{k_2}$, and choose the x axis arbitrarily. We have $\boldsymbol{p_{12}} = -\boldsymbol{p_{34}}$ and $|\boldsymbol{p_{12}}| = (1/2)\sqrt{\lambda(s, s_{12}, s_{34})/s}$. Using

$$\begin{aligned} d\mathrm{PS}_2(p; p_{12}, p_{34}) &= \frac{|\boldsymbol{p_{12}}|}{(4\pi)^2\sqrt{s}} d\cos\theta_{12}\, d\phi_{12}, \\ d\mathrm{PS}_2(p_{ij}; p_i, p_j) &= \frac{1}{(4\pi)^2 |\boldsymbol{p_{ij}}|} dp_i^0\, d\phi_i, \end{aligned} \quad \text{(C.2)}$$

where θ_{12} and ϕ_{12} are the polar and azimuthal angles of $\boldsymbol{p_{12}}$, respectively, and ϕ_i is the azimuthal angle of $\boldsymbol{p_i}$ with respect to the axis pointing along $\boldsymbol{p_{ij}}$ measured from the plane spanned by $\boldsymbol{k_1}$ and $\boldsymbol{p_{ij}}$, we obtain

$$d\mathrm{PS}_4(p; p_1, p_2, p_3, p_4) = \frac{8}{(4\pi)^8\sqrt{\lambda(s, s_{12}, s_{34})}} ds_{12}\, ds_{34}\, d\cos\theta_{12}\, d\phi_{12}\, dp_1^0\, d\phi_1\, dp_3^0\, d\phi_3. \quad \text{(C.3)}$$

Owing to the azimuthal symmetry of the problem under consideration, the integration over ϕ_{12} is trivial, and we may choose $\boldsymbol{p_{12}}$ to lie in the x-z plane. If we now rotate the

coordinate system in such a way that $\boldsymbol{p_{12}}$ points along the z axis and $\boldsymbol{p_1}$ lies in the x-z plane, then $\theta = \theta_{12}$ and $\phi = \pi - \phi_1$ define the direction of $\boldsymbol{k_1}$. Introducing $z_{ij} = s_{ij}/s$, we thus have

$$d\mathrm{PS}_4(p; p_1, p_2, p_3, p_4) = \frac{s^2}{(4\pi)^7\sqrt{\lambda(1, z_{12}, z_{34})}} dz_{12}\, dz_{34}\, dx_1\, dx_3\, d\phi_3\, d\cos\theta\, d\phi. \tag{C.4}$$

As explained in Eq. (3.9), the integrations over $\cos\theta$ and ϕ can be exploited to transform the leptonic tensor $L^{\mu\nu}$ defined by Eq. (3.3), which depends on k_1 and k_2, into one depending only on p, so as to preclude scalar products of the type $k_i \cdot p_j$. The residual scalar products read

$$\begin{aligned}
p_1 \cdot p_2 &= \frac{s}{2}(z_{12} - a_1 - a_2), \\
p_3 \cdot p_4 &= \frac{s}{2}(z_{34} - a_3 - a_4), \\
p_1 \cdot p_3 &= \frac{s}{4}[x_1 x_3 - y_1 y_3(\sin\theta_1 \sin\theta_3 \cos\phi_3 - \cos\theta_1 \cos\theta_3)], \\
p_1 \cdot p_4 &= \frac{s}{2}(x_1 - z_{12} - a_1 + a_2) - p_1 \cdot p_3, \\
p_2 \cdot p_3 &= \frac{s}{2}(x_3 - z_{34} - a_3 + a_4) - p_1 \cdot p_3, \\
p_2 \cdot p_4 &= \frac{s}{2}(1 - x_1 - x_3 + a_1 - a_2 + a_3 - a_4) + p_1 \cdot p_3,
\end{aligned} \tag{C.5}$$

where θ_i is the angle enclosed between $\boldsymbol{p_{ij}}$ and $\boldsymbol{p_i}$. It is determined by

$$\cos\theta_i = \frac{x_i(1 + z_{ij} - z_{kl}) - 2(z_{ij} + a_i - a_j)}{y_i\sqrt{\lambda(1, z_{ij}, z_{kl})}}, \tag{C.6}$$

with $(i, j), (k, l) = (1, 2), (3, 4)$ and $(i, j) \neq (k, l)$. Furthermore, we have

$$x_j = 1 - x_i + z_{ij} - z_{kl}. \tag{C.7}$$

The limits of integration are

$$\begin{aligned}
(\sqrt{a_1} + \sqrt{a_2})^2 &< z_{12} < (1 - \sqrt{a_3} - \sqrt{a_4})^2, \\
(\sqrt{a_3} + \sqrt{a_4})^2 &< z_{34} < (1 - \sqrt{z_{12}})^2, \\
x_i^- &< x_i < x_i^+, \\
0 &< \phi_3 < 2\pi,
\end{aligned} \tag{C.8}$$

where

$$x_i^{\pm} = \frac{1}{2z_{ij}}\left[(1 + z_{ij} - z_{kl})(z_{ij} + a_i - a_j) \pm \sqrt{\lambda(1, z_{ij}, z_{kl})\lambda(z_{ij}, a_i, a_j)}\right]. \tag{C.9}$$

For the application in Sec. 3.4.2, it is convenient to assign the indices 1, 2, 3, and 4 to the t quark, $\overline{b}$ quark, gluon, and H^- boson, respectively. Then, the hard-gluon condition $q^0 > E_{\text{cut}}$ may be implemented by substituting $x_3^- \to \max\left(x_3^-, 2E_{\text{cut}}/\sqrt{s}\right)$ in Eq. (C.8). Furthermore, we have $a_3 = 0$ throughout this appendix.

Appendix D

Quark selfenergy

In this appendix we report the results for the quark selfenergy. As we consider only QCD and SUSY QCD corrections we will have just three diagrams contributing to the selfenergy. These are displayed in Fig. D.1. In general, the the quark selfenergy can be

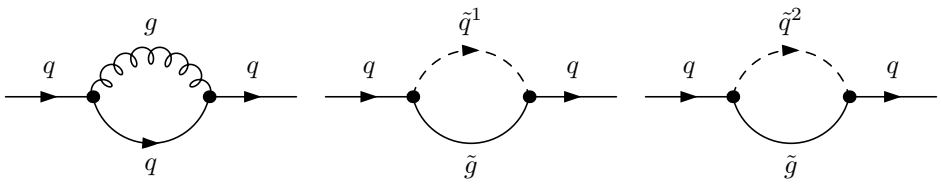

Figure D.1: QCD and SUSY QCD contributions to the quark selfenergy.

decomposed as follows [48]:

$$\Sigma(\not{p}) = \not{p} P_L \Sigma^L(p^2) + \not{p} P_R \Sigma^R(p^2) + P_L \Sigma^D(p^2) + P_R \Sigma^{D*}(p^2), \tag{D.1}$$

where $P_{L,R} = \frac{1}{2}(1 \mp \gamma_5)$ are the chirality projection operators and

$$\Sigma^L(p^2) = \Sigma^{L*}(p^2), \qquad \Sigma^R(p^2) = \Sigma^{R*}(p^2). \tag{D.2}$$

Eq. (D.1) generalizes the decomposition

$$\Sigma(\not{p}) = \not{p} P_L \Sigma^L(p^2) + \not{p} P_R \Sigma^R(p^2) + m_q \Sigma^S(p^2), \tag{D.3}$$

which is specific for the SM [80]. We indicate with Σ_g^q and $\Sigma_{\tilde{g}}^q$ the part of the selfenergy concerning the first diagram and the other two diagrams from the left, respectively.

$$\Sigma_g^{q,L}(p^2) \;=\; -\frac{\alpha_s}{4\pi} C_F \left[2B_1(p^2, m_q^2, m_g^2) + 1 \right], \tag{D.4}$$

$$
\begin{aligned}
\Sigma_g^{q,R}(p^2) &= \Sigma_g^{q,L}(p^2), \\
\Sigma_g^{q,D}(p^2) &= -\frac{\alpha_s}{4\pi} C_F m_q \left[4B_0(p^2, m_q^2, m_g^2) - 2 \right], \\
\Sigma_g^{q,D*}(p^2) &= \Sigma_g^{q,D}(p^2) = m_q \Sigma_g^{q,S}(p^2).
\end{aligned} \tag{D.5}
$$

The inclusion of the superparticles leads to the following contributions to the selfenergy

$$
\begin{aligned}
\Sigma_{\tilde{g}}^{q,L}(p^2) &= -\frac{\alpha_s}{2\pi} C_F \sum_i \left(|S_{i1}|^2 B_1(p^2, m_{\tilde{g}}^2, m_{\tilde{q}_i}^2) \right), \\
\Sigma_{\tilde{g}}^{q,R}(p^2) &= -\frac{\alpha_s}{2\pi} C_F \sum_i \left(|S_{i2}|^2 B_1(p^2, m_{\tilde{g}}^2, m_{\tilde{q}_i}^2) \right), \\
\Sigma_{\tilde{g}}^{q,D}(p^2) &= -\frac{\alpha_s}{2\pi} C_F m_{\tilde{g}} \sum_i \left(S_{i1} S_{i2}^* B_0(p^2, m_{\tilde{g}}^2, m_{\tilde{q}_i}^2) \right), \\
\Sigma_{\tilde{g}}^{q,D*}(p^2) &= -\frac{\alpha_s}{2\pi} C_F m_{\tilde{g}} \sum_i \left(S_{i2} S_{i1}^* B_0(p^2, m_{\tilde{g}}^2, m_{\tilde{q}_i}^2) \right).
\end{aligned} \tag{D.6}
$$

Bibliography

[1] S. L. Glashow, Nucl. Phys. **B22**, 579 (1961);
S. Weinberg, Phys. Rev. Lett. **19**, 1264 (1967);
A. Salam, in *Proceeding of the 8th Nobel Symposium*, p.367, ed. N. Svartholm, Almqvist and Wiksell, Stockholm (1968).

[2] D. Abbaneo *et al.* (LEP Electroweak Working Group) and A. Chou *et al.* (SLD Heavy Flavour and Electroweak Groups), LEPEWWG/2002-01 (May 2002), arXiv:hep-ex/0112021 and additional updates at `http://lepewwg.web.cern.ch/LEPEWWG/`.

[3] P. W. Higgs, Phys. Rev. Lett. **12**, 132 (1964);
F. Englert and R. Brout, Phys. Rev. Lett. **12**, 132 (1964);
G. S. Guralnik, C. R. Hagen, and T. W. B. Kibble, Phys. Rev. Lett. **13**, 585 (1964).

[4] Y. Fukada *et al.* (Super-Kamiokande Collaboration), Phys. Rev. Lett. **82**, 2430 (1999).

[5] F. Abe *et al.* (CDF Collaboration), Phys. Rev. Lett. **74**, 2626 (1995);
S. Abachi *et al.* (D0 Collaboration), Phys. Rev. Lett. **74**, 2632 (1995).

[6] P. Bock *et al.* (ALEPH, DELPHI, L3 and OPAL Collaborations, The LEP working group for Higgs boson searches), LHWG Note 2001-03 (July 2001), arXiv:hep-ex/0107029, and additional updates at `http://lephiggs.web.cern.ch/LEPHIGGS/www/Welcome.html`.

[7] J. Andruszkow *et al.*, TESLA Technical Design Report, edited by R. Brinkmann, K. Flöttman, J. Rossbach, P. Schmüser, N. Walker, and H. Weise, Report No. DESY 2001-011, ECFA 2001-209, TESLA Report 2001-23, and TESLA-FEL 2001-05, 2001. arXiv:hep-ph/0106315.

[8] For an introduction see: J. Wess and J. Bagger, *Supersymmetry and Supergravity*, 2nd Edition, Princeton Series in Physics, 1992.

[9] S. Weinberg, Phys. Rev. D **13** , 974 (1976) and Phys. Rev. D **19** , 1277 (1979);
L. Susskind, Phys. Rev. D **20**, 2619 (1979);
G. 't Hooft, in *Recent Developments in Gauge Theories*, Proceeding of the NATO Advanced Summer Institute, Cargese 1979, ed. by G. 't Hooft *et al.*, Plenum, New York (1980).

[10] U. Amaldi, W. de Boer, and H. Fürstenau, Phys. Lett. B **260**, 447 (1991).

[11] P. Fayet, Phys. Lett. **B69**, 489 (1984);
P. Fayet and S. Ferrara, Phys. Rep. **32**, 249 (1977).

[12] H.P. Nilles, Phys. Rep. **110**, 132 (1984).

[13] H. E. Haber and G. Kane, Phys. Rep. **117**, 75 (1985).

[14] S. Komamiya, Phys. Rev. D **38**, 2158 (1988).

[15] S. Kanemura, S. Moretti, and K. Odagiri, JHEP **0102**, 011 (2001).

[16] S. Kanemura, Eur. Phys. J. C **17**, 473 (2000);
H. E. Logan and S. Su, Phys. Rev. D **66**, 035001 (2002).

[17] A. Arhrib, M. Capdequi Peyranere, W. Hollik, and G. Moultaka, Nucl. Phys. **B581**, 34 (2000).

[18] S. Moretti, Report No. CERN-TH/2002-137, IPPP/02/30, DCPT/)2/60, and arXiv:hep-ph/0206208.

[19] A. Djouadi, J. Kalinowski, and P. M. Zerwas, Z. Phys. C **54**, 255 (1992).

[20] S. Kiyoura, private communication.

[21] J. L. Feng and T. Moroi, Phys. Rev. D **56**, 5962 (1997).

[22] B. A. Kniehl, F. Madricardo, and M. Steinhauser, Phys. Rev. D **66**, 054016 (2002).

[23] S. Dittmaier, M. Krämer, Y. Liao, M. Spira, and P. M. Zerwas, Phys. Lett. B **441**, 383 (1998).

[24] S. Dawson and L. Reina, Phys. Rev. D **59**, 054012 (1999).

[25] S. Dimopoulos and H. Georgi, Nucl. Phys. **B193**, 150 (1981).

[26] E. Gildener, Phys. Rev. D **14** , 1667 (1976);
S. Weinberg, Phys. Lett. B **82**, 387 (1979);
L. Susskind, Phys. Rep. **104**, 181 (1984).

[27] D. Z. Freedman, P. van Nieuwenhiuzen, and S. Ferrara, Phys. Rev. D **13**, 3214 (1976);
S. Deser and B. Zumino, Phys. Lett. B **62**, 335 (1976).

[28] R. Haag, J.T. Lopuszanski, and M. Sohnius, Nucl. Phys. **B88**, 257 (1975).

[29] J. Wess and B. Zumino, Nucl. Phys. **B70**, 39 (1974) and **B78**, 1 (1974);
S. Ferrara and B. Zumino, Nucl. Phys. **B79**, 413 (1974);
A. Salam and J. Strathdee, Phys. Lett. B **51**, 353 (1974) and Nucl. Phys. **B76**, 477 (1974).

[30] Yu. A. Gol'fand and E. P. Likhtman, JETP Lett. **13**, 323 (1971);
D. V. Volkov and V. P. Akulov, Phys. Lett. B **46**, 109 (1973).

[31] S. Coleman and J. Mandula, Phys. Rev. **159**, 1251 (1967).

[32] G. R. Farrar and P. Fayet, Phys. Lett. B **76**, 575 (1978); S. Weinberg, Phys. Rev. D **26**, 287 (1982).

[33] L. O'Raifeartaigh, Nucl. Phys. **B96**, 461 (1975).

[34] P. Fayet and J. Iliopoulos, Phys. Lett. B **51**, 461 (1974).

[35] G. F. Giudice and R. Rattazzi, Phys. Rep. **322**, 419 (1999).

[36] L. Girardello and M. Grisaru, Nucl. Phys. **B194**, 65 (1982).

[37] J. F. Gunion, H. E. Haber, G. Kane, and S. Dawson, *The Higgs Hunter's Guide*, Frontiers in Physics Vol. 80, Addison-Wesley, (1990).

[38] M. Carena and H. E. Haber, arXiv:hep-ph/0208209.

[39] K. Inoue, A. Kakuto, H. Komatsu, and H. Takeshita, Prog. Theor. Phys. **68**, 927 (1982) and **71**, 413 (1984);
N. K. Falck, Z. Phys. C **30**, 247 (1986).

[40] Particle Data Group, K. Hagiwara *et al.*, Phys. Rev. D **66**, 010001 (2002).

[41] F. Bloch and A. Nordsieck, Phys. Rev. **52**, 54 (1937).

[42] T. Kinoshita, J. Math. Phys. **3**, 650 (1962);
T. D. Lee and M. Nauenberg, Phys. Rev. B **133**, 1549 (1964).

[43] E. Byckling and K. Kajantie, *Particle Kinematics*, (John Wiley and Sons, London, (1973).

[44] G. P. Lepage, J. Comput. Phys. **27**, 192 (1978).

[45] G. 't Hooft and M. Veltman, Nucl. Phys. **B44**, 189 (1972).

[46] W. A. Bardeen, A. J. Buras, D. W. Duke, and T. Muta, Phys. Rev. D **18**, 3998 (1978).

[47] D. A. Ross and J. C. Taylor, Nucl. Phys. **B51**, 25 (1979).

[48] B. A. Kniehl and A. Pilaftsis, Nucl. Phys. **B474**, 286 (1996).

[49] J. Küblbeck, M. Böhm, and A. Denner, Comput. Phys. Commun. **60**, 165 (1990);
T. Hahn, Comput. Phys. Commun. **140**, 418 (2001);
T. Hahn and C. Schappacher, Comput. Phys. Commun. **143**, 54 (2002).

[50] T. Hahn and M. Pérez-Victoria, Comput. Phys. Commun. **118**, 153 (1999);
T. Hahn, Acta Phys. Polon. B **30**, 3469 (1999); Nucl. Phys. B (Proc. Suppl.) **89**, 231 (2000).

[51] J. A. M. Vermaseren, *Symbolic Manipulation with FORM*, (Computer Algebra Netherlands, Amsterdam, 1991).

[52] W. Beenakker and A. Denner, Nucl. Phys. **B338**, 349 (1990).

[53] G. 't Hooft and M. Veltman, Nucl. Phys. **B153**, 365 (1979).

[54] A. Denner, Fortschr. Phys. **41**, 307 (1993).

[55] A. H. Hoang, M. Jezabek, J. H. Kühn, and T. Teubner, Phys. Lett. B **338**, 330 (1994).

[56] S. D. Ellis, R. Kleiss, and W. J. Stirling,
RA(NDOM) M(OMENTA) B(EAUTIFULLY), O(RGANIZED) (unpublished).

[57] W. Siegel, Phys. Lett. B **84**, 193 (1979).

[58] D. M. Capper, D. R. T. Jones, and P. van Nieuvenhuizen, Nucl. Phys. **B167**, 479 (1980).

[59] W. Siegel, Phys. Lett. B **94**, 37 (1980).

[60] F. del Aguila, A. Culatti, R. Muños Tapia, and M. Pérez-Victoria, Nucl. Phys. **B537**, 561 (1999).

[61] B. A. Kniehl, G. Kramer, and B. Pötter, Phys. Rev. Lett. **85**, 5288 (2000).

[62] B. A. Kniehl, Z. Phys. C **72**, 437 (1996).

[63] S. Dimopoulos and D. Sutter, Nucl. Phys. **B452**, 496 (1995).

[64] M. Veltman, Nucl. Phys. **B123**, 89 (1977).

[65] A. Djouadi, J. L. Kneur, and G. Moultaka, arXiv:hep-ph/9901246. The program can be downloaded from `http://www.lpm.univ-montp2.fr:-6714/kneur/suspect.html`

[66] E. Braaten and J. P. Leveille, Phys. Rev. D **22**, 715 (1980).

[67] A. Mendez and A. Pomarol, Phys. Lett. B **252**, 461 (1990).

[68] B. A. Kniehl and R. Hempfling, Phys. Rev. D **51**, 1386 (1995).

[69] G. Grunberg, Phys. Lett. **95B**, 70 (1980); **110B**, 501(E) (1982); Phys. Rev. D **29**, 2315 (1984).

[70] P. M. Stevenson, Phys. Rev. D **23**, 2916 (1981); Phys. Lett. **100B**, 61 (1981); Nucl. Phys. **B203**, 472 (1982); Phys. Lett. B **231**, 65 (1984).

[71] S. J. Brodsky, G. P. Lepage, and P. B. Mackenzie, Phys. Rev. D **28**, 228 (1983); S. J. Brodsky and H. J. Lu, Phys. Rev. D **51**, 3652 (1995).

[72] A. Krause, T. Plehn, M. Spira, and P. M. Zerwas, Nucl. Phys. **B519**, 85 (1998).

[73] H. Baer, S. Dawson, and L. Reina Phys. Rev. D **61**, 013002 (2000).

[74] S. Dawson and L. Reina, Phys. Rev. D **60**, 015003 (1999); S. Dittmaier, M. Krämer, Y. Liao, M. Spira, and P. M. Zerwas, Phys. Lett. B **478**, 247 (2000).

[75] S. Dawson and L. Reina, Phys. Rev. D **57**, 5851 (1998).

[76] G. Moortgat-Pick and H. Steiner, EPJ direct **C6** (2001) 1-27 and
also in *2nd ECFA/DESY Study 1998-2001* 1261-1296.

[77] J. E. Clendenin, Polarized Electron Sources, SLAC-PUB-95-6842, May 1995 and
Proc. of Particle Accelerator Conference PAC 95, Dallas, Texas, 1-5 May 1995,
pp.877-881 (1995).

[78] K. Flöttmann, DESY-93-161,1993 and DESY-95-064, 1995;
N. Walker, ECFA/DESY LC-Workshop, Hamburg, September 2000.

[79] G. Passarino and M. Veltman, Nucl. Phys. **B160**, 151 (1979).

[80] A. Denner and T.Sack Nucl. Phys. **B347**, 203 (1990).

ACKNOWLEDGMENTS

First, I would like to thank my advisor, Prof. Dr. Bernd A. Kniehl, for allowing me to work on this very interesting topic and for supporting me in these three years with helpful discussions and encouragement. My special thanks go to Dr. Matthias Steinhauser, for his help and patience and the innumerable discussions throughout the time when this work has been completed. I am very grateful to Stefan Berge for his help with Fortran, and computers in general, for several interesting discussions, and for the time spent together. For the nice time in the office and several discussions about physics and more, I would like to thank Luminita Mihaila. I am also thankful to all the Diploma students of the sixth floor for the hospitality in their office and to all the PhD students and the other members of the institute for the enjoyable atmosphere. Finally, I would like to thank Dr. Matthias Steinhauser, Stefan Berge and Dr. C. Mrinal Dasgupta for reading carefully the manuscript.

Ringrazio di cuore anche la mia famiglia e tutti i miei amici in Italia e all'estero, per il loro sostegno e il loro affetto.